

# **Nuclear Fuels & Materials Spotlight**

## **Volume 4**

April 2014



The INL is a U.S. Department of Energy National Laboratory  
operated by Battelle Energy Alliance

**INL/EXT-14-31925**

# **Nuclear Fuels & Materials Spotlight**

## **Volume 4**

**April 2014**

**Idaho National Laboratory  
Idaho Falls, Idaho 83415**

**<http://www.inl.gov>**

**Prepared for the  
U.S. Department of Energy  
Under DOE Idaho Operations Office  
Contract DE-AC07-05ID14517**

# Nuclear Fuels & Materials SPOTLIGHT

VOLUME 4



**Cover Design**

*Transmission Electron Microscopy (TEM) image showing fission gas bubbles self-organized in three dimensions in irradiated uranium molybdenum alloy fuel. This work was conducted as part of Global Threat Reduction Initiative (GTRI) Fuel Development program at INL.*

**Editor**

Lexie Byrd

**Designers/Illustrators**

Scott D. Brown  
Kristine L. Burnham

**Printing Coordination**

Katherine C. Watson

INL/EXT-14-31925

# Nuclear Fuels & Materials SPOTLIGHT

VOLUME 4

*2014*

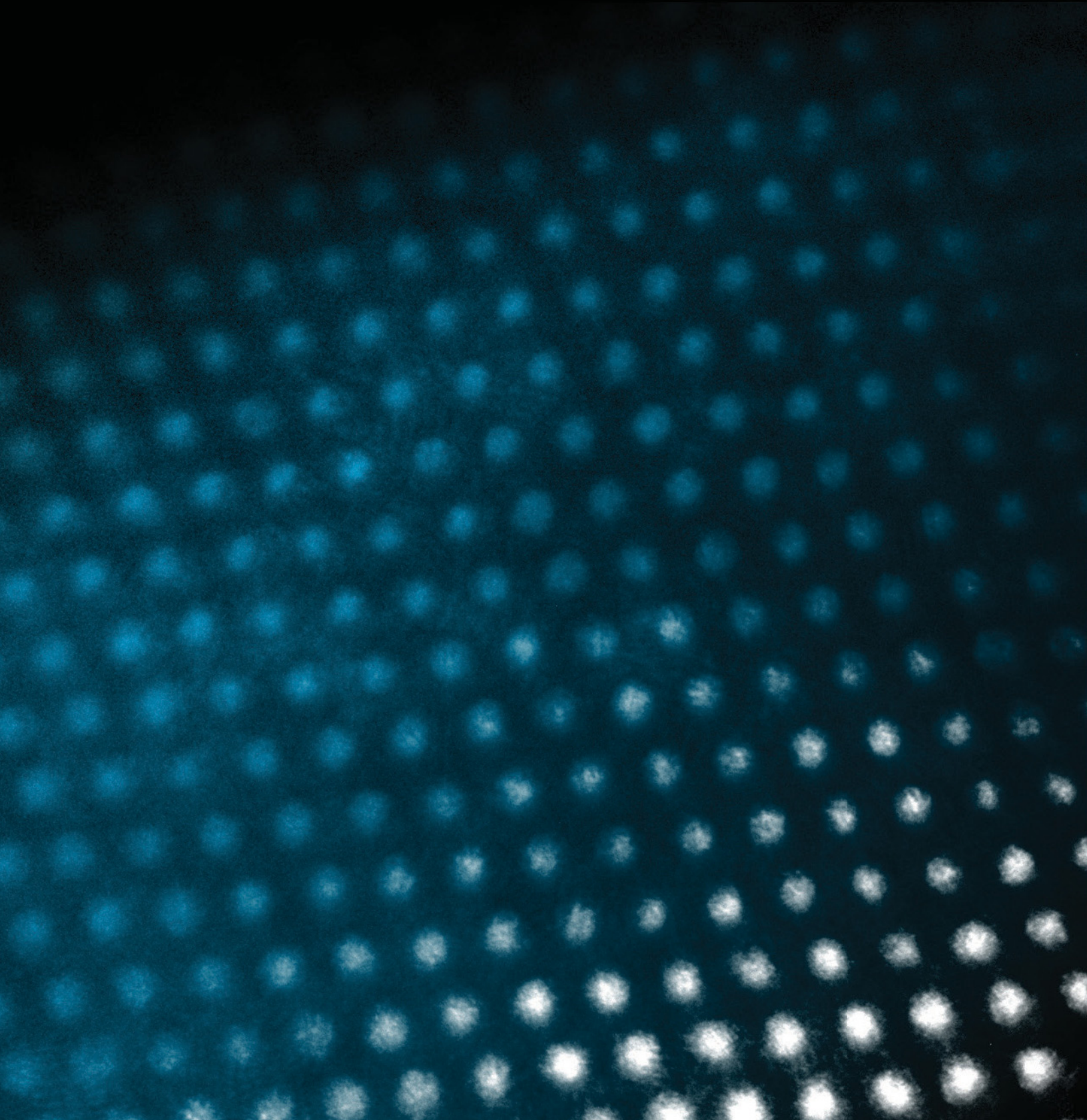
Idaho National Laboratory  
P.O. Box 1625  
Mailstop 3878  
Idaho Falls, ID 83415-3878

[INLNFMSpotlight@inl.gov](mailto:INLNFMSpotlight@inl.gov)

Tel: 208-526-1950  
Fax: 208-526-2930

[www.inl.gov/nuclearfuels](http://www.inl.gov/nuclearfuels)

# Introduction



As the nation's nuclear energy laboratory, Idaho National Laboratory (INL) brings together talented people and specialized nuclear research capability to accomplish our mission. This edition of the Nuclear Fuels and Materials Division *Spotlight* provides an overview of some of our recent accomplishments in research and capability development. These accomplishments include:

- The first identification of silver and palladium migrating through the SiC layer in TRISO fuel
- A description of irradiation assisted stress corrosion testing capabilities that support commercial light water reactor life extension
- Results of high-temperature safety testing on coated particle fuels irradiated in the ATR

- New methods for testing the integrity of irradiated plate-type reactor fuel
- Description of a 'Smart Fuel' concept that wirelessly provides real time information about changes in nuclear fuel properties and operating conditions
- Development and testing of ultrasonic transducers and real-time flux sensors for use inside reactor cores, and an example of a capsule irradiation test.

Throughout *Spotlight*, you'll find examples of productive partnerships with academia, industry, and government agencies that deliver high-impact outcomes. The work conducted at INL helps to spur innovation in nuclear energy applications that drive economic growth and energy security.

We appreciate your interest in our work here at INL, and hope that you find this issue informative.



**Mitchell K. Meyer** is the Director of the Nuclear Fuels and Materials Division (Ph.D. Ceramic Engineering, Iowa State University) at INL. Dr. Meyer has been involved in a wide range of research including nuclear fuels, silicon carbide fiber production, ultra-high temperature materials, and synthesis of polymers. Beginning in 2001, Dr. Meyer began work in the area of transmutation fuel development, including research on the first metal alloy nuclear fuels with high americium and neptunium content. In 2003, Dr. Meyer was appointed to lead the U.S. Generation IV GFR (Gas Fast Reactor) fuel effort to develop novel high-temperature, high-density fuels in conjunction with international partners. In 2004, Meyer assumed the role of National Technical Lead for the Reduced Enrichment for Research and Test Reactors (RERTR) fuel development program, including responsibilities for supplying fuel for conversion of foreign

and domestic reactors to low-enrichment. In 2007, Dr. Meyer was appointed as Interim Director and Scientific Program Manager of the Advanced Test Reactor National Scientific User Facility, tasked to develop an operational strategy for this important facility. Today, in addition to duties as Director of INL's Nuclear Fuels and Materials Division he serves as National Technical Lead for the Global Threat Reduction Initiative (GTRI) fuel development program.

***Disclaimer***

This information was prepared as an account of work sponsored by an agency of the U.S. Government. Neither the U.S. Government nor any agency thereof, nor any of their employees, makes any warranty, express or implied, or assumes any legal liability or responsibility for the accuracy, completeness, or usefulness of any information, apparatus, product, or process disclosed, or represents that its use would not infringe privately owned rights. References here into any specific commercial product, process, or service by trade name, trademark, manufacturer, or otherwise, does not necessarily constitute or imply its endorsement, recommendation, or favoring by the U.S. government or any agency thereof. The views and opinions of authors expressed herein do not necessarily state or reflect those of the U.S. Government or any agency thereof.

**Introduction**

Mitch Meyer, Director, Nuclear Fuels and Materials Division ..... i

**The Fuel Accident Condition Simulator (FACS) Furnace System for High-Temperature Fuel-Performance Testing**

P.A. Demkowicz, L. Scott, D.M. Scates, E.L. Reber ..... 1

**First Reported Identification of Silver and Palladium-Containing Fission Products in Irradiated TRISO-Coated Particles**

I. J. van Rooyen, T. M. Lillo (INL), Y.Q. Wu (BSU, CAES) ..... 11

**EPRI-INL Pilot Project for Characterization of Irradiation Assisted Stress Corrosion Cracking in Alloys X-750 and XM-19**

J.H. Jackson, S.P. Teyseyre ..... 23

**Laser-Based Characterization of Nuclear Fuel Plates**

J.A. Smith, D.L. Cottle, B.H. Rabin ..... 31

**Multiscale Development of Materials Models for Fuel Performance Simulation**

M.R. Tonks, S.B. Biner, Y. Zhang, R.L. Williamson, S.R. Novascone, B.W. Spencer,  
J.D. Hales, D.R. Gaston, C.J. Permann, D. Andrs, S.L. Hayes (INL), P.C. Millett (UofArk),  
D. Andersson, C.R. Stanek (LANL) ..... 41

**Synergistic Smart Fuel for Microstructure Mediated Measurements**

J.A. Smith (INL), R. Ali, S.L. Garrett (PSU) ..... 57

**Assessment of Survival or Ultrasonic Transducers Under Neutron Irradiation**

J.E. Daw, J.L. Rempe, J. Palmer (INL), B. Tittmann, B. Reinhardt (PSU), G. Kohse (MIT), P. Ramuhalli (PNNL),  
H.T. Chien (ANL) ..... 67

**In-core Flux Sensor Evaluations at the ATR Critical Facility**

T. Unruh, B.M. Chase, J.L. Rempe, D.W. Nigg (INL), G. Imel, J.T. Harris (ISU), T. Sherman, J-F Villard (CEA, DEN, DER,  
Instrumentation, Sensors and Dosimetry Laboratory, Cadarache, France) ..... 80

**Luna Innovations Irradiation Experiment**

J. Palmer, P. E. Murray (INL), S. B. Grover (INL-Retired) ..... 95

# **The Fuel Accident Condition Simulator (FACS) Furnace System for High-Temperature Fuel-Performance Testing**

# The Fuel Accident Condition Simulator (FACS) Furnace System for High-Temperature Fuel Performance Testing

PA. Demkowicz, L. Scott, D.M. Scates, E.L. Reber

## Introduction

The performance of nuclear fuels during off-normal reactor events is a key characteristic that strongly influences reactor safety. Understanding how fuel behaves at high temperatures and, in particular, the level of fission product retention in the reactor core, is essential when defining the performance envelope during reactor design. This is particularly true with the high-temperature gas-cooled reactor (HTGR), which uses tristructural isotropic (TRISO) coated particle fuel and helium as coolant.

TRISO fuel consists of a spherical uranium oxide or uranium oxide/carbide fuel kernel approximately 350–500  $\mu\text{m}$  in diameter. The kernel is coated with a porous carbon buffer layer (~100  $\mu\text{m}$  thick), a dense inner pyrolytic carbon layer (~40  $\mu\text{m}$  thick), a silicon carbide (SiC) layer (~35  $\mu\text{m}$  thick), and an outer pyrolytic carbon layer (~40  $\mu\text{m}$  thick),

as shown in Figure 1. Together, these coatings are designed to effectively retain fission products released from the fuel kernel, both during normal reactor operation and during a high-temperature depressurized loss-of-coolant accident. The SiC layer provides the primary structural support and is the main barrier to fission product release.

While TRISO fuel is expected to experience operating temperatures in the range of 1000–1250°C, a depressurized loss-of-coolant accident can see temperatures increase to as high as 1600°C in small fractions of the core. At these temperatures, certain fission products can have significant mobility and are capable of diffusing through coating layers and into the core structural materials and beyond. Cesium release is particularly sensitive to flaws in the SiC layer, while krypton is generally only released if all of the coating layers are breached. Silver diffuses relatively rapidly through intact SiC, and plate-out of

radioactive Ag-110m on cooler reactor components may have consequences for reactor maintenance. In addition, reaction of certain fission products, such as palladium, with the SiC layer is significantly accelerated at these temperatures and could potentially jeopardize the integrity of the coating. High-quality TRISO fuel is designed to withstand these temperatures and prevent significant release of fission products from the core, forming a vital component of the HTGR passive safety case.

The United States recently completed the first in a series of irradiation experiments to test the in-pile performance of TRISO fuel as part of the Very High-Temperature Reactor (VHTR) program. The Advanced Gas Reactor 1 (AGR-1) experiment consisted of 72 fuel compacts—each containing approximately 4,100 coated particles—and was irradiated in the Idaho National Laboratory (INL) Advanced Test Reactor to peak burnups of 19.5% fissions per initial metal atom (FIMA) [1]. The performance of the fuel during irradiation was exceptional, with zero failures out of a total of  $3 \times 10^5$  particles in the experiment, and relatively low release of solid fission products such as cesium and strontium [1, 2].

An important objective of the post-irradiation examination of the fuel is high-temperature performance testing, in which fission product retention of the particles is evaluated at temperatures as high as 1800°C. Measurements of accident performance have historically been carried out during post-irradiation examination by heating fuel elements in pure helium to temperatures in the range of 1600–1800°C, while monitoring releases of the fission gas Kr-85, as well as condensable fission products such as silver, cesium, and strontium [3, 4].

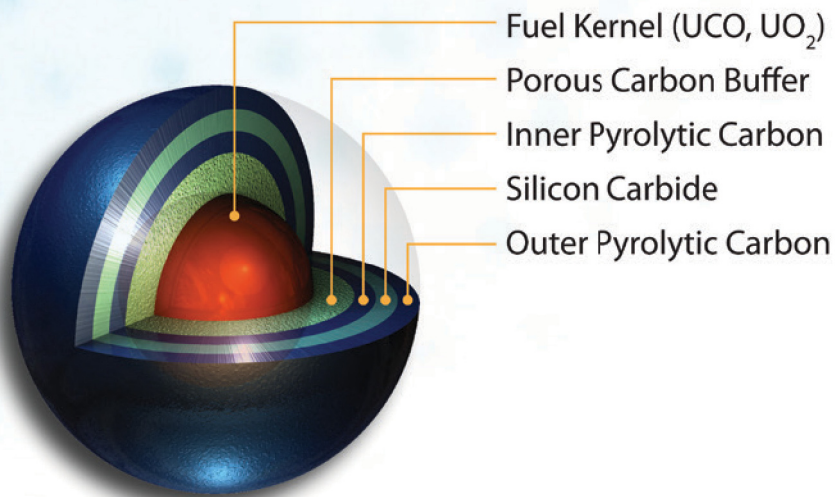


Figure 1. Diagram of a TRISO particle.

The Fuel Accident Condition Simulator (FACS) furnace system has been developed at INL to support the AGR safety testing effort [5], with basic system design features and technical requirements based on the KÜFA furnace used in the 1980s and early 1990s to evaluate high-temperature fission product release characteristics of spherical TRISO fuel elements as part of the German HTGR Program [6]. The system is now being used to perform safety tests on the AGR-1 fuel compacts for the VHTR Program, in parallel with tests performed at Oak Ridge National Laboratory using a similar furnace system developed previously (the Core Conduction Cooled Test Facility). The use of the two separate systems allows for an increased sample throughput for the program (this is an important consideration given the large number of specimens that must be tested to experimentally verify very small particle failure fractions) and independent verification of data integrity by comparing results from the two testing systems.

### FACS System Description

The FACS furnace system consists of the main furnace assembly, power supply, control cabinet with operator control station, cooling-water supply system, and helium supply system. Figure 2 shows the main furnace assembly and the related components, which are located inside the shielded main hot cell at the INL Materials and Fuel Complex (MFC) Hot Fuel Examination Facility (HFEF). The design approach was for a system that would allow for a high degree of automation in basic operation, including condensation plate exchange (described below), to facilitate remote operation. The system is operated using a computer control station with a graphical user interface located near the hot-cell window. The basic system was built by TevTech, LLC, in Billerica, Massachusetts, USA. After delivery to INL, this system

was extensively modified to support remote operation and maintenance in the Hot Fuel Examination Facility hot cells.

Internally, the main furnace chamber has tantalum primary hot zone components and is heated using a graphite resistance element (see Figure 3) powered by a 40-kVA transformer located outside of the hot cell. The fuel specimen is heated inside an 85-mm-diameter tantalum flow tube and is

supported on a tantalum holder that sits atop a tantalum support tube inserted from the bottom of the furnace. Helium is injected into the main chamber through this support tube. The tantalum flow tube has a flat plate at the top with a 19-mm-diameter aperture, where He flow escapes and impinges on the condensation plate. The fuel specimen temperature is monitored with redundant Type C (tungsten-rhenium) thermocouples housed within the tantalum support tube.

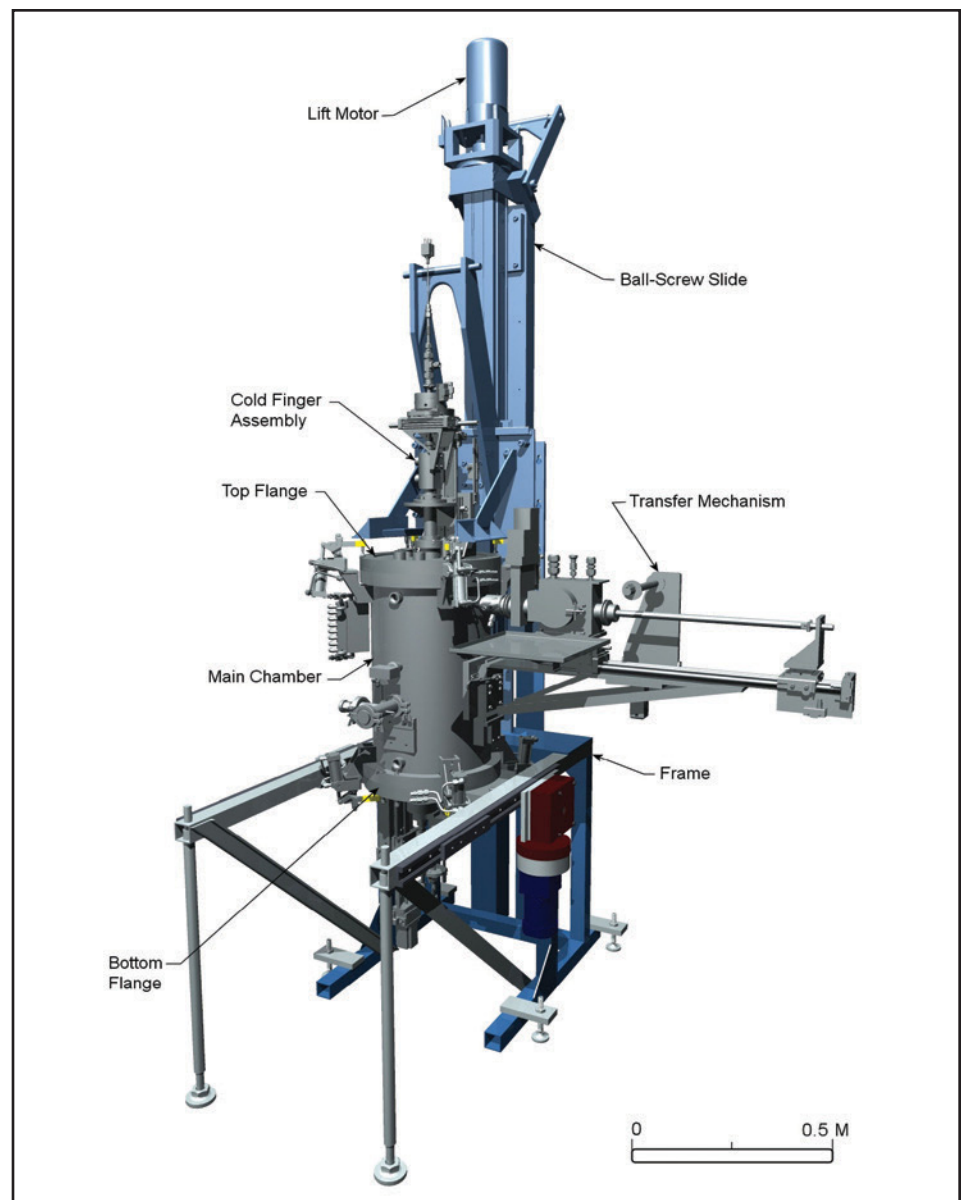


**Figure 2.** Main FACS furnace assembly.

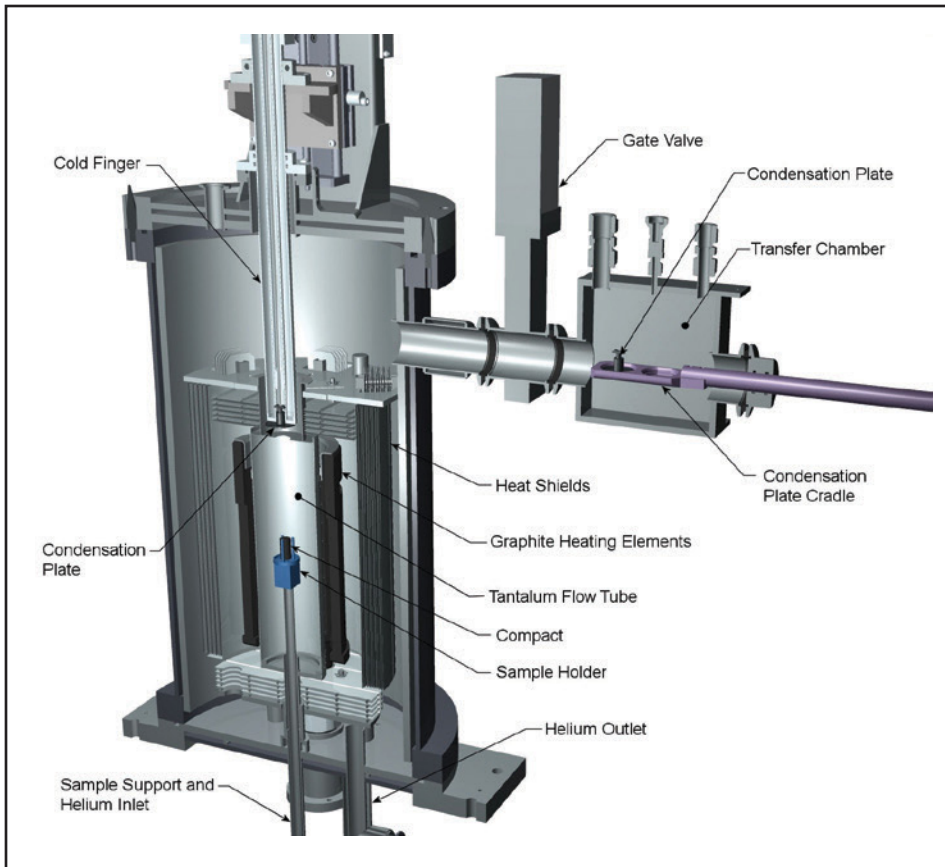


**Figure 3.** Cutaway view of the FACS main furnace chamber, cold finger, and transfer chamber assembly.

The hot zone can accommodate samples up to approximately 75 mm in diameter (which would include, for example, a standard 60-mm-diameter spherical HTGR fuel element). Special sample holders have been designed to accommodate the 25-mm-long  $\times$  12.3-mm-diameter AGR compacts, although any specimen geometry can be accommodated through design of a custom tantalum holder. Ten layered heat shields enclose the heating element and specimen in the center of the furnace while shielding the outer components from the elevated temperatures. These consist of four inner tantalum shields, followed by two molybdenum shields, and finally four stainless steel shields.

A key design feature of the FACS furnace is a water-cooled cold finger that holds a removable 35-mm-diameter stainless steel condensation plate on the end (Figure 3). The cold finger can be positioned such that the steel plate is located immediately above the tantalum flow tube aperture, where it can collect condensable fission products (such as silver, cesium, europium, and strontium) that have evolved from the heated fuel specimen and are swept upwards by the flow of helium during the test. The condensation plates can be exchanged periodically during a test, which allows the time-dependent release of fission products from the fuel to be determined. The condensate plate temperature is monitored with redundant Type J thermocouples.

The exchange of condensate plates was designed to be accomplished automatically, with only minimal operator manipulation. The transfer mechanism (shown to the right of the main chamber in Figures 2 and 3) consists of a transfer chamber with an access port, a pneumatically operated gate valve that isolates the transfer chamber from the furnace main chamber, a small stepper motor coupled to a horizontal ball screw, and a condensation plate cradle. A fresh condensation plate is remotely loaded by the operator onto the cradle via the access port. When a plate exchange is initiated, the cold finger retracts from the hot zone, and the cradle, located at the end of a positioning arm, is moved horizontally beneath the cold finger. The old plate is deposited on the cradle, and a new plate is then positioned with the cradle beneath the cold finger and acquired using the rotary locking action. The entire condensate plate exchange operation is performed automatically by computer control. The operator need only remove the used plate from the cradle once it has been retracted into the transfer chamber and place a fresh plate on the cradle.

After removal from the furnace, the condensation plates are packaged in clean plastic containers and sent to the MFC Analytical Laboratory for analysis. Plate analysis consists of gamma counting using a high-purity germanium (HPGe) detector to measure the inventory of gamma-emitting fission products (including Ag-110m, Cs-134, Cs-137, and Eu-154), followed by acid leaching to remove fission products and analysis of non-gamma-emitting fission products, including Sr-90.

### Fission Gas Monitoring System

Fission gases (including Kr-85 and Xe-133) released from the fuel specimen inside the FACS furnace are carried by the helium sweep gas out of the furnace, through a particulate filter, and then to the fission gas monitoring system (FGMS) for analysis using gamma spectrometry. The FGMS is located outside of the hot cell and consists of dual lead-shielded, liquid-nitrogen-cooled charcoal traps to retain the fission gases, each with an HPGe detector and adjustable collimator. One of the assemblies is shown in Figure 4.

The fission gases adsorb onto the charcoal within the cold trap while the helium exits through the FGMS exhaust. The cold traps are maintained at  $-190^{\circ}\text{C}$  by use of an automated liquid-nitrogen fill system controlled by FGMS software, which was developed at INL. Figure 5 shows a cross-section view of the FGMS cold trap assembly. The cold traps are typically operated in series during a safety test, with fission gases collected in the first trap while the second trap is monitored to determine whether the first trap becomes saturated and can no longer retain fission gas. Alternately, the second trap can be used as the primary in the event of a failure of the first trap or detector.

The FGMS software was designed to collect data continuously during a safety test. Data acquisition times are manually set based on the experimental test conditions. When a test begins, the FGMS software communicates with the FACS programmable logic controller to obtain test time and temperature information. These data are then logged continuously with the spectral data that are collected. The FGMS collects a continual spectrum that runs the duration of the test, and all measurements taken by the FGMS software are performed in near real time, thus eliminating the need for lengthy post processing.

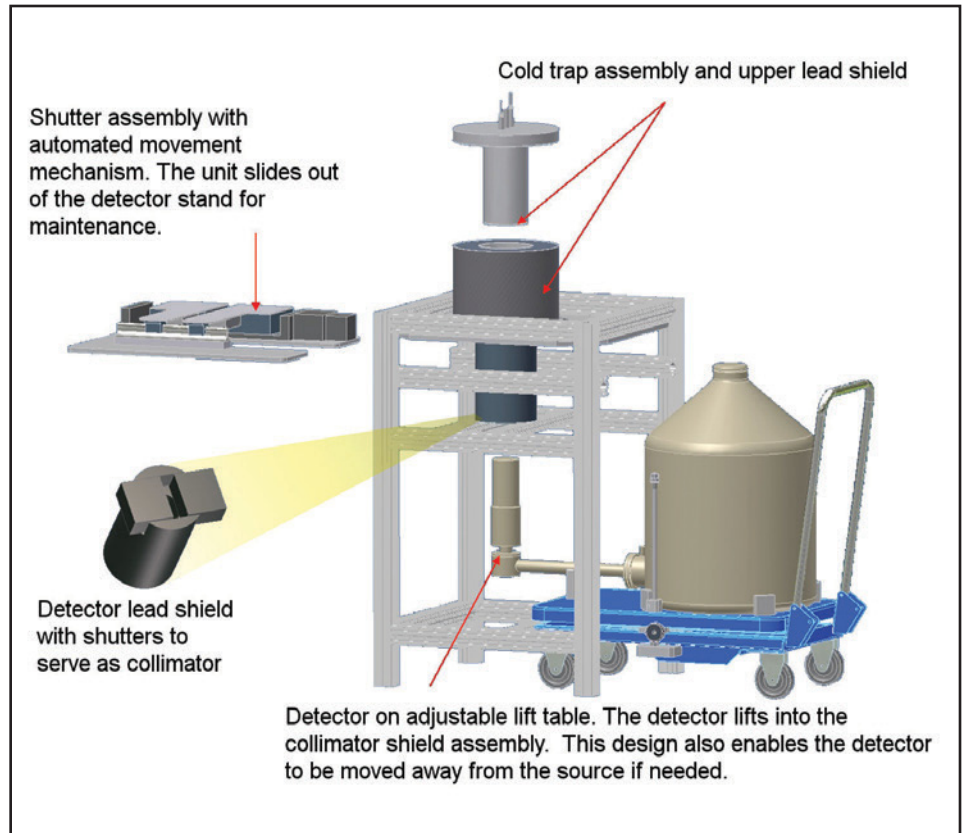


**Figure 4.** Schematic of the FGMS HPGe detector configuration, the collimator/shutter mechanism, and the coldtrap and detector shield assembly.

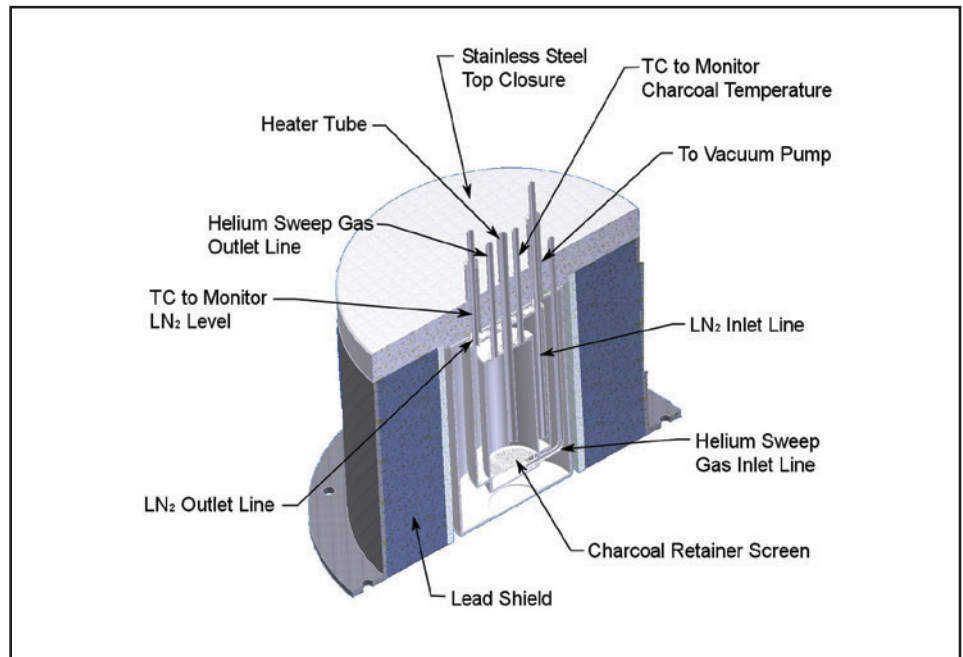


**Figure 5.** Cutaway view of the FGMS coldtrap.

## Results of the First AGR-1 Safety Test

The first safety test of an irradiated fuel compact using the FACS furnace system was performed in April 2013. AGR-1 Compact 6-4-1 was irradiated in the Advanced Test Reactor to a compact average burnup of 13.2% FIMA and a time-averaged, maximum in-pile temperature of 1130°C [1]. During the ramp up to the target furnace temperature, there were intermediate holds at 400°C for 2 hours (to provide adequate time to eliminate moisture from the specimen) and 1250°C for 12 hours (to simulate the operating temperature in an HTGR) before continuing to 1600°C, where the compact was held for 300 hours. The FACS furnace system and the FGMS both performed extremely well during the test, operating as designed with no significant problems. Condensation plates were exchanged at intervals between approximately 12 and 24 hours during the test, while fission gas release was monitored continuously with

the FGMS. A total of 16 condensation plates were used during the test.

After removal from the furnace, the condensation plates were sent to the MFC Analytical Laboratory for analysis. Plates were first gamma counted using an HPGe detector to determine the activity of gamma-emitting fission products on the plates. The collection surfaces of the plates were then treated with nitric acid to remove deposited fission products, and the solutions were analyzed with inductively coupled plasmas mass spectrometry to determine the inventory of non-gamma-emitting fission products. Strontium separation, followed by gas flow proportional counting, was used to determine the Sr-90 inventory. The collection efficiency of a particular element on the FACS condensation plates (i.e., the amount deposited on the plates divided by the amount released from the specimen) is generally less than 100%; therefore a collection efficiency must be used to determine the total inventory

released from the specimen. These collection efficiencies were determined during FACS development and testing and have been used to convert the measured inventories on the condensation plates to the total inventory released from the fuel specimen.

A plot of the release fraction for several fission products during the test is presented in Figure 6. The release fraction is determined by dividing the inventory released from the compact by the predicted end-of-irradiation inventory of the compact based on physics simulations of the AGR-1 experiment [7]. The horizontal dashed line represents the fraction of a fuel compact inventory in a single particle for reference ( $2.4 \times 10^{-4}$ ). The temperature profile for the test is also provided in Figure 6. The data provide significant insights into the behavior of TRISO fuel and specific fission products at elevated temperatures. Because some fission products are released through intact TRISO coatings, some are retained effectively only by SiC, and others are retained by any dense intact coating (IPyC, SiC, or OPyC), the nature of the observed fission product release can provide information regarding failure of various coating layers during the test.

### Kr-85

Fission gas behavior during a high-temperature safety test is critically important because release of fission gas is an indication of a complete failure of all three dense TRISO coatings. As the Kr-85 data in Figure 6 indicate, the fission gas release from Compact 6-4-1 remained extremely low for the duration of the test, reaching a maximum of  $2 \times 10^{-6}$  at the end of the test. This confirms that there were no through-coating failures in Compact 6-4-1 and also that diffusive release of krypton through the intact coatings was very low at 1600°C.

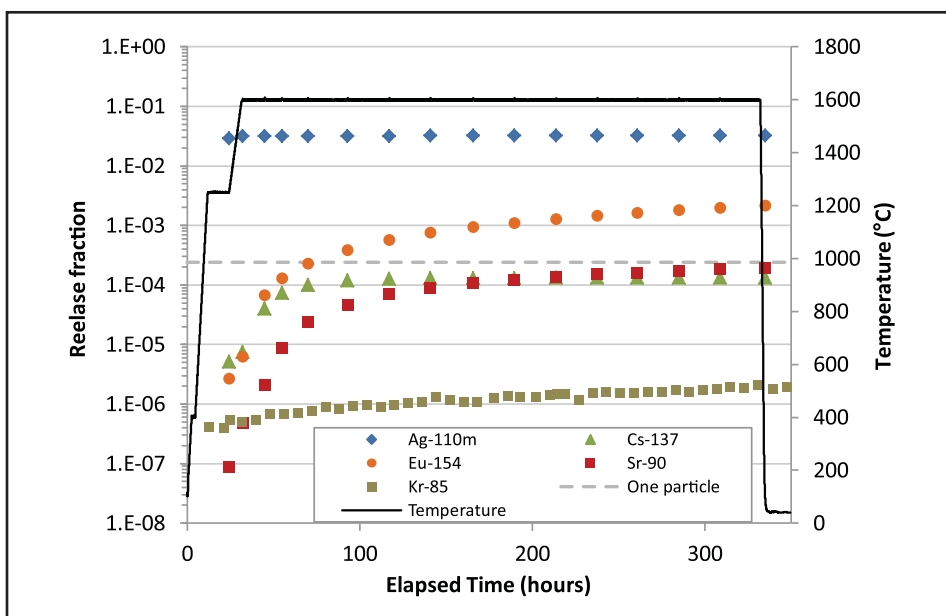


**Figure 6.** Fission-product release fraction from Compact 6-4-1 during heating at 1600°C for 300 hours. The dashed line represents the fraction corresponding to the fission-product inventory of a single particle.

### *Ag-110m*

Silver has long been known to exhibit relatively high release from irradiated TRISO particles [8–10]. While Ag-110m is not a significant concern for offsite dose, once released from the core, it can plate out on internal reactor piping and result in a plant maintenance hazard. In the AGR-1 experiment, the total silver release from individual fuel compacts could range from approximately 0 to 90% during the irradiation [11]. Compact 6-4-1 in particular was found to have retained 56% of the predicted Ag-110m inventory at the end of irradiation, suggesting significant loss of silver in-pile [11].

As shown in Figure 6, approximately 3% of the predicted Ag-110m inventory was released from the compact very early in the test (most of this was released by the end of the initial 12-hour hold at 1250°C). After approximately 1 day at 1600°C, no further Ag-110m release was measured. This behavior is consistent with previous 1600°C AGR-1 safety tests [12]. It is currently believed that this represents rapid release of the silver that was originally released from particles during irradiation, but that was still retained in the compact matrix at the end of irradiation, and that no further significant silver was released from the intact particles during the remainder of the safety test. This is a significant finding, because it indicates a relatively low rate of silver diffusion through intact SiC at 1600°C.

### *Cs-137*

Cesium behavior during high-temperature accidents is extremely important for reactor safety because of the potentially high contribution to offsite dose by Cs-137. Cesium is generally retained well by SiC, but is not as effectively retained by the dense pyrolytic carbon layers. Therefore,

cesium release from the fuel can be a strong indication of an SiC failure, even if one of the pyrocarbon layers in the particle remained intact, providing for good retention of fission gases.

The initial inventory on the plates during the ramp up to 1600°C was below a fraction of  $10^{-5}$  (Figure 6). However, after the experiment reached 1600°C, the cesium release increased dramatically, reaching a value of  $1.3 \times 10^{-4}$  (corresponding to approximately one half of the inventory of a single particle) with very low levels of release after approximately 120 hours at 1600°C. This behavior is similar to that observed in previous AGR-1 safety tests, where post-test analysis confirmed that this is indicative of SiC failure during the test with intact OPyC [13]. Therefore, the results suggest that one of the particles in Compact 6-4-1 experienced a SiC failure early in the test, but at least one of the pyrocarbon layers remained intact as indicated by good krypton retention.

### *Eu-154*

Once the furnace temperature reaches 1600°C, the europium release rate is virtually constant for the remainder of the test. The final release fraction is approximately  $2 \times 10^{-3}$ . Based on additional post-irradiation examination of the AGR-1 compacts, it is unclear whether the level of release observed during safety testing is the result of europium that was released during the irradiation but retained in the compact matrix, or europium is being slowly released through intact TRISO coatings.

### *Sr-90*

The strontium behavior is generally similar to that of europium, although the release fractions are approximately an order of magnitude lower. The release rate for the duration of the test is nearly constant, similar

to releases of europium, and the final release fraction is  $2 \times 10^{-4}$ .

## **Post-Safety Test Destructive Analysis**

---

Compact 6-4-1 will undergo extensive destructive examination that will provide additional information on the fuel performance at elevated temperatures. The analysis will, in general, be similar to that performed on other irradiated AGR-1 fuel compacts [14, 15]. Because Compact 6-4-1 apparently contained a single particle with a SiC layer that failed during the test, it will be of interest to locate this particle for focused examination to help determine the cause of this failure. This can be accomplished by deconsolidating the compact to liberate the individual particles, and gamma counting all ~4,100 particles to locate any that have abnormally low Cs-137 inventory, indicating loss of cesium during the safety test [13]. These particles can then be studied using advanced microanalysis methods to examine the state of the coatings and location of fission products in the coating layers (especially the SiC layer).

## **Conclusions**

---

A capability for high-temperature performance testing of irradiated fuel has been developed at INL. The FACS furnace system can heat irradiated fuel specimens to temperatures as high as 2000°C in pure helium while monitoring the release of fission gases and condensable fission products throughout the test. This is a crucial capability for the VHTR Program, because verification of fuel performance during high-temperature accident conditions is a critical component of fuel qualification.

The first safety test on an irradiated fuel specimen from the AGR-1 experiment using the FACS furnace demonstrated the

excellent performance of the fuel at 1600°C. Very little krypton was released from the fuel, indicating no failures through all TRISO coating layers. A small increase in cesium release during the test is most likely indicative of a SiC layer failure in a single particle in the fuel compact. Europium and strontium were released from the compact at a fairly constant rate during the safety test, with final release fractions of  $2 \times 10^{-3}$  and  $2 \times 10^{-4}$  for Eu-154 and Sr-90, respectively. The data suggest that diffusive release of silver from the particles during the test was extremely small.

Additional tests on the AGR-1 fuel compacts are planned at temperatures as high as 1800°C to establish a database of safety test performance as a function of fuel burnup, fast fluence, and irradiation temperature. These data are essential for developing a better understanding of fuel behavior during reactor accidents and to qualify the fuel in support of licensing a very high-temperature gas-cooled reactor.

## Acknowledgements

The authors gratefully acknowledge the contributions of Lance Cole, Kim Davies, David Laug, and the staff at the INL MFC mock-up shop during FACS furnace development and testing. Kent Dale and Clay Brower are acknowledged for FACS furnace operation support. This work was supported by the U.S. Department of Energy, Office of Nuclear Energy, under the Next Generation Nuclear Plant Project.

## References

1. B. P. Collin, "AGR-1 Irradiation Test Final As-Run Report," INL/EXT-10-18097, Rev. 1, June 2012.
2. P.A. Demkowicz, J.D. Hunn, R.N. Morris, J.M. Harp, P.L. Winston, C.A. Baldwin, and F.C. Montgomery, "Preliminary Results of Post-Irradiation Examination of the AGR-1 TRISO Fuel Compacts," HTR2012-3-021, *Proceedings of HTR 2012*, Tokyo, Japan, October 28 – November 1, 2012.
3. W. Schenk, G. Pott, and H. Nabielek, "Fuel accident performance testing for small HTRs," *Journal of Nuclear Materials* 171 (1990) 19-30.
4. D. Freis, D. Bottomley, J. Etjon, W. de Weerd, H. Kostecka, and E.H. Toscano, "Postirradiation test of high temperature reactor spherical fuel elements under accident conditions," *Journal of Engineering for Gas Turbines and Power* 132 (2010).
5. P.A. Demkowicz, D.V. Laug, D.M. Scates, E.L. Reber, L.G. Roybal, J.B. Walter, J.M. Harp, and R.N. Morris, "The Fuel Accident Condition Simulator (FACS) furnace system for high temperature performance testing of VHTR fuel," *Nuclear Engineering and Design* 251 (2012) 164-172.
6. W. Schenk, D. Pitzer, and H. Nabielek, "Fission Product Release Profiles from Spherical HTR Fuel Elements at Accident Temperatures," *Jülich Report* 2234 (1988).
7. J.W. Sterbentz, "JMOCUP As-Run Daily Depletion Calculation for the AGR-1 Experiment in ATR B-10 Position," ECAR-958, Rev. 1, Idaho National Laboratory, August 2011.
8. H. Nabielek, P.E. Brown, and P. Offerman, "Silver release from coated particle fuel," *Nuclear Technology* 35 (1977) 486-493.
9. W. Amian and D. Stover, "Diffusion of silver and cesium in silicon carbide coatings of fuel particles for high temperature gas-cooled reactors," *Nuclear Technology* 61 (1983) 475-486.
10. P.E. Brown and R.L. Faircloth, "Metal fission product behavior in high temperature reactors—UO<sub>2</sub> coated particle fuel," *Journal of Nuclear Materials*, 59 (1976) 29-41.
11. J.M. Harp, "Analysis of Individual Compact Fission Product Inventory and Burnup for the AGR-1 TRISO Experiment using Gamma Spectrometry," ECAR-1682, Rev. 2, Idaho National Laboratory, June 2013.
12. C.A. Baldwin, J.D. Hunn, R.N. Morris, F.C. Montgomery, G.W. Chinthaka Silva, and P.A. Demkowicz, "First elevated temperature performance testing of coated particle fuel compacts from the AGR-1 irradiation experiment," HTR2012-3-027, *Proceedings of HTR 2012*, Tokyo, Japan, October 28–November 1, 2012.
13. J.D. Hunn, C.A. Baldwin, C.M. Silva, T.J. Gerczak, F.C. Montgomery, and R.N. Morris, "Detection and Analysis of Particles with Abnormal Fission Product Retention," presented at the VHTR Technology Development Office 6th Annual Technical Review Meeting, May 7-9, 2013, Idaho Falls, Idaho.
14. P.A. Demkowicz, J.M. Harp, P.L. Winston, and S. Ploger, "AGR-1 Fuel Compact 6 3 2 Post-Irradiation Examination Results," INL/EXT-12-27123, Idaho National Laboratory, December 2012.
15. J.D. Hunn, R.N. Morris, C.A. Baldwin, F.C. Montgomery, G.W. Chinthaka Silva, and T.J. Gerczak, "AGR-1 Irradiated Compact 6-1-1 PIE Report: Evaluation of As-Irradiated Fuel Performance Using Leach Burn Leach, IMGA, Materialography, and X-ray Tomography," ORNL/TM-2012/233-R0, Oak Ridge National Laboratory, June 2012.



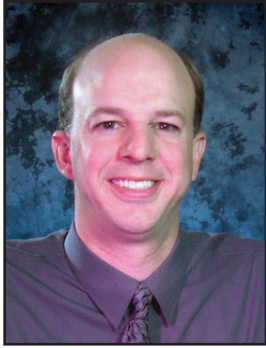
**Paul Demkowicz** (B.S., Ceramic Engineering, University of Washington; M.S. and Ph.D., Materials Science and Engineering, University of Florida) is a Distinguished Staff Scientist at INL. He has worked at INL for the last 10 years, where his current focus is on the development and characterization of fuels for advanced nuclear reactors. Dr. Demkowicz is the technical lead for the post-irradiation examination and high-temperature safety testing of coated particle fuel for the Very High-Temperature Reactor project. He received the 2012 Idaho National Laboratory Director's Award for Exceptional Engineering Achievement for his leadership in establishing post-irradiation examination capabilities for coated particle fuel at INL, which includes development of the FACS furnace.



**Les Scott** (B.S., 1988, General Engineering, Idaho State University) is a senior Process Engineer at the MFC Hot Fuels Examination Facility. He has worked at INL for over 25 years. The majority of his experience has been associated with remote work in the various hot cells located at MFC. He has also worked as a manager for the R&D Support Services organization and as a Lead Engineer and Quality Engineer for the Space Nuclear Systems and Technologies organization during the New Horizons Mission.

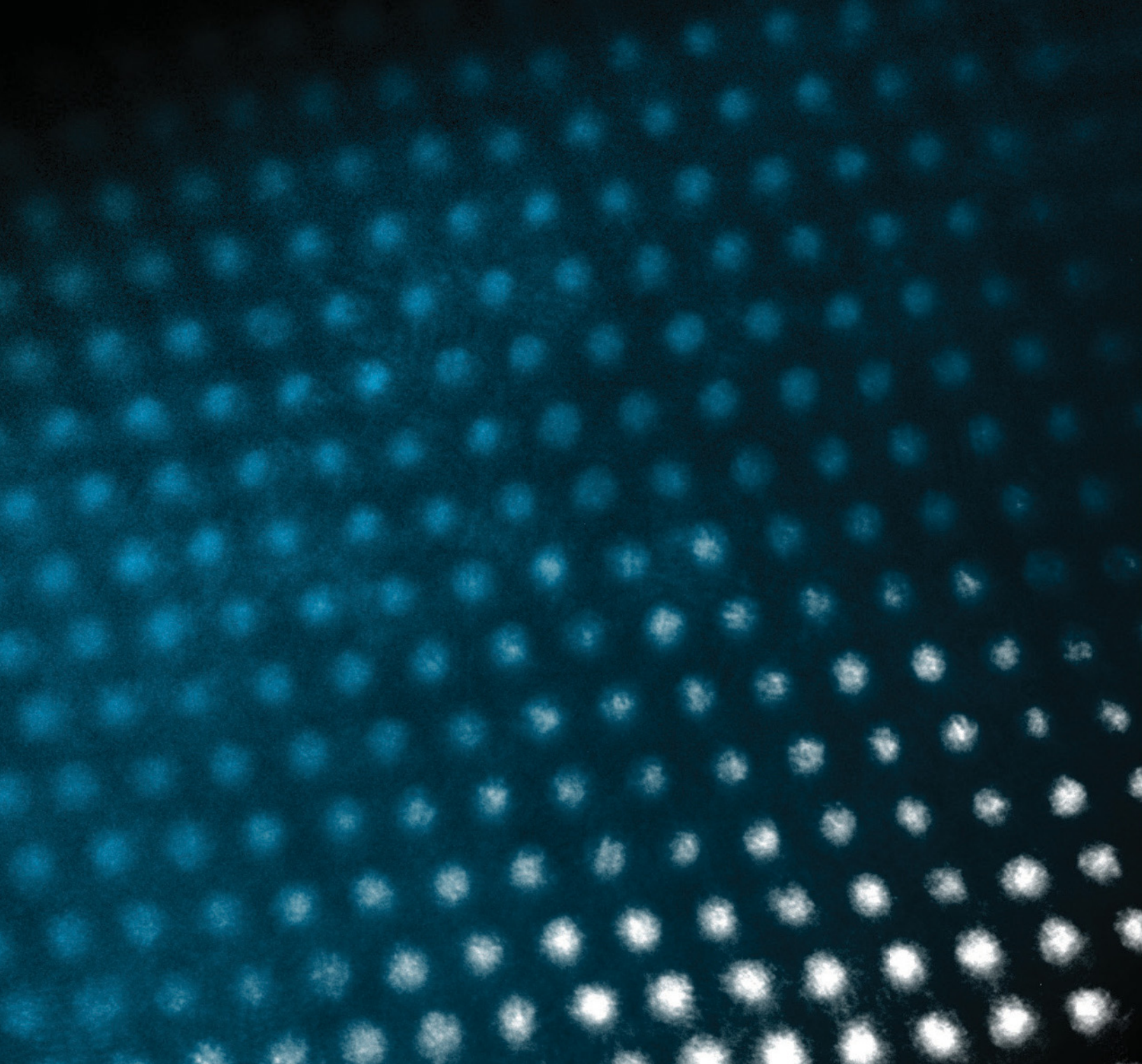


**Dawn M. Scates** (B.S., 1995, Physics, California State University at Bakersfield; M.S., 1999, Physics, Idaho State University) joined INL in 1999 and has worked on many different projects through her 14-year tenure. Her work can be thought of as a cradle-to-grave approach. Dawn is currently the lead researcher for the Fission Product Monitoring System, which involves in-reactor experiments and the FGMS, looking at post-irradiated TRISO fuel. Her research also involves quantifying and relocation activities involving the treatment of transuranic waste, deactivation, decontamination and decommissioning activities involving identifying the location of and identifying the presence of irradiated reactor fuel plates, rods, and pellets using gamma-ray spectroscopy; and nuclear instrumentation/basic nuclear research. In 2009, she received the Laboratory Director's Exemplary achievement award. Dawn is also involved with INL community outreach programs such as "My Amazing Future."



**Edward L Reber** (B.S., 1987, Physics, State University of New York at Geneseo; M.S., 1992, Nuclear Physics, Florida State University; Ph.D., 1994, Nuclear Physics, Florida State University) has worked on many different projects, including being the technical lead for the Idaho Explosives Detection System, nuclear nonproliferation, basic nuclear research, spent nuclear fuel characterization, and gamma-ray spectroscopy of nuclear fuel in-reactor experiments, among others. He joined INL in 1997 following a 3-year postdoctoral fellowship. He has been awarded eight U.S. Patents. In 2005, he received the Christopher Columbus Fellowship Foundation's Homeland Security Award in the Field of Border/Transportation Security.

# **First Reported Identification of Silver and Palladium-Containing Fission Products in Irradiated TRISO-Coated Particles**



# First Reported Identification of Silver and Palladium-Containing Fission Products in Irradiated TRISO-Coated Particles

I. J. van Rooyen, T. M. Lillo (INL), Y. Q. Wu (BSU, CAES)

Evidence of silver (Ag) in the silicon carbide (SiC) layer of irradiated tristructural isotropic (TRISO)-coated particles of the recent AGR-1 experiment at Idaho National Laboratory (INL) was obtained using advanced electron microscopy techniques such as scanning transmission electron microscopy (STEM), electron energy-loss spectroscopy (EELS), and energy-filtered transmission electron microscopy (EFTEM). Silver was identified in SiC grain boundaries, while no silver was identified in the SiC grains. Cadmium was also found in the triple junctions where Ag was identified, but no palladium was found in these triple junctions. Previous work using transmission electron microscopy (TEM) diffraction patterns indexed the micro and nano-sized precipitates as  $UPd_2Si_2$ , while elemental Ag was not conclusively found.

Palladium (Pd) was, however, identified as the main constituent of micron-sized precipitates present at the SiC grain boundaries. Additionally, spherical, nano-sized, palladium-rich precipitates were found

inside the SiC grains. No silver was found in the centre of the micron-sized fission product precipitates using these techniques, although silver was found on the outer edge of one of the Pd-U-Si-containing precipitates that was facing the inner pyrolytic carbon (IPyC) layer.

The identification of silver alongside the SiC grain boundaries and the findings of Pd inside the SiC grains and alongside SiC grain boundaries provide important information needed to understand silver and palladium transport in TRISO fuel, which has been the topic of international research for the past 40 years. The findings reported in this paper lend credence to the hypothesis generated from recent research that Ag transport could be caused by grain boundary diffusion. More work is needed to fully understand the transport mechanisms.

## Introduction

Evidence of the release of metallic fission products through intact TRISO particles has been seen for decades around the world, as well as in the recent AGR-1 experiment at INL [1, 2]. AGR-1, the first in a series of fuel-irradiation experiments planned for the Advanced Test Reactor, began in December of 2006 and ended in November 2009. The relatively high release of silver from some of the AGR-1 fuel compacts and particles [2] accentuates the need to identify and measure silver in the SiC layer. Approximately 25% of the AGR-1 compacts retained less than 50% of their Ag-110m inventory during irradiation. For example, in AGR-1 Compact 6-3-2, analysis indicates that roughly half of the individual particles retained less than 50% of the Ag-110m. Understanding the transport mechanism for silver is important

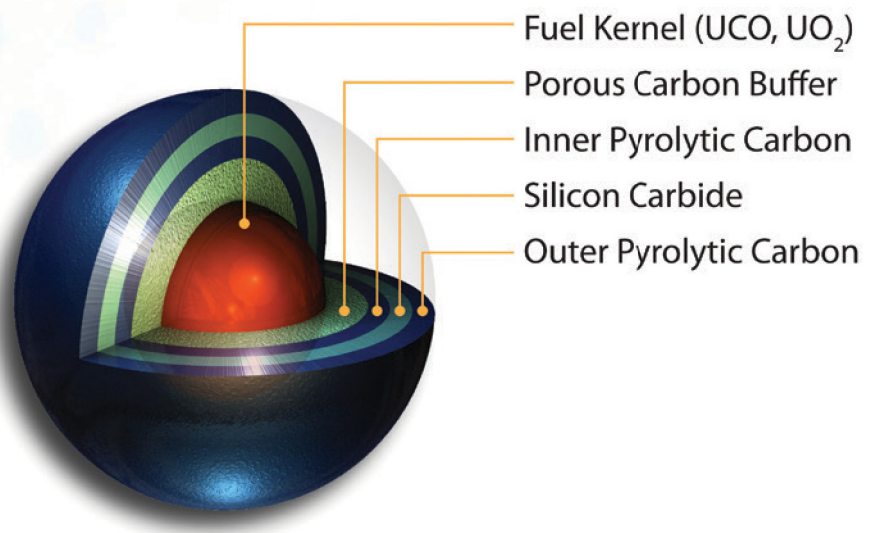


**Figure 1.** Schematic presentation of a TRISO-coated particle

because the TRISO coating is part of the high-temperature gas-cooled reactor's functional containment and is critical for the safety strategy for licensing purposes. Figure 1 shows a schematic presentation of the TRISO particle.

The release of Ag-110m is a potential worker safety concern due to plate-out on the cooler metallic parts of the helium pressure boundary that can pose a risk for maintenance personnel. Although numerous studies have been conducted over the past 40 years, no definitive conclusions about the mechanism responsible for silver transport have been reached. Recent research postulates that Ag transport may be driven by grain boundary diffusion [3–7]. It was also speculated in previous work [8] that Ag would be able to substitute for Pd in a  $U(Ag,Pd)_2Si_2$  solid solution, rather than forming a separate phase, because they have identical atomic radii (both 0.144 nm for the pure elements [9]). Van Rooyen et al. [4] speculated that the Ag transport mechanism might not be attributable to a single factor, but rather to the combined effect of more than one factor.

The initial electron microscopic examination on AGR-1 coated particles using scanning electron microscopy, energy dispersive spectroscopy (EDS), wavelength dispersive spectroscopy, and TEM attempted to identify silver in fission product precipitates, but it was not successful. Although wavelength dispersive spectroscopy has much higher energy resolution than EDS—so that it potentially could distinguish between the overlapping peaks of Pd, U, and Ag (the Ag  $L\beta$  x-ray is separated by 78 eV from the closest Pd x-ray and only 9.6 eV from the nearest U x ray)—the presence of Ag was not confirmed. Even TEM-EDS analysis, using a new silicon drift EDS detector with a normal 0-40-keV range, did not yield conclusive evidence based on the higher-en-

ergy Ag  $K\alpha_1$  peak at 22.166 keV, which avoided overlapping problems between U, Pd, and Ag. However, the initial characterization provided information on the presence of fission product precipitates [8]. These precipitates were located on the SiC grain boundaries within the SiC layer and in the IPyC layer [8].

Palladium is also a metallic fission product of great interest in TRISO fuel. Past studies have shown that Pd can corrode SiC [10-12], and it has been postulated to be a potential failure mechanism at high burnup in low-enriched TRISO fuels when temperatures exceed 1100°C. Neethling et al. [13] showed that Ag transport in SiC took place when present at the SiC surface as a Ag-Pd mixture. No penetration of the SiC layer was found in the absence of Pd. Results of this study (and others) indicate Pd reacts with Si to form  $Pd_2Si$ , and graphite regions form due to the carbon remaining (re-precipitated) after the formation of the silicides. These studies further showed significant Pd corrosion on the SiC-PyC interface. However, in the AGR-1 experiment, no significant Pd corrosion is observed [8]. The Pd and Ag concentrations used in these out-of-pile research studies are orders of magnitude larger than in the actual TRISO-coated particles, which could contribute to the different corrosion behavior observed compared to those seen in the AGR-1 experiment. Our understanding of palladium behavior in TRISO fuel is also incomplete; therefore, it is further explored in this study.

In this paper, the results of the first STEM, STEM-EDS, EELS, and EFTEM obtained from a selected irradiated TRISO fuel particle will be provided and discussed. These results for the AGR-1 experiment have provided new evidence at both the micrometer and nanometer scale that will help improve the understanding of Ag and Pd transport behavior in TRISO fuel.

## Material and Methods

### Material

Because of the importance of silver behavior in TRISO fuel, specific particles were chosen for analysis as part of this study based on the degree of silver retention exhibited during irradiation. Individual particles from selected deconsolidated compacts were gamma counted to measure the activity of various gamma-emitting fission products [2]. The initial results of the advanced electron microscopic examination of Compact 6-3-2 from Capsule 6 are described here. The unique identification number, 6-3-2, is based on the specific capsule, level, and stack number for each compact. Figure 2 identifies the stack and position (or level) numbers in a particular capsule. Compact 6-3-2 refers to the compact in Capsule 6 at Level 3 of Stack 2.

Compact 6-3-2 contains baseline fuel that is fabricated with coating process conditions similar to those used to fabricate historic German fuel because of that fuel's excellent irradiation performance with  $UO_2$  kernels. However, the AGR-1 fuel kernel is made of low-enriched UCO (uranium oxycarbide). Kernel diameters are approximately 350  $\mu m$ , with a U-235 enrichment of approximately 19.7%. Compact 6-3-2 was irradiated to 11.3% fissions per initial metal atom average burnup, 1070°C time-average, volume-average temperature; 1144°C time-average, peak temperature; and an average fast fluence of  $2.38 \times 10^{21}$  n/cm<sup>2</sup>. Based on gamma spectroscopy measurements [2], coated particle AGR1-632-035 was selected because it exhibited a higher than average retention of Ag-110m under irradiation, compared to other particles from the same compact, in the hope that enough Ag would be present to be identified using these advanced microscopic characterization techniques. Particle AGR1-632-035 had a retained Ag-110m fraction of

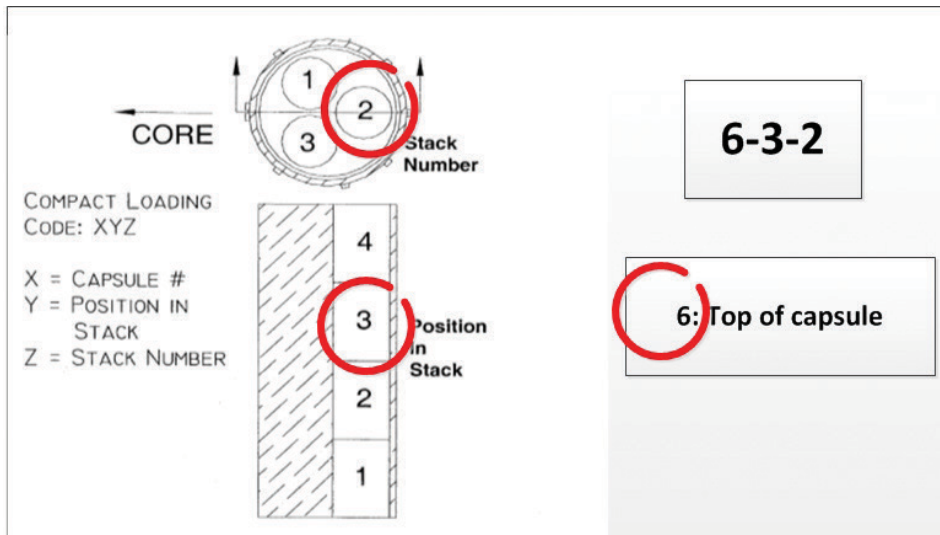


**Figure 2.** Numbering scheme for AGR-I Compact 6-3-2.

0.787 (i.e., it retained 78.7% of the original Ag-110m during irradiation). The total range for the 60 particles analyzed in this compact was 0.075 to 0.882. (Please see [2] for details).

### Methods

The materials used for the coatings on the high-temperature gas-cooled reactor fuel consist of relatively light elements such as carbon and SiC. After irradiation, relatively heavy fission products migrated into these coatings. A high-angle annular dark field (HAADF) detector is best suited for characterization studies, easily differentiating between the pyrolytic graphite and SiC coatings, as well as revealing the distribution of fission products. The HAADF detector in the STEM mode discriminates only differences in atomic number (so-called Z-contrast imaging). This mode is most useful in the identification of small precipitates for further compositional analysis [14].

Compositional analysis of small precipitates and second phases using TEM with EDS requires two main characteristics: (1) a small electron probe (smaller than the feature

under analysis) and (2) the collection of an EDS spectrum suitable for quantification of the elements present. Technological advances in state-of-the-art TEMs have made it possible to form extremely small probe sizes, particularly in the STEM mode, where probe sizes of around 1 nm or smaller are possible. In STEM imaging mode, a small electron probe is scanned across the sample, and an image of the sample is built up, pixel by pixel, from information collected by the HAADF detector below the sample. Generally, the time to collect an EDS spectrum with high signal-to-noise ratio increases as the electron probe size decreases. However, when a high-brightness field emission gun (FEG) is used as the electron source, the EDS spectrum collection time becomes reasonable. The STEM used for the work reported in this paper was conducted with a microscope with an FEG electron source.

In our strategy to identify silver, another analytical tool, EELS, is considered. In TEM, some incoming electrons lose energy when they travel through the specimen due to the inelastic interaction with the specimen's atoms. EELS analyzes the energy distribution of these scattered electrons and provides quantitative compositional information about the nature of the atoms under illumination by the electron beam. The transmitted electrons can be filtered with respect to energy loss, and only those electrons with a specific energy loss (e.g., those associated with Ag) are chosen for imaging. In essence, these filtered electrons with a selected energy loss form an elemental map in the imaging mode (EFTEM).

EELS analysis is considered important for TRISO fuel research because of the specific resolution of elements of interest. In EELS analysis, the chemical sensitivity and the size of resolvable features could be at 1% and smaller than 1 nm, respectively. Moreover, Pd, Ag, and U have close, but separable edge energies in an EELS spectrum, which suggests that trace amounts of Ag in the studied sample may be detected using the EELS technique. The STEM, STEM-EDS, and EELS analyses were conducted with an FEI Tecnai G2 F30 STEM at the Microscopy and Characterization Suite, Center for Advanced Energy Studies (CAES), where low-activity irradiated materials can be examined. Thin, focused ion beam (FIB)-prepared lamellas minimize irradiation dose to a level that allows us to use these advanced techniques at the CAES facility for the irradiated TRISO-coated particles. The specimen was prepared at the Electron Microscopy Laboratory at the Materials and Fuels Complex of INL using the dual-beam Quanta 3D FEG FIB (Figure 3). For this paper, the results obtained from examining the FIB lamella at position 6b are briefly discussed, with more detail in [15]. This lamella was extracted from a location approximately tangent to

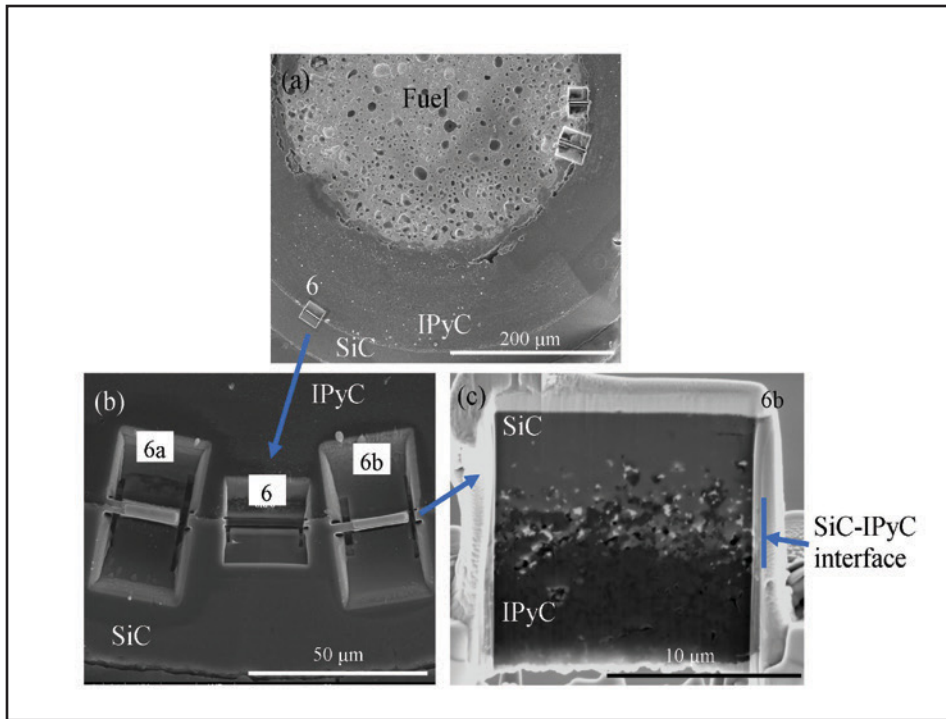


**Figure 3.** Images showing the (a) the cross-sectioned, mounted, coated particle AGRI-632-035, (b) the FIB lamella position 6b, and (c) the AGRI-632-035-6b FIB lamella consisting of the SiC-IPyC interface at higher magnification[15].

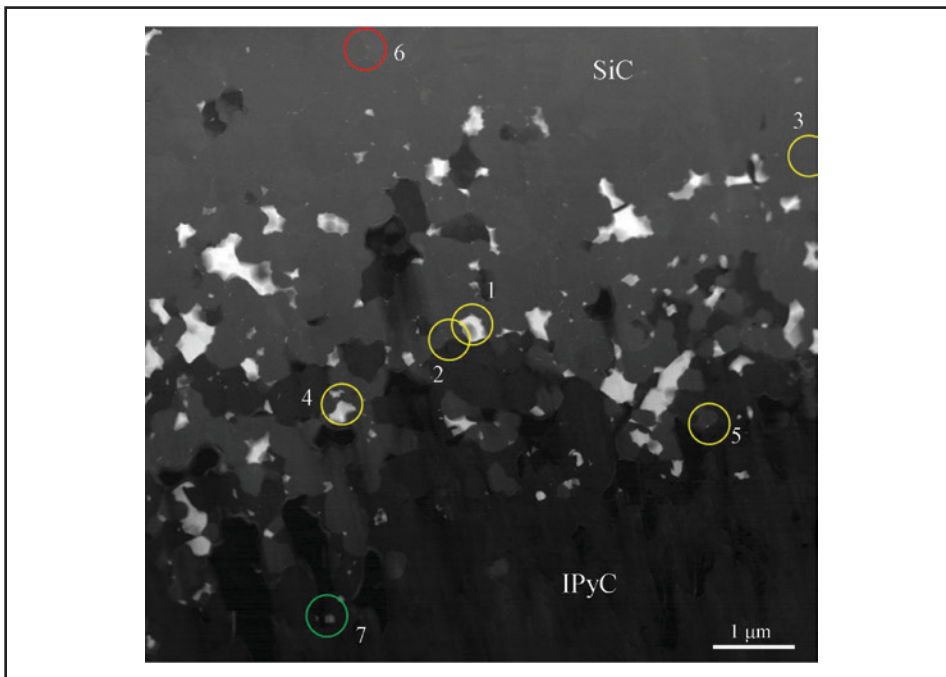


**Figure 4.** STEM Z-contrast micrograph using the HAADF detector showing the three main examination areas: (1) the SiC-IPyC interlayer (yellow numbers 1 to 5), (2) deeper inside the SiC layer (red number 6), and (3) the IPyC layer further away from the SiC-IPyC interlayer (green number 7) [15].

the SiC-IPyC interface and contains parts of both the IPyC and SiC layers as shown in Figure 3c.

### Approach Followed for the STEM Examination

Three areas were identified for the initial STEM examination: (1) the SiC-IPyC interlayer, (2) a region deeper inside the SiC layer, and (3) another region in the IPyC layer farther from the SiC-IPyC interface. During these examinations, attention was given to the precipitates on the outer edge of the SiC-IPyC interface because this is the starting point for the transport of fission products as they move from the IPyC to the SiC. Color-coded numbers, shown in Figure 4, are used to indicate the five areas examined at the SiC-IPyC interface (numbers 1 to 5, yellow color designation), the one area further in the SiC layer (number 6, red color designation), and the one area in the IPyC (number 7, green color designation). The investigation focused on identifying the elemental components in the precipitates using EDS line and spot scans and on determining the physical nature of the precipitates (i.e., inter or intragranular).

### Results and Discussion

#### Identification of Silver

Silver was identified in specific locations in Areas 1–4 using the STEM-EDS detector by focusing at the higher energies associated with K-level transitions of fission products. Figure 5 shows the presence of silver along the grain boundary, leading up to a micron-sized precipitate in Area 1. No silver was found in the precipitate in Area 1, which was predominantly found to contain Pd, U, and Si. The EDS line scan is normalized to the three elements, Pd, U, and Ag.

Silver was identified in both the grain boundaries (marked 1 and 2 in Figure 6), leading up to the triple junction (marked 3 in Figure 6) and in the triple junction itself in the SiC layer near the edge of the IPyC. The EDS spectrum from the center of this triple junction, shown in Figure 7a, identifies the Ag K peak at 22.162 keV. It is also interesting to note that Cd, at 23.172 keV in Figure 7a, is observed in this triple junction, because it had not been found in any other grain boundaries or triple junctions analyzed in these studies. (Cd is a metallic fission product as well.) Also peculiar is that Pd is not observed in this triple junction, although Pd is identified in the SiC matrix adjacent to this triple junction as shown in Figure 7b from the EDS line scan through this triple junction (marked 3 in Figure 6).

Area 3 of Figure 4 was also found to contain grain boundaries with significant concentrations of silver. This area contained a high density of triple junctions in a somewhat curious configuration (see Figure 8). An EDS line scan was performed along the blue line at the triple junction in Figure 8, identifying the presence of silver throughout this particular triple junction. However, this

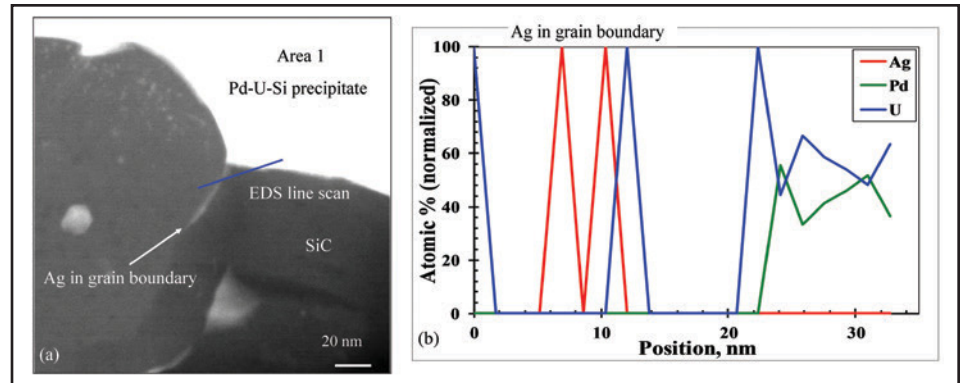


**Figure 5.** Images showing the (a) the HAADF STEM image of a silver-containing grain boundary and (b) the EDS line scan confirming the presence of silver in the grain boundary leading up to the micron-sized Pd-U-Si precipitate [15].

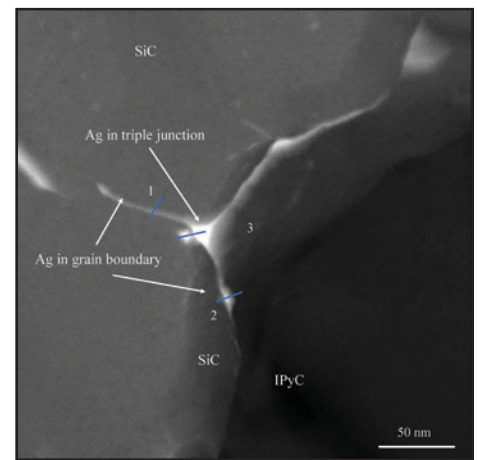


**Figure 6.** Image showing the HAADF STEM image of silver-containing grain boundaries and triple junction at the outmost edge of the SiC adjacent to the IPyC at area 2 shown in Figure 4 [15].

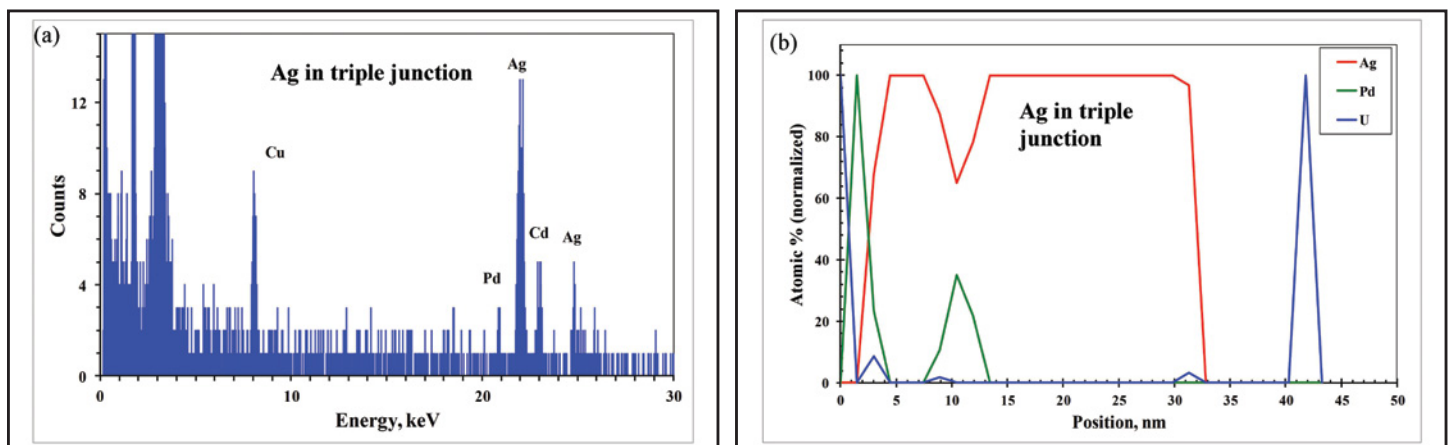


**Figure 7.** Image showing (a) the EDS spectrum, identifying the Ag K peak at 22.162 keV and the presence of Cd in the center of the triple junction shown in Figure 6, and (b) the EDS line scan profile through the triple junction, indicating the presence of Ag. Although no Pd is observed in the triple junction, Pd and U are identified in the SiC matrix adjacent to this triple junction (Cu is an artifact from the grid holder) [15].

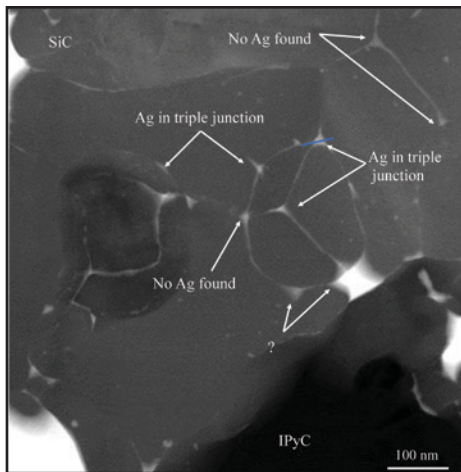


**Figure 8.** Photomicrograph of Area 3, showing the triple junctions analyzed. Junctions found to contain or not contain Ag are indicated, while those where the EDS results for Ag were ambiguous are marked with “?” [15].

was not necessarily the case for all triple junctions in this area. In fact, only four showed significant silver content, while three showed no evidence of silver and two others exhibited only possible indications of silver from extremely small Ag EDS peaks. Additionally, Ag-free (or low Ag concentration) triple junctions appear to be connected to Ag-rich triple junctions via grain boundaries and, thus, suggest that grain boundary character may have an influence on silver transport. Grain and grain-boundary character determination between triple points where silver was found can provide information on preferred orientations for silver transport pathways. Transmission electron back-scattered diffraction analysis of the grain and grain-boundary orientation relationships is being planned for this and other samples in an effort to understand the effect of grain boundary parameters on fission product transport.

However, the fact that not all triple junctions contain silver leads to questions regarding

the role of grain-boundary type on silver transport and collection at triple points. Does this mean, for example, that triple junctions rich in silver consist of one grain boundary capable of easily transporting silver to the triple junction and two grain boundaries incapable of transporting silver efficiently away from the triple junction, thus resulting in a silver-rich triple junction? Or is it that the Ag-free triple junction does not contain a grain boundary that is capable of transporting silver to the junction, while the low Ag triple junctions may have grain boundaries that transport the silver away from the triple junction at a slightly slower rate than the grain boundary supplying the silver to it? Future research work is needed to answer these questions. If these questions can be answered and future work shows that grain boundaries with varying silver transport capabilities do exist, the silver distribution in Figure 7 could be explained. Additional work to characterize the boundaries is required to further understand the potential role that grain-boundary character plays in silver transport.

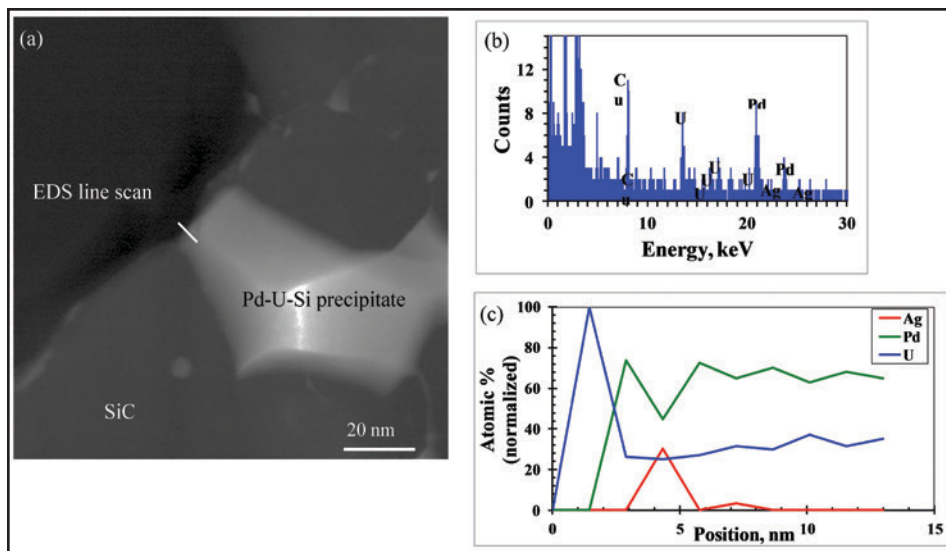


**Figure 9.** (a) Pd,U-containing precipitate on the IPyC/SiC interface showing the location of the EDS line scan in (c); (b) the EDS spectrum from the interior of the precipitate showing significant levels of Pd and U with virtually no Ag present; and (c) the composition profile acquired along the white line in (a) shows silver present at the IPyC/precipitate interface only (Cu is an artifact from the grid holder) [15].

Silver was also found in conjunction with coarse palladium precipitates. Figure 9 shows a palladium and uranium-containing precipitate, as indicated by the EDS spectra (shown in Figure 9b) taken from the center of the bright precipitate. The concentration profile in Figure 9c was obtained from EDS line-scan data, along the white line shown in Figure 9a, spanning the IPyC/precipitate interface and, again, normalized to three elements of interest. A small amount of Ag is found only at the interface between the IPyC and the Pd,U-containing precipitate.

## Identification of Silver using EELS and EFTEM

Ag, Pd, and U can be distinguished by using EELS because their edge energies are separated from each other (i.e., Pd  $M_{4,5}$  335 eV, Ag  $M_{4,5}$  367 eV, U  $N_7$  381 eV) [16]. Therefore, EELS was carried out at Area 2 (Figure 4 and Figure 6), where an Ag-rich intergranular phase was found by EDS (Figure 7) to verify the presence of silver and further investigate its behavior.

Figure 10a is a zero-loss image of the triple-junction area, with the triple-junction phase in darker contrast in this image. The EELS spectra obtained in a range from ~230 eV to ~390 eV (Figure 10b) shows the successful identification of the Ag M-peak (387 eV) at the triple junction of grain

boundaries. This result confirms the presence of Ag found by EDS analysis, as shown in Figure 7. A very small peak at 340 eV is also observed in the spectrum, which likely corresponds to Pd M-peak; therefore, this area may also contain some small amount of Pd.

EFTEM elemental maps of Ag and Si were also obtained at this triple-junction area, as shown in Figure 10c and Figure 10d, respectively. In the EFTEM elemental map, the lighter region corresponds to the elements being analyzed. Therefore, Figure 10c clearly shows the triple-junction phase is Ag-rich and Figure 10d indicates this triple-junction area is located at the boundary between the SiC and IPyC phases. EFTEM elemental mapping was done at four locations of the TRISO sample using the

three-window method at edge energies of Pd  $M_{4,5}$  335 eV, Ag  $M_{4,5}$  367 eV, U  $N_7$  381 eV, C K 284 eV, and Si  $L_{2,3}$  99 eV, respectively. Because the edge energies of Pd  $M_{4,5}$ , Ag  $M_{4,5}$ , and U  $N_7$  are close to each other, the Ag map might contain Pd information and the U map might contain Ag information, respectively. At this time, these EFTEM maps are used only as complimentary information, but with further work on the three-window energy settings, this may be more conclusive. This EFTEM method is of specific interest in this research, because it could provide a means of showing elemental distribution that would assist in understanding the transport of these elements or compounds.

## Identification of Palladium

EDS analyses were also carried out for a large precipitate (Area 1 in Figure 4) about one-half micron away from the triple-junction area where the Ag-rich phase was detected (Figure 6 and Figure 10). Figure 11a is a STEM HAADF image of this precipitate. EDS area scans (~200 nm × 150 nm and ~50 nm × 10 nm) both inside and at the edge of this precipitate reveal that this is a Pd-U-Si phase (Figure 11b). Interestingly, sphere-shaped precipitates of ~10–20-nm size were observed inside the SiC grains in locations near the SiC-IPyC phase boundaries (Figure 12a), as well as approximately 4 μm inside the SiC layer (Figure 12b; Area 6 in Figure 4). These precipitates have a lighter contrast than the SiC matrix in the STEM HAADF images shown in Figure 12a to d. EDS analyses (Figure 12e and f) reveal that these nanoprecipitates are Pd-rich phases. Further work is needed to identify the complete composition and crystal structure of these precipitates.

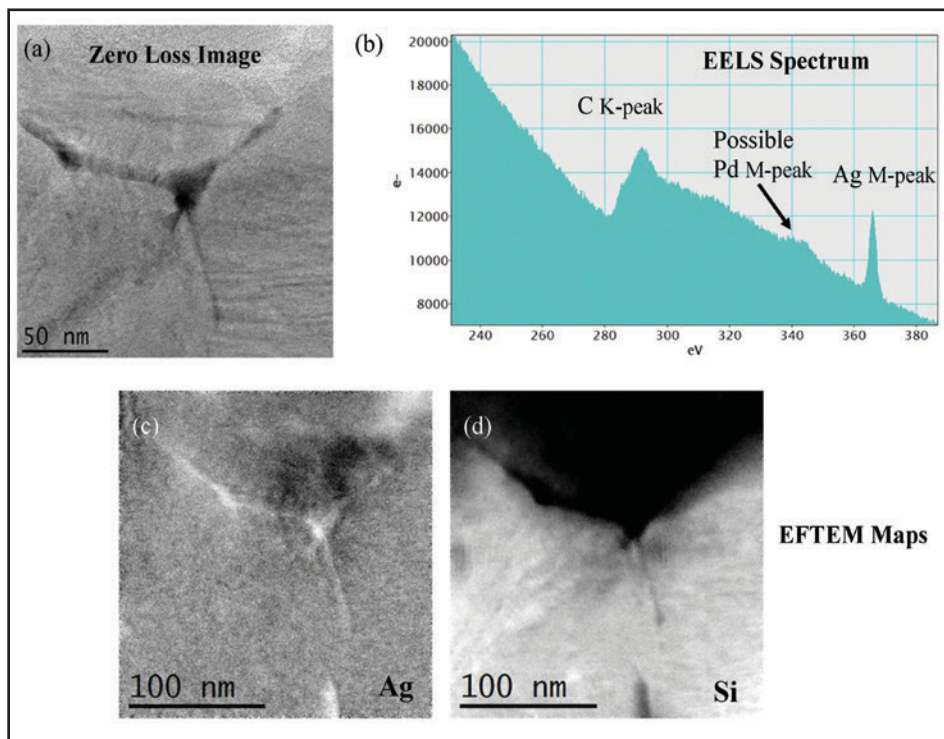


**Figure 10.** Zero-loss image of the second phase at triple junction (a) and corresponding EELS spectrum obtained at this area (b); EFTEM elemental maps of Ag and Si at this area (c) and (d), respectively [15]. In the EFTEM elemental maps, the lighter region corresponds to the elements being analyzed.

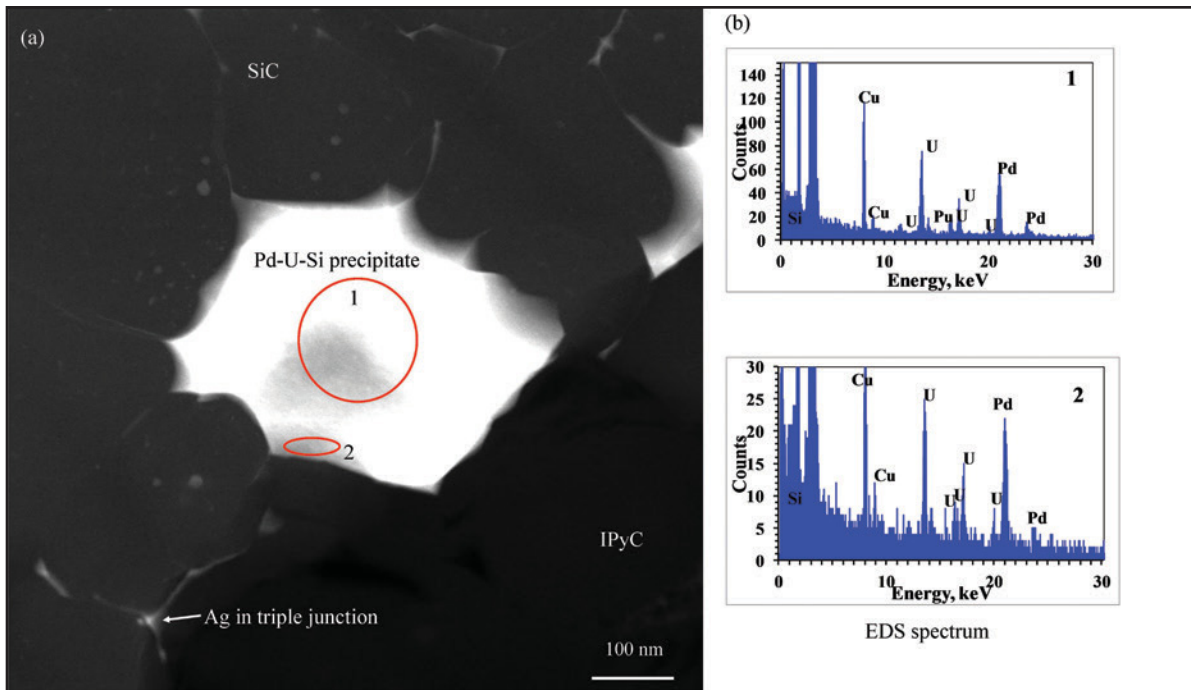


**Figure 11.** A STEM HAADF image of a large precipitate shown in (a) with the EDS area scans ( $\sim 200 \text{ nm} \times 150 \text{ nm}$  and  $\sim 50 \text{ nm} \times 10 \text{ nm}$ ) both inside and at the edge of this precipitate reveal that this is a Pd-U-Si phase (Figure 10b). Ag is detected at the grain boundary extended from this precipitate (Cu is an artifact from the grid holder) [15].

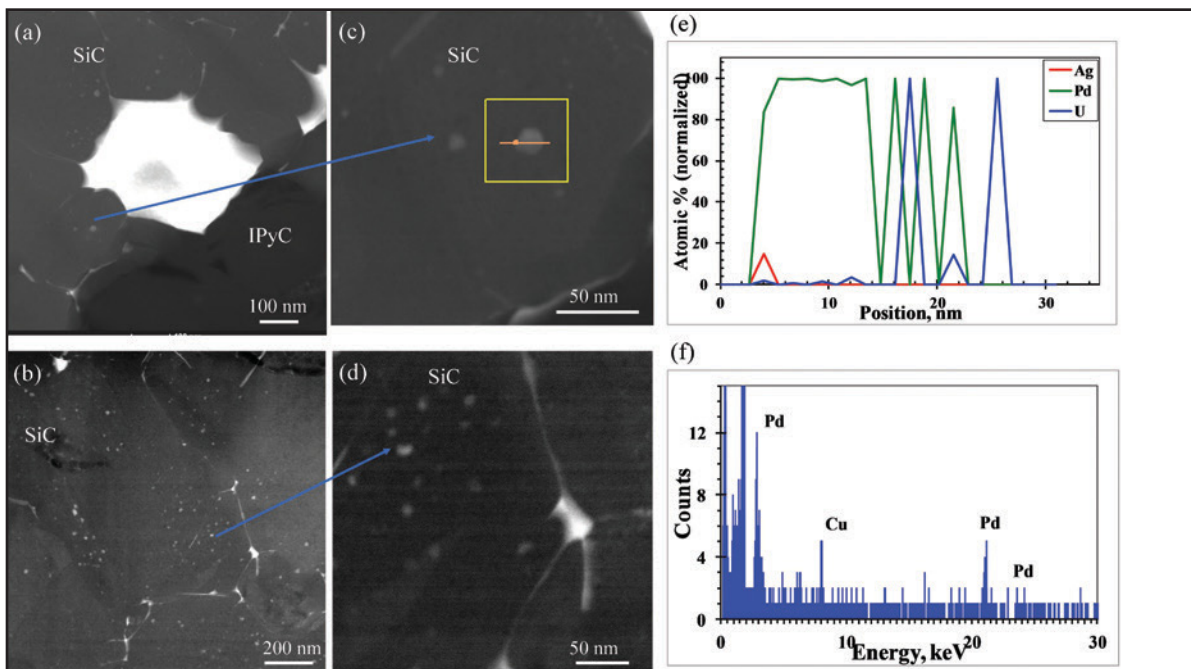


**Figure 12.** STEM HAADF images showing nanometer-size precipitates ( $\sim 10 - 20 \text{ nm}$ ) inside SiC grains (a) at the SiC-IPyC interface and (b) approximately  $4 \mu\text{m}$  inside the SiC layer. The corresponding enlargements are shown in (c) and (d). The corresponding EDS line scans in (e) and (f) revealed that these precipitates contain Pd (Cu is an artifact from the grid holder) [15].

## Conclusions

STEM, EELS, and EFTEM were used to identify, for the first time, the physical location and elemental distribution of fission products at the micro- and nano-scale in the SiC and IPyC layers of irradiated TRISO fuel. Additionally, the STEM examination provided evidence of nano-sized silver precipitates at triple points and grain boundaries in the SiC on the edge of the SiC-IPyC interface up to a depth of approximately 0.5  $\mu\text{m}$ . Silver was also identified using EELS and EFTEM. At this time, the EFTEM maps obtained were used only as complimentary information, but with further work on the three-window energy settings, this may be more conclusive. This EFTEM method is of specific interest in this research, because it could provide a means of showing elemental distribution that would assist in understanding the transport of these elements or compounds.

Because silver was identified in the SiC grain boundary structure, investigations following the silver-containing grain-boundary networks can lead to more clarity on the silver-transport mechanism through the SiC structure. For example, grain and grain-boundary character determination between triple points where silver was found can provide information on preferred orientations for silver-transport pathways. EFTEM maps and detailed EELS analysis on larger (micron-sized) precipitates will provide more compositional detail, while atom-probe analysis will provide three-dimensional elemental maps. This will greatly help to identify and locate the actual atomic positions of Ag and the phase formed. This information will support elucidation of transport mechanisms.

Cd, another metallic fission product, is observed in this silver-containing triple junction. Cd had not been found in any other grain boundaries or triple junctions analyzed in these studies. Also peculiar is that Pd is not observed in this triple junction, although Pd is identified in the SiC matrix adjacent to this triple junction.

Palladium was identified as the main constituent of the micron-sized precipitates present at the SiC grain boundaries, which confirmed preliminary studies by Van Rooyen et al. [8]. Additionally, nano-sized palladium-rich spherical precipitates were found inside the SiC grains. These nano-sized, Pd precipitates were found to be distributed up to a depth of approximately 4  $\mu\text{m}$  away from the SiC-IPyC interlayer. No silver was found in the center of the micron-sized fission-product precipitates using these techniques, although silver was found on the outer edge of one of the Pd-U-Si-containing precipitates that was facing the IPyC layer.

In future efforts, transmission electron back scattered diffraction is being considered for TRISO-coated particle research in parallel to electron back scattered diffraction studies on irradiated SiC. This technique may provide advantages, not only in decreased sample preparation time, but in the quality and resolution of results needed when studying fission product transport in irradiated SiC. This will also provide a direct means to measure the grain characteristics at the exact location where fission product precipitates were identified using the STEM, EELS, and EDS techniques.

## Acknowledgements

This work was sponsored by the U.S. Department of Energy, Office of Nuclear Energy, under U.S. Department of Energy Idaho Operations Office Contract DE AC07 05ID14517. James Madden is gratefully acknowledged for preparation of the FIB samples. Paul Demkowicz provided pre-publication review and comments, which are gratefully acknowledged.

## References

1. H. Nabelek, P.E. Brown, and P. Offerman, "Silver Release from Coated Particle Fuel," *Nucl. Technol.* 35 (1977) 483.
2. P.A. Demkowicz, J.D. Hunn, R.N. Morris, J.M. Harp, P.L. Winston, C.A. Baldwin, and F.C. Montgomery, "Preliminary Results of Post Irradiation Examination of the AGR 1 TRISO Fuel Compacts," Paper HTR2012 3 021, *Proceedings of the HTR 2012*, Tokyo, Japan, October 28 – November 1, 2012.
3. S. Khalil, N. Swaminathan, D. Shrader, A.J. Heim, D.D. Morgan, and I. Szlufarska, "Diffusion of Ag Along  $\Sigma 3$  Grain Boundaries in 3C SiC," *Physical Review B* 84, 214104 (2011) 1-13.
4. I.J. van Rooyen, M.L. Dunzik Gougar, and P.M. van Rooyen, "Silver (Ag) Transport Mechanisms in TRISO Coated Particles," A Critical Review, Paper HTR2012 3 040, *Proceedings of the HTR 2012*, Tokyo, Japan, October 28 – November 1, 2012.
5. E. Lopez Honorato, D.X. Yang, J. Tan, P.J. Meadows, and P. Xiaow, "Silver Diffusion in Coated Fuel Particles," *J. Am. Ceram. Soc.* 93 [10] (2010) 3076-3079.

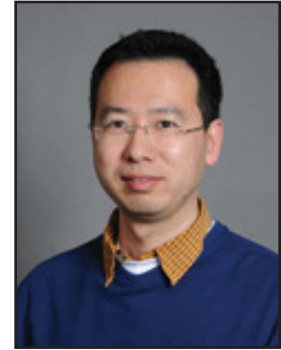
6. I.J. van Rooyen, M.L. Dunzik Gougar, P.M. van Rooyen, and T.Trowbridge, "On Techniques to Characterize and Correlate Grain Size, Grain Boundary Orientation and The strength of the SiC Layer of Triso Coated Particles," A Preliminary Study, Paper HTR2012 3 024, *Proceedings of the HTR 2012*, Tokyo, Japan, October 28–November 1, 2012.
7. R. Kirchhofer, J.D. Hunn, P.A. Demkowicz, J.I. Cole, and B.P. Gorman, "Microstructure of TRISO Coated Particles from the AGR 1 Experiment: SiC Grain Size and Grain Boundary Character," *Journal of Nuclear Materials* 432 (2013) 127–134.
8. I.J. van Rooyen, D.E. Janney, B.D. Miller, P.A. Demkowicz, and J. Riesterer, "Electron Microscopic Evaluation and Fission Product Identification of Irradiated TRISO Coated Particles from the AGR 1 Experiment," A Preliminary Review, Paper HTR2012 3 023, *Proceedings of the HTR 2012*, Tokyo, Japan, October 28 – November 1, 2012.
9. E.A. Brandes and G.B. Brook, eds., *Smithells Metals Reference Book*, Seventh Edition, 1992, Butterworth Heinemann, Ltd.: Oxford.
10. M. Barrachin, R. Dubourg, S. de Groot, M.P. Kissane, and K. Bakker, "Fission-product behaviour in irradiated TRISO-coated particles: Results of the HFR-EU1bis experiment and their interpretation," *Journal of Nuclear Materials*, 415 (2011) 104-116.
11. K. Minato, T. Ogawa, K. Fakuda, H. Sekino, H. Miyanishi, S. Kado, and I. Takahasi, "Release behaviour of metallic fission products from HTGR fuel particles at 1600 to 1900°C," *Journal of Nuclear Materials* 202 (1993) 47–53.
12. P.A. Demkowicz, K. Wright, J. Gan, and D. Petti, "High temperature interface reactions of TiC, TiN, and SiC with palladium and rhodium," *Solid State Ionics* 179, 39 (December 2008) 2313–2321.
13. J. Neethling, J. O'Connell, and J. Olivier, "Palladium assisted silver transport in polycrystalline SiC," AG-PD HTR2010-196
14. D.B. Williams and C.B. Carter, *Transmission Electron Microscopy: A Textbook for Materials Science*, Plenum Press, New York, 1996.
15. I.J. van Rooyen, Y.Q. Wu, and T.M. Lillo, "Identification of Silver and Palladium in Irradiated TRISO Coated Particles of the AGR1 Experiment," *Journal of Nuclear Materials* 446 (2016) 178-186.
16. Gatan's Chart of Inner Shell Loss Edge Types and Energies for Electron Energy Loss Spectroscopy (EELS), iPhone App Store, [www.itunes.com](http://www.itunes.com).



**Isabella J. Van Rooyen** (B.Sc., 1981, Metallurgy, University of Pretoria; B.Sc. Honors, 1983, Metallurgy, University of Pretoria; M.Sc, 1988, Metallurgy, University of Pretoria; MBA, 2003, Business Administration, North West University; Ph.D., 2011, Physics, Nelson Mandela Metropolitan University) is a researcher at INL where she works as the electron microscopic and advanced micro-analysis technique lead for the Very High-Temperature Reactor TRISO fuel development program. In addition to this role, she is the engineering and design lead of a low-enriched uranium conversion fuel program and she is the principal investigator or co-principal investigator of four research projects funded by the national scientific university fund. Prior to joining INL, Dr. van Rooyen held various technical leadership roles in the nuclear, aerospace, and automotive industries in South Africa, most notable the research conducted over 12 years in the nuclear arena, which included the Pebble Bed Modular Reactor Company and NECSA. Dr. van Rooyen has authored or co-authored 19 peer-reviewed journal publications, 16 peer-reviewed conference papers, 11 other conference presentations, three invited lectures and nine workshop presentations. Dr. Van Rooyen has affiliate graduate faculty status at the Nuclear Engineering Department, Idaho State University, as well as affiliated status at CAES.



**Thomas Lillo** (Ph.D., 1994, Metallurgical Engineering, Michigan Technological University) is a staff scientist in the Department of Materials Science and Engineering with 20+ years of experience in materials characterization of high-temperature metallic alloys, intermetallic alloys, ceramics, and composites for power generation applications. He has expertise in the areas of TEM, SEM, OIM, and x-ray diffraction. Additionally, he is directing a study on the high-temperature creep behavior of alloys for the intermediate heat exchanger of the Very High-Temperature Reactor. Dr. Lillo has in excess of 30 technical publications and has collaborated on six patents.



**Yaqiao (Y.Q.) Wu** (Ph.D. in Materials Science and Engineering, 2000, from the Institute of Metal Research, Chinese Academy of Sciences, China) is currently a Research Associate Professor of Materials Science & Engineering at Boise State University, and works at Materials and Characterization Suite, CAES, in Idaho Falls, Idaho. Prior to coming to Boise State University in 2011, Dr. Wu was a research scientist in the Ames Laboratory of the U.S. Department of Energy. Dr. Wu's research interests are in materials design; synthesis; property analysis; nanoscale structure and chemistry characterization; establishing connections between structure, chemistry, and behavior through combinatorial transmission electron microscopy and atom probe tomography techniques. He has been actively investigating various materials' systems (e.g., nanocrystalline magnetic materials, quasiperiodic crystal, radioactive materials, etc.) for over 15 years.

# **EPRI-INL Pilot Project for Characterization of Irradiation- Assisted Stress Corrosion Cracking in Alloys X-750 and XM-19**

# EPRI-INL Pilot Project for Characterization of Irradiation-Assisted Stress Corrosion Cracking in Alloys X-750 and XM-19

J.H. Jackson, S.P. Teysseyre

Following the advent of the Advanced Test Reactor National Scientific User Facility (ATR NSUF), several advances in capability supporting irradiated materials characterization were implemented to address top industry issues. Two of these capabilities were (1) a controlled water chemistry loop installed in the ATR center flux trap and (2) a set of shielded stress corrosion cracking (SCC) test systems. These capabilities are utilized in a cooperative research program between Idaho National Laboratory (INL) and the Electric Power Research Institute (EPRI) to address irradiation-assisted stress corrosion cracking (IASCC), which is regularly cited as a top industry concern with regard to lifetime limiting factors for light water reactors.

## Introduction

As a means of establishing a basis for development and execution of joint ATR NSUF/industry programs, the EPRI and ATR NSUF (through INL) developed a pilot program involving shared costs and responsibilities. The pilot program is designed to do the following:

- Provide a set of data that is relevant to a current industry problem.
- Develop the administrative protocols for cooperative research, such as cooperative agreements and funding between ATR NSUF and industry users
- Develop portions of the research capability and staffing required to address future research and development needs

- Develop a protocol for validation of data with industry, particularly stress-corrosion crack growth rate (CGR) data.

Discussions between ATR NSUF and EPRI identified investigation of the fracture toughness and IASCC growth rates of irradiated high-strength alloys used for boiling water reactor (BWR) repair hardware as an area of interest for an initial project; very little IASCC and irradiated fracture toughness data exist for alloy X-750 (Ni-based alloy, Table 1) and XM-19 (nitrogen-strengthened austenitic stainless steel, Table 2) at the exposure levels of interest, up to a fluence of  $1 \times 10^{21}$  n/cm<sup>2</sup>. Therefore, the focus of this EPRI pilot project is on irradiation and characterization of these alloys in both un-irradiated (baseline) and irradiated states, and it is being conducted in three phases. Phase I and Phase II of this EPRI pilot project have already been completed. Phase I entailed fabrication of the EPRI specimens from materials provided by EPRI [1]. It established the baseline fracture toughness and CGRs of unirradiated material. Phase II of this project entailed design and fabrication of the specimen holders and performance of a safety analysis on a test train to meet EPRI objectives for irradiation of tensile- and compact-tension specimens in the center flux trap of ATR utilizing pressurized water Loop 2A [2]. The current phase of this project, Phase III, will entail performing irradiation and post-irradiation examination (PIE) of the EPRI specimens delivered by EPRI to Battelle Energy Alliance, LLC in Phase I using the test train hardware developed during Phase II.

## Background

Alloys X-750 and XM-19 are used extensively as materials to repair degraded BWR core internals. These materials were selected for their high-temperature/high-strength properties and good corrosion resistance. Although the fleet-wide reactor operating experience regarding SCC for these alloys has been generally favorable to-date, there have been some incidents of cracking and failures of X-750 that have raised concerns regarding its long-term viability as a structurally reliable material in a BWR environment.

In February 2006, an upper tie-rod support bracket made of X-750—similar to the one shown in Figure 1—was found cracked during an in-service inspection. The root cause of the cracking was determined to be SCC. A characteristic of intergranular stress-corrosion cracking in these nickel-base alloys is the transition from a ductile, transgranular fracture mode in an air environment to a predominantly brittle, intergranular fracture mode in the aggressive reactor environment. This recent cracking of X-750 highlighted the need for an improved understanding of these high-strength materials for in-reactor application.

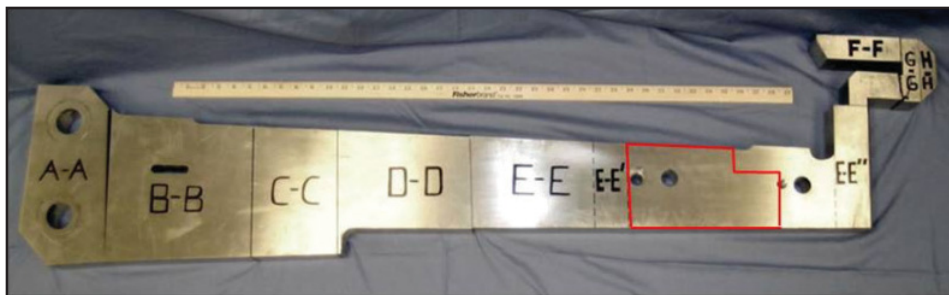


Figure 1. Inconel X-750 support bracket.

Alloy X-750 can exhibit a highly variable microstructure, the effects of which are not understood. SCC resistance of these alloys is not well characterized, especially in a hydrogen water chemistry (HWC) environment. Hydrogen is commonly known to promote embrittlement in nickel-base alloys, leading to decreases in ductility. Additionally, the degradation in material properties due to neutron fluence has not been well quantified. X-750 and XM-19 materials are located in the annulus between the core shroud and reactor vessel and will experience moderate to high levels of fluence, especially if the materials will remain in the reactor through 60 years of operation.

Generation of mechanical property data, SCC growth rates, and stresses required to initiate cracks in these alloys is necessary to determine the long-term viability of currently installed materials. Such information can also

be extremely valuable to hardware designers in reducing the potential for in-service failures. Improvements in fabrication specifications to improve SCC resistance can also be identified and implemented for future hardware.

The EPRI BWR Issue Management Tables (BWRVIP-167, Rev. 1) have determined this topic to be a high priority. This project is aimed at addressing the key knowledge gaps.

### Scope of Work

Samples of two alloys of interest to EPRI were provided to INL during Phase I of this project. The first material was comprised of several sections of Inconel alloy X-750 that were provided to INL by General Electric-Global Research Center (GE-GRC). These sections were removed by GE-GRC from a spare upper support bracket (Figure 1) that

was purchased from Southern Company by EPRI. A decision was made by INL to fabricate all fracture toughness and SCC specimens required for the pilot program from a single section, labeled “E” and outlined in red in Figure 1. The as-received material chemistry is shown in Table 1. The material was delivered in the HTH condition, which consists of a 35% minimum reduction hot roll, solution anneal at 1107°C for 1 hour and rapid cool, and aging at 704°C for 20 hours and air cool.

The second material was comprised of two sections of alloy XM-19 that were provided to INL by GE-GRC. One of the sections was provided in the annealed condition, and the other was cold rolled in a large rolling mill at GE-GRC to induce a total of 19.3% cold work in only two passes. It was decided by the project team to use the 19.3% cold-worked material for the baseline testing performed under this Phase I project to allow comparison to the effect of neutron embrittlement on the annealed material under Phase III of this project. It is expected that both cold work and neutron embrittlement will serve to increase the yield strength of the material and reduce its fracture toughness.

During Phase I of this project, thirty 0.4 T-CT specimens (Figure 2) were fabricated from each alloy; nine American Society for

Table 1. Inconel X-750 composition.														
Al	C	Nb+Ta	Co	Cr	Cu	Fe	Mg	Ni	P	S	Si	Ti	Ta	?
0.77	0.04	0.99	0.726	14.99	0.0151	7.8	0.197	70.8	<0.005	0.002	0.25	2.42	<0.01	0.97

Table 2. XM-19 (Nitronic 50) composition.														
Mo	C	Nb	Co	Cr	Cu	Fe	Mn	Ni	P	S	Si	Ti	W	?
2.17	0.027	0.20	0.016	20.76	0.06	Bal	4.59	12.82	0.014	0.006	0.39	0.001	0.02	0.97

Testing and Materials standard dogbone tensile specimens (Figure 3) were fabricated from each alloy; and approximately 20 3-mm-diameter transmission electron microscopy (TEM) specimens were fabricated from each alloy. Of these specimens, six each of the 0.4 T-CT specimens, three each of the dogbone tensile specimens, and eight each of the TEM specimens were retained for baseline testing. The remaining specimens were set aside for irradiation.

### Baseline Testing

As a part of Phase I of the EPRI pilot project, baseline mechanical properties, including tensile strength, fracture toughness, and (SCC CGR under BWR conditions were determined. The tensile- and fracture-toughness tests were conducted in air at BWR temperature (288°C), and the SCC tests were conducted in simulated BWR HWC and normal water chemistry (NWC) conditions using newly constructed SCC water conditioning and autoclave systems installed at the Center for Advanced Energy Studies. The HWC environment is characterized by a temperature equal to 288°C, under a pressure of 10 MPa; the water chemistry is 63-ppb dissolved hydrogen in ultra pure water with an electrochemical potential equal to approximately  $-420 \text{ mV}_{\text{SHE}}$ . The NWC environment is characterized by a temperature equal to 288°C, under a pressure of 10 MPa; the water chemistry is nominally 2-ppm dissolved oxygen in ultra pure water, with an electrochemical potential approximately equal to  $275 \text{ mV}_{\text{SHE}}$ .

In this article, only the alloy X-750 results are discussed. INL report, INL/EXT-11-24173, “Baseline Fracture Toughness and CGR testing of alloys X-750 and XM-19 (EPRI Phase I)” [1] may be referred to for additional results. Figure 4 is a typical fracture toughness result for the alloy X-750 tested in air at 288°C and Figure 5 is a

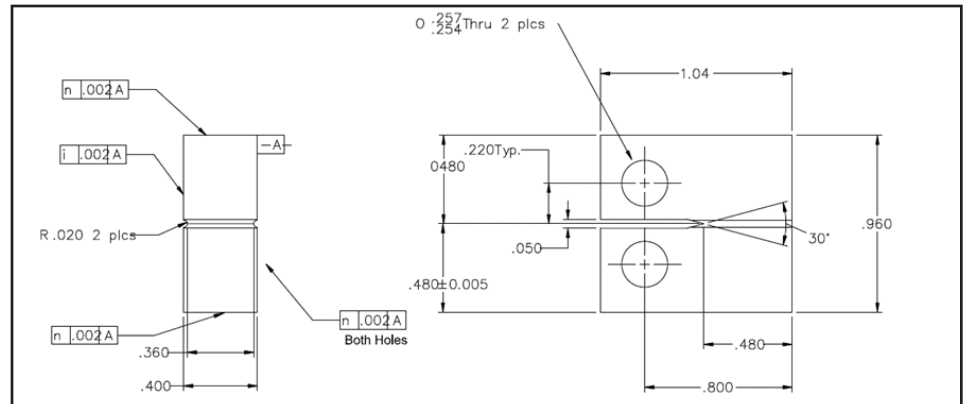


Figure 2. 0.4 T-CT compact tension specimen used for fracture toughness and CGR testing.

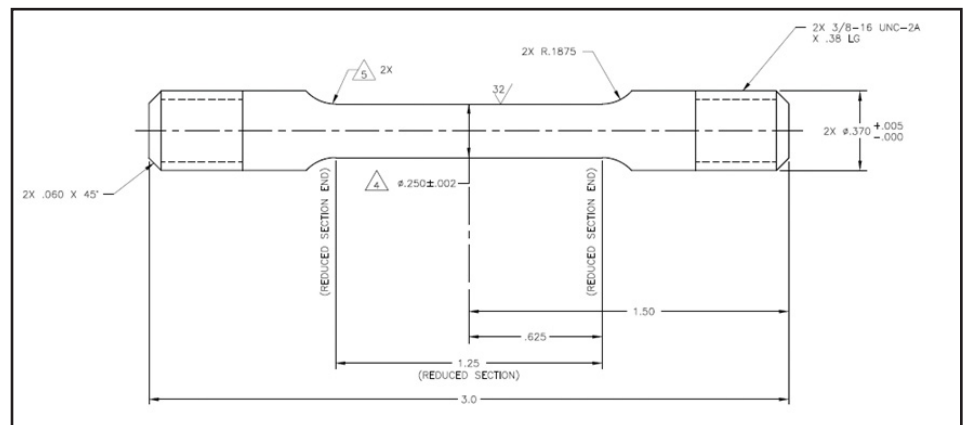


Figure 3. Standard dogbone-type specimen used for tensile testing.

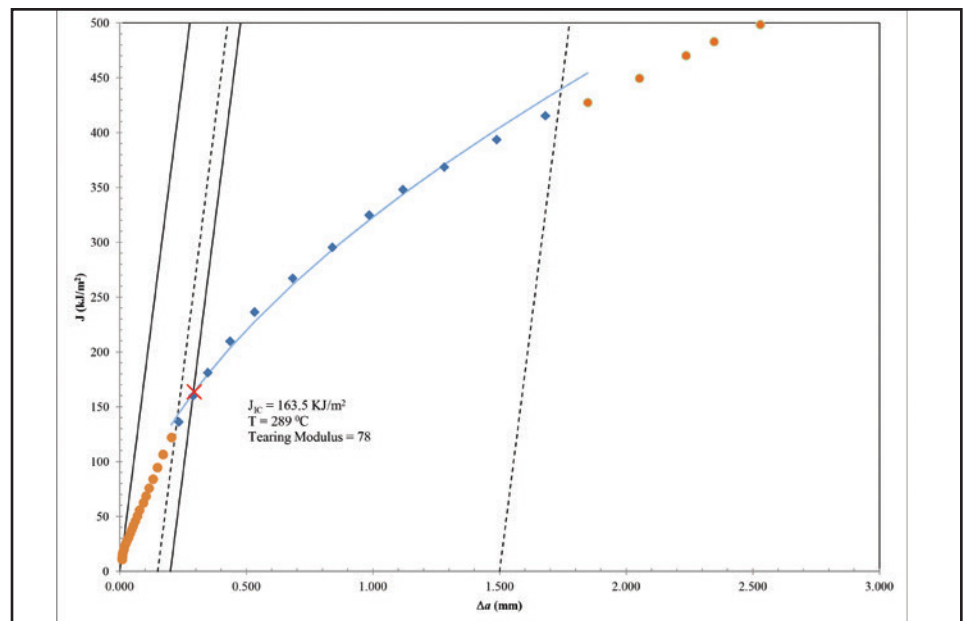


Figure 4. Typical fracture toughness test on inconel alloy X-750 at 288 °C.

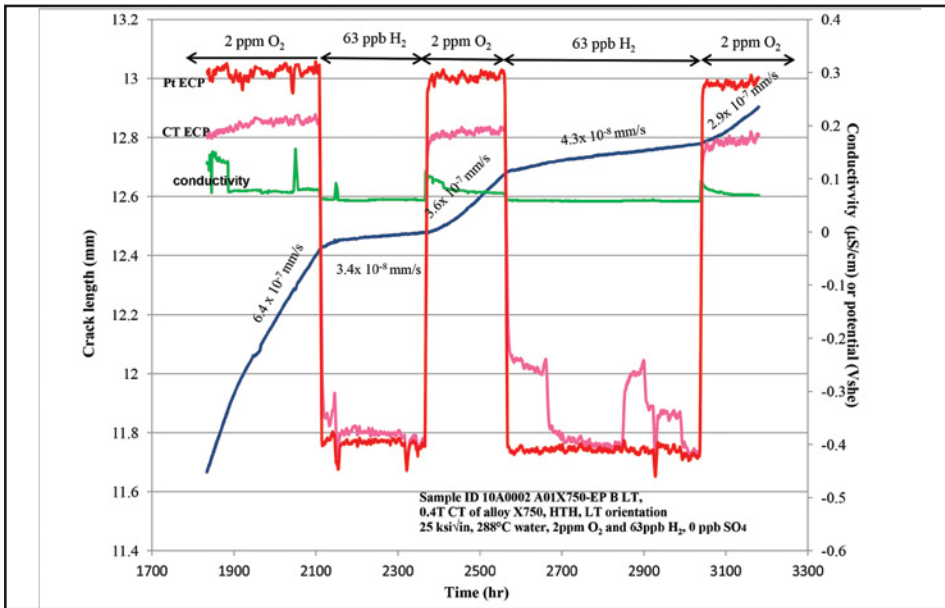


Figure 5. Typical SCC CGR test of Inconel alloy X-750 in BWR, NWC, and HWC environment.

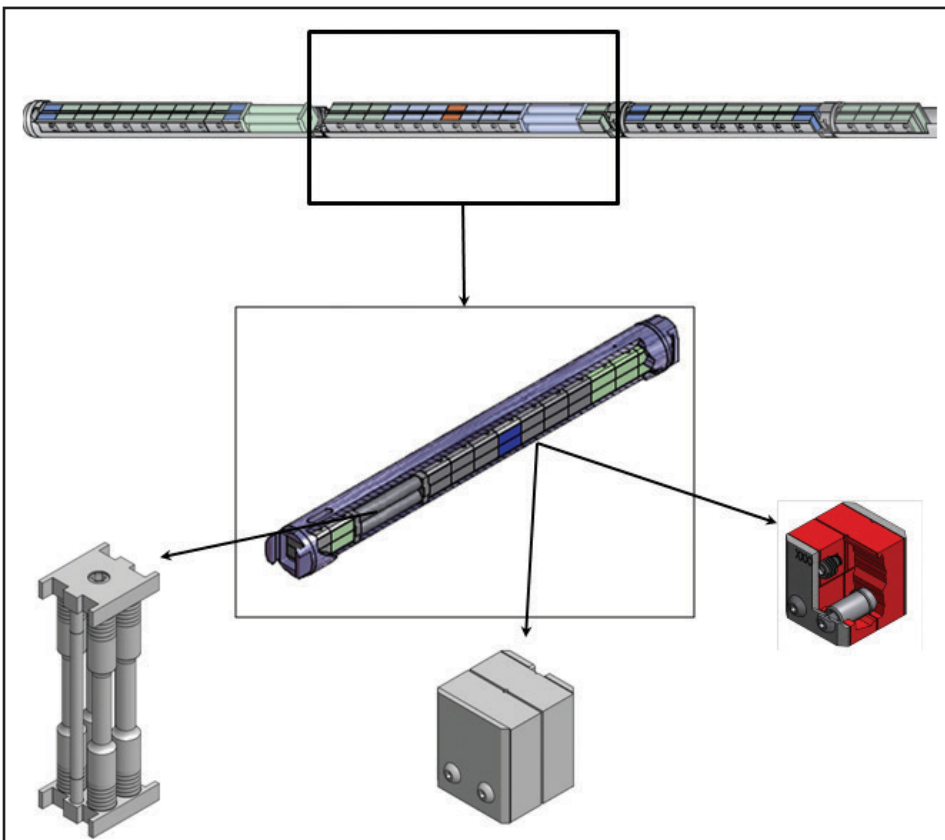


Figure 6. EPRI test train containing packages of 0.4 T-CT specimens, dogbone tensile specimens, and TEM discs packaged inside a 0.4 T-CT blank.

typical SCC CGR test result showing both NWC and HWC CGR trends.

In order to establish the most susceptible crack growth orientation (for SCC CGR), specimens were tested in three orientations with respect to rolling direction of the alloy X 750 plate. These orientations were S-L, T-L, and L-T. Here the S refers to the short transverse direction (thickness of plate), T refers to the long transverse direction, and L refers to the longitudinal or rolling direction of the plate. The first letter refers to the direction of applied force to extend the crack, and the second letter refers to the direction of crack growth. Through this testing program, it was established that, with regard to SCC susceptibility, there was no preferential direction; all exhibited similar CGR trends. In order to maintain consistency with the actual observed material failure, the L-T orientation was chosen for all ensuing testing.

The measured 0.2% offset yield strength of alloy X-750 at 288°C was nominally 714 MPa and ultimate strength was nominally 1,079 MPa. Nominal fracture toughness (i.e., JIC) was 160 kJ/m<sup>2</sup>. SCC CGRs with the material exposed to BWR NWC were on the order of  $5 \times 10^{-6}$  mm/s and for the BWR HWC environment, they were on the order of  $5 \times 10^{-7}$  mm/s. All measured values compared well with expected values and served as a validation of INL's capability for performing these types of tests.

### Test Train Design

The design of the ATR irradiation test train is based on a Naval Reactors design for irradiation of full-sized compact tension specimens in a flux trap water loop. This design features a zirconium body with a low neutron absorption cross section and stacking of pairs of 0.4 T-CT specimens, with spacing to allow flow of the loop coolant in order to maintain a target peak centerline temperature of approximately 288°C. In order to minimize variability in fluence accumulation among specimens, the specimens were situated in the test trains such that they primarily lie within the center 18 inches of the ATR core, thus taking advantage of the “flat” region of the axially symmetric ATR flux profile. Figure 6 shows an overview of the test train and detail of specimen packages that are stacked in the test train. Figure 7 shows the location of the test train relative to the ATR flux profile.

### Irradiation and Planned Post-Irradiation Examination

Three irradiation levels were chosen for this project, based on expected fluences for in-service components and based on expected transition levels for microstructural phenomena. These three target levels are shown in Table 3. All three irradiations utilize the newly installed Loop 2A in the ATR center flux trap for irradiation to control temperature during the irradiation campaign. Capsules EPRI-1 and EPRI-2 utilize short (i.e., 5 and 14-day, respectively) cycles in order to achieve the low target fluences. EPRI-3 will be irradiated in the center flux trap for two full cycles and will also contain several specimens for a Nuclear Regulatory Commission work-for-others project.

During irradiation, the temperature and water chemistry will be controlled in Loop 2A to standards agreed upon by EPRI and INL. The nominal irradiation conditions are shown in Table 4. Although the primary function of the water loop for these irradiations is to control temperature, BWR conditions are targeted to avoid unnecessary corrosion during the irradiation campaigns.

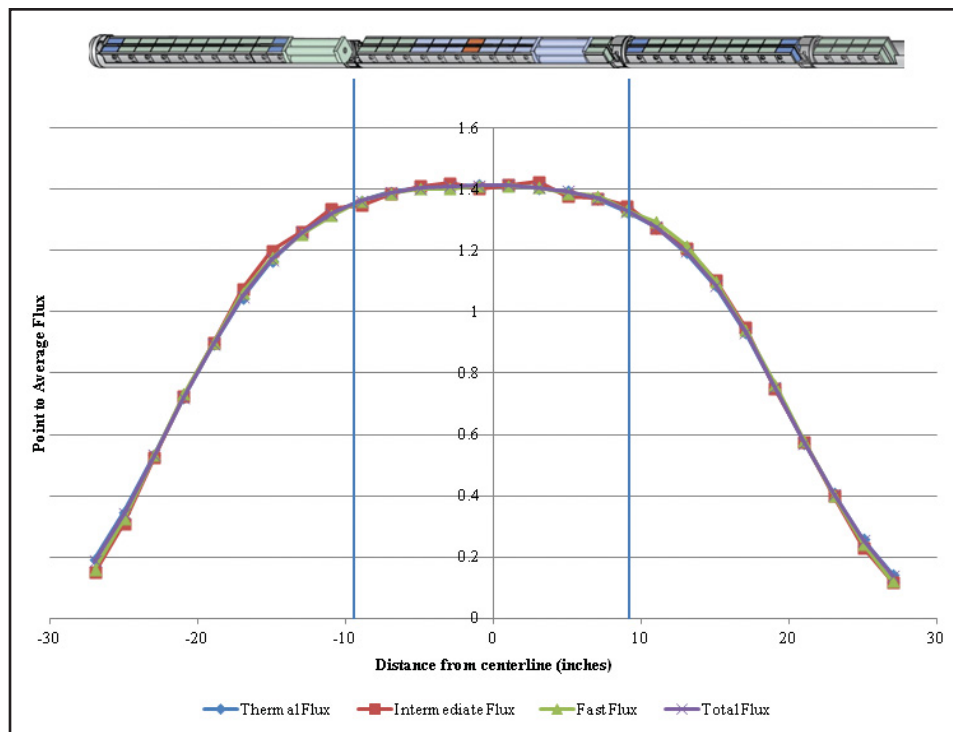


Figure 7. Location of EPRI test train relative to the ATR flux profile.

Table 3. Target irradiation levels and ATR insertion dates.		
Specimen Holder (Experiment) Designation Capsule ID	ATR Insertion	Approximate Fluence (E>MeV)
EPRI-1	May 2014 (156B)	$5.0 \times 10^{19}$
EPRI-2	March 2013 (153B)	$2.0 \times 10^{20}$
EPRI-3	October 2013 (155A)	$1.0 \times 10^{21}$

<b>Table 4. Nominal irradiation conditions for EPRI experiment.</b>	
Design Life	3 Years
Design Temperature	
In-Vessel Portion of the Experiment	325°C
Target Specimen Temperature	288°C ±8°C
Design Pressure	
In-Vessel Portion of the Experiment	2,150 ± 50 psig
IPT Coolant Flow	
Standard In-Pile Tube Flow Rate (maximum)	80 gpm
Standard In-Pile Tube Flow Rate (minimum)	20 gpm
Coolant Chemistry	
Dissolved oxygen	0 - 2,000 ppb
Conductivity	0.1 μS/cm -μS/cm
Chloride	< 200 ppb
Miscellaneous	
pH	7 +0.3/-0.0
Nominal Target Fluence (n/cm <sup>2</sup> )	EPRI-1: 5x10 <sup>19</sup> EPRI-2: 2x10 <sup>20</sup> EPRI-3: 1x10 <sup>21</sup>
Center Flux Trap Power	22-25 MW (nominal) 44-50 MW (PALM cycle)
Corrosion Allowance, (corrosion will be based on loop chemistry which will be controlled)	Zero (negligible)
Reactor Startup, Shutdowns, SCRAM Recoveries	18/year

Following irradiation, the specimens will be cooled in the ATR canal for at least 60 days and then shipped to the INL Hot Fuel Examination Facility in order to disassemble and process the specimens. Tensile tests will be conducted in the Hot Fuel Examination Facility, utilizing the 50-kN capacity Instron test frame, following disassembly of the irradiation capsules. The compact tension specimens will be shipped to the newly constructed IASCC test cells, located at the Materials and Fuels Complex Fuels and Applied Sciences Building, using a specially modified GE-100 transfer cask. They will then be subjected to CGR tests in simulated BWR, NWC, and HWC environments identical to the baseline test environments utilized for Phase I of this project. Fracture toughness tests will also be conducted on several specimens. The CGR and fracture toughness results will be compared to those obtained during baseline testing to determine the effect of neutron fluence on IASCC susceptibility and fracture toughness.

<b>Table 5. PIE test matrix for EPRI Pilot Project.</b>							
	Fluence (n/cm <sup>2</sup> )	# of Fracture Specimens (CT Specimens)	# of IASCC Specimens (CT Specimens)	# of CT Specimens (Backup)	# of Dogbone Tensile Specimens	# of TEM Specimens	
In Air	5.00E+19	2		1	2	4	
	2.00E+20	2		1	2	4	
	1.00E+21	2		1	2	4	
NWC	In Environment with Fatigue Precrack	5.00E+19					
		2.00E+20					
		1.00E+21					
	In Environment with SCC "Prcrack"	5.00E+19		1	1		
		2.00E+20			1	1	
		1.00E+21			1	1	
HWC	In Environment with Fatigue Precrack	5.00E+19					
		2.00E+20					
		1.00E+21		2		1	
	In Environment with SCC "Prcrack"	5.00E+19			1		
		2.00E+20			1		
		1.00E+21		2	1	1	
Total		10	6	8	6	12	

In addition to the mechanical testing performed, several TEM specimens will be analyzed to determine the effect of neutron fluence on material microstructure. These results will provide insight into the progression of microstructural damage as a function of exposure of these materials to reactor environments.

Table 5 is an overall post-irradiation examination test matrix for this project.

## Summary

---

The EPRI X-750 and XM-19 pilot project is one of the first ATR NSUF/industry projects and it will be the first project that utilizes the newly installed Loop 2A in the ATR center flux trap. This project will also be the first project to utilize the recently constructed IASCC test rigs that have been installed at the Materials and Fuels Complex Fuels and Applied Sciences Building. These test rigs were completed based on feedback from industry that IASCC was one of the top issues with regard to lifetime extension of the existing reactor fleet. The project will be a demonstration of INL capability to contribute relevant data toward mitigation of the IASCC issue in the worldwide light water reactor fleet. Additionally, it will serve to develop the protocol necessary to perform industry projects through the ATR NSUF, with INL as the centerpiece, and will provide a baseline for future collaborative research projects involving ATR NSUF, industry participants, and university participants.

## References

---

1. J.H. Jackson and S.P. Teysseyre, "Baseline Fracture Toughness and CGR testing of alloys X-750 and XM-19 (EPRI Phase I)," INL/EXT-11-24173, Rev. 2, October 2012.
2. C.R. Tyler, P.E. Murray, and J.W. Nielsen, "CRADA EPRI Phase II Design Report," INL/LTD-12-24400, March, 2012.



**John H. Jackson** (Ph.D. and Master's degrees in Mechanical Engineering from the University of Washington, Seattle, Washington, and a B.S. in Mechanical Engineering Technology from Central Washington University in Ellensburg, Washington) is a distinguished staff scientist at INL. He has over 15 years of experience in the areas of mechanical testing and fracture mechanics. Dr. Jackson specializes in solid mechanics, nonlinear fracture mechanics, hybrid experimental/numerical analysis, and non-conventional mechanical testing techniques. He also has over 3 years of experience in extreme environment materials characterization and drilling mechanics at the ExxonMobil Upstream Research Company. He currently is the ATR NSUF industry programs lead, and is responsible for research in support of Light Water Reactor Materials lifetime prediction for the ATR NSUF.



**Sebastien Teysseyre** (Ph.D. in Material Science and Engineering), is a senior staff scientist at INL. He has over 10 years of experience in the area of environmental degradation of materials in nuclear power systems, more specifically stress corrosion cracking, effect of irradiation on materials, and IASCC. Before joining INL, he worked for the Department of Nuclear Engineering of the University of Michigan where he studied stress corrosion cracking and IASCC of structural materials for the GEN IV supercritical water-cooled nuclear reactor concept.

# Laser-Based Characterization of Nuclear Fuel Plates

# Laser-Based Characterization of Nuclear Fuel Plates

J.A. Smith, D.L. Cottle, B.H. Rabin

The integrity of fuel-clad and clad-clad bonding in nuclear fuels is important for the development of new fuels; however, the measurement of bond strengths in actual fuels has proved challenging. The laser shock-wave technique (LST) originally developed to characterize structural adhesion in composites is being employed to characterize interface strength in a new type of plate fuel being developed at Idaho National Laboratory (INL). LST is a non-contact method that uses lasers for the generation and detection of large-amplitude acoustic waves and is well suited for application to both fresh and irradiated nuclear fuel plates. Initial characterization results are reported for fresh fuel plates manufactured by different processes, including hot isostatic pressing, friction stir welding, and hot rolling.

## Introduction

The U.S. National Nuclear Security Agency oversees the Global Threat Reduction Initiative, which is tasked with minimizing the use of highly enriched uranium (HEU) worldwide. A key component of that effort is the conversion of research reactors from HEU to low-enriched uranium (LEU) fuels. A novel fuel is being designed to replace HEU. The new LEU fuel is based on a monolithic fuel meat made from a uranium-molybdenum (U-Mo) alloy foil encapsulated in Al-6061 cladding, with thin Zr diffusion barrier interlayers between the U-Mo and cladding. To support the fuel qualification process, new techniques are being developed to fill the need for characterizing bond strengths for the clad-clad and fuel-clad interfaces.

As shown in Figure 1a, the monolithic fuel is based on a rolled U-Mo alloy foil (typically 0.2 to 0.4-mm thick) that is covered with a thin (typically 25- $\mu\text{m}$  thick) Zr diffusion barrier layer and then clad in Al-6061 by a hot isostatic pressing (HIP) process. This monolithic fuel has shown promising results in irradiation testing.

Monolithic fuel is fundamentally different from historical dispersion fuels used in most research reactors. The fuel-clad interface has a Zr diffusion barrier, producing a complex microstructure which evolves over time. The mismatch in properties across the interface results in localized stresses during fabrication and irradiation. Similar to dispersion

fuels, the clad-clad interface in monolithic fuel provides the primary barrier for fission product retention. Even though the new HIP manufacturing process produces fuel plates that pass traditional ultrasonic testing (UT) and bend-test inspections, they do not meet the historical criteria for grain growth across the interface that was used to qualify the previous roll-bonding manufacturing process. Therefore, a critical need exists to establish new evaluation methods and criteria supporting fuel qualification, process development, and manufacturing process qualification.

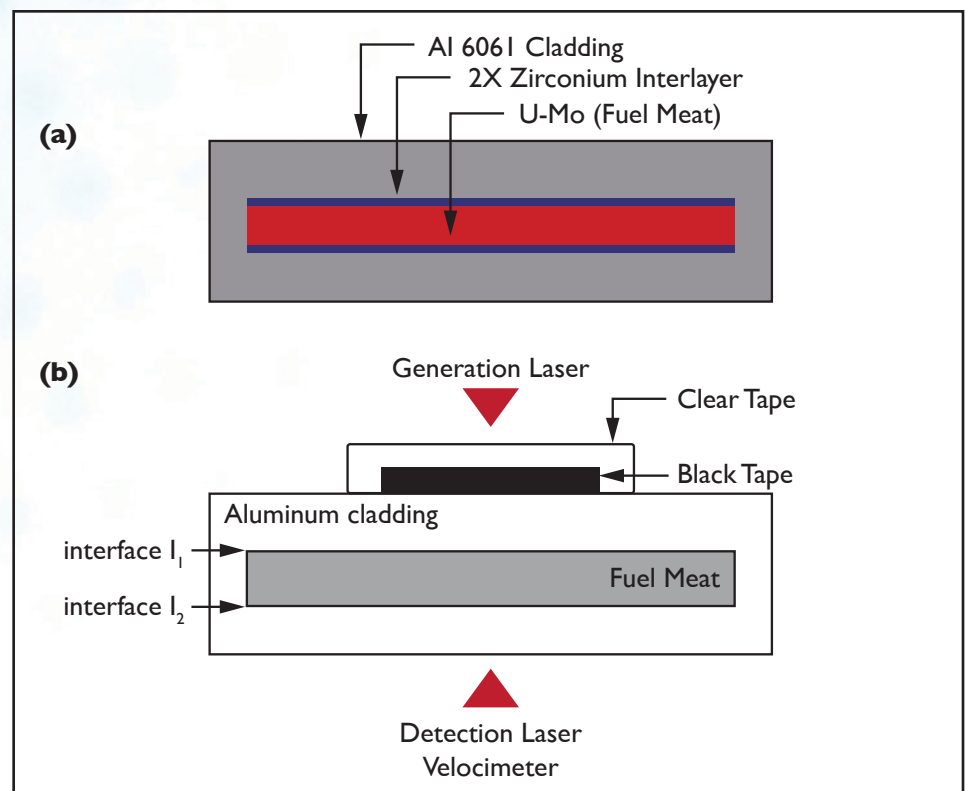


**Figure 1.** Schematic showing the specimen (a) and the geometries for laser shock generation, plasma-constraining mechanism, and back surface velocity detection (b).

Monolithic LEU fuel has recently transitioned from the research phase to the development and qualification stages. One of the significant fuel performance requirements that must be addressed involves ensuring that the clad-clad and fuel-clad interface strengths within the fuel plates are sufficiently high to maintain integrity throughout irradiation. Measurement of bond strengths before and after irradiation will provide valuable information in this regard. Furthermore, quality assurance requirements in the manufacturing process demand that suitable inspection and testing techniques are available to evaluate interfacial bond strengths in as-fabricated fresh fuel plates. This report is concerned primarily with bond-strength characterization. Since past efforts to characterize bond strengths in monolithic fuel plates using conventional mechanical testing methods have been unsuccessful, the LST technique is being developed to provide needed capabilities.

LST has been used previously in the measurement of bond strength for thin coatings on a substrate [1-2]. For thin-coating measurements, a pulsed laser is used to generate a large-amplitude compression pulse, which travels through the specimen as a shock wave. After reaching the back side of the specimen, the shock wave is reflected from the free surface as a tensile pulse that can debond the coating. Current research addresses the characterization of adhesive bonding in thicker structures composed of carbon-epoxy composite [3].

Advantages offered by LST include the ability to provide a spatially localized measurement without contacting the specimen, and with a minimum of specimen preparation. Since there is no propagation of the induced debond outside of the test area, the specimen remains intact. Compared to conventional testing techniques (e.g., pull

testing, bend testing, or double cantilever beam methods), these are significant advantages for applications involving radioactive materials. For example, nuclear fuel plates can be characterized remotely, improving operator safety, and fuel remains contained within the cladding, avoiding the potential for spreading radioactive contamination.

It should be recognized that LST is a high strain rate interrogation technique, relying on the propagation of waves at the speed of sound in the material. The constitutive behavior of a material under shock-loading conditions is significantly different compared to that observed using quasi-static (i.e., low strain rate) testing methods. In particular, flow stresses in metals are significantly elevated and deformation mechanisms are different at such high strain rates; therefore, the critical stress necessary to create a debond (i.e., the bond strength) as measured by LST may be several times greater than the values measured by quasi-static (i.e., low strain rate) methods such as pull testing [4]. It's worth noting that neither the high strain rate nor quasi-static bond strength measurements can be considered to provide the "correct" answer; rather, the strengths measured are representative of the material response under the specific testing conditions used. Therefore, provided that the constituent materials and sample geometries remain fixed and the sources of error and variability in the measurements are established for the different methods, a consistent basis exists for comparison of results, and practical and meaningful correlations may be established.

In this research effort, LST has been adapted to the characterization of interfaces in nuclear fuel plates fabricated by HIP, roll bonding, and friction stir welding processes. Both clad-clad and fuel-clad interfaces have been characterized. The details of LST

equipment and test methodology for bond strength characterization will be discussed. Initial bond strength determinations show that LST is able to distinguish between weak and strong bonds resulting from the different manufacturing processes.

### Principles and Experimental Approach

---

The laser used to induce shock waves in the fuel plates was a Q-switched neodymium doped: yttrium aluminum garnet (Nd:YAG) laser, which generates optical pulses of about 10 ns with a maximum energy of 3.5 J at a 1,064-nm wavelength. The laser beam is focused to a beam diameter near 5 mm. To avoid surface damage and to increase the efficiency of optical-to-mechanical transduction [2, 3], the surface of the material is covered with an absorbing tape and then covered with a transparent constraining medium (such as tape), as shown in Figure 1b. The shock waves generated under the confinement layer produce large-amplitude atomic displacement rather than laser ablation of the sample surface.

Previous work [2-6] used a liquid constraining medium (such as de-ionized water). The liquid constraining medium works well, but the liquid overspray can contaminate equipment and optics, and may not be desirable in the hot cell environment; therefore, recent work has focused on the use of transparent tape.

The shock-wave source size (roughly the laser spot size) needs to be about two times the sample thickness (about 1.5 mm) to the approximate one-dimensional (1-D) wave propagation. Under the 1-D approximation, shear stresses are neglected and the shock wave is primarily planar and compressive. The generated shock wave is then reflected by the back surface of the plate and con-

verted to a tensile wave; tensile stresses are responsible for debonding at the interface.

The resulting stresses developed in the material may be the result of several shock waves besides the wave reflected from the back surface. Previous results [5, 6] discussed a strategy to account for multiple reflections from interfaces within the specimen. In this paper, the simplifying assumption is made that the shock-wave energy reaching the backside is fully reflected and is the sole cause of the tensile stress at specimen interfaces. This simplifies the discussion and the resulting approximate stresses are adequate to illustrate LST. Bond strength is determined by increasing the laser pulse energy step by step. The ultimate stress value is imposed at the interface when debonding is imminent. To limit the cumulative effects of plastic deformation in the material, a single shock is applied at each shock location. Because shock waves are reflected from each surface or interface, the reflected shock wave propagates in material that has been subject to prior plastic deformation. Thus, plastic effects can occur during a single shock event.

Because of the intractable nature of a laser-generated shock wave from a confined plasma, optical energy of the source laser is not an accurate predictor of shock-wave stress. The back surface velocity is a more accurate representation of the stress imparted to the specimen. The stress estimate based on the back surface velocity is reasonable as a first approximation. More detailed stress estimates may be obtained, either by accounting for internal reflections from the different layers within the fuel plate in Equation (1) or by numerical simulation of the shock wave propagation. These approaches are the subjects of future investigation.

The stress is indirectly calculated from the measured back wall surface velocity, which is recorded by an optical velocimeter, based on a solid Fabry-Perot etalon (see Figure 1b). The velocimeter laser is a long pulse ( $>120 \mu\text{s}$ ) Nd:YAG, operated at a 1,064-nm wavelength. Details of the etalon interferometer have been described elsewhere [7].

For the simplified case where multiple wave reflections are not considered, the measured bottom surface velocity is assumed to provide a direct, first-order estimate of the magnitude of the reflected stress wave responsible for creating internal interface debonds. By ignoring multiple and overlapping reflections and assuming elastic, 1-D wave propagation and no attenuation, the measured bottom surface velocity,  $u_B$ , is related to stress at the bottom surface,  $\sigma_B$ , by the simplified relation given by Equation 1:

$$\sigma_B = \rho v u_B \quad (1)$$

where  $v$  is the speed of sound in 6061 Al (measured experimentally to be 6,440 m/s) and  $\rho$  is the density of 6061 Al (2.7 g/cm<sup>3</sup>).

Laser ultrasonic imaging of the specimen prior to and after the laser shock are used to confirm the presence of debonds, as well as to determine the depth of the debond (i.e., to determine at which internal interface the failure occurred) [3]. These ultrasonic inspections are performed using another laser-based experimental technique, where generation and detection laser beams are on the same surface (pulse-echo mode), superimposed with diameter sizes of about 1 mm and 0.5 mm, respectively. The step size of the scan is approximately 0.5 mm in the x and y directions on the sample surface. The generation laser was Nd:YAG, operated at 532-nm wavelength with a full width

at half maximum of 10 ns. The detection uses a long-pulse ( $>120 \mu\text{s}$ ) Nd:YAG laser, operated at a 1,064-nm wavelength and a photorefractive interferometer. The laser ultrasonic inspection is performed without the tape or confinement and is similar to a conventional ultrasonic C-scan.

## Experiments and Results

LST has been performed on fuel plates fabricated by three different clad bonding techniques: HIP, roll-bonded, and friction stir welding. The first HIP example is used to introduce the technique and the data processing/display methods used to characterize the shock locations in the specimen. Data obtained from the three fuel plate types are used for comparative purposes.

LST performed on a HIP fuel plate containing a stainless steel surrogate fuel foil is shown in Figure 2a. This particular plate was made using Neolube as a parting agent (i.e., to keep the plate from bonding to the spacers in the HIP assembly), which was being investigated as an alternative to the Grafoil parting agent that is currently used today. The Neolube approach was abandoned because Neolube was thought to have contributed to weakening of interfacial bonds. Circular features on the fuel plate (Figure 2a) show locations of laser shock testing. Dark black locations indicate areas of debond.

Figure 2b shows ways in which the data are displayed to characterize the effects of the LST. The A-scans are the raw laser ultrasonic signals taken at a single location. The B-scan images are a water fall plot of A-scans taken along a line. C-scan images are the maximum value from each A-scan generated while the specimen is being scanned and imaged. The A-scans emphasize individual reflections and pulse shapes.

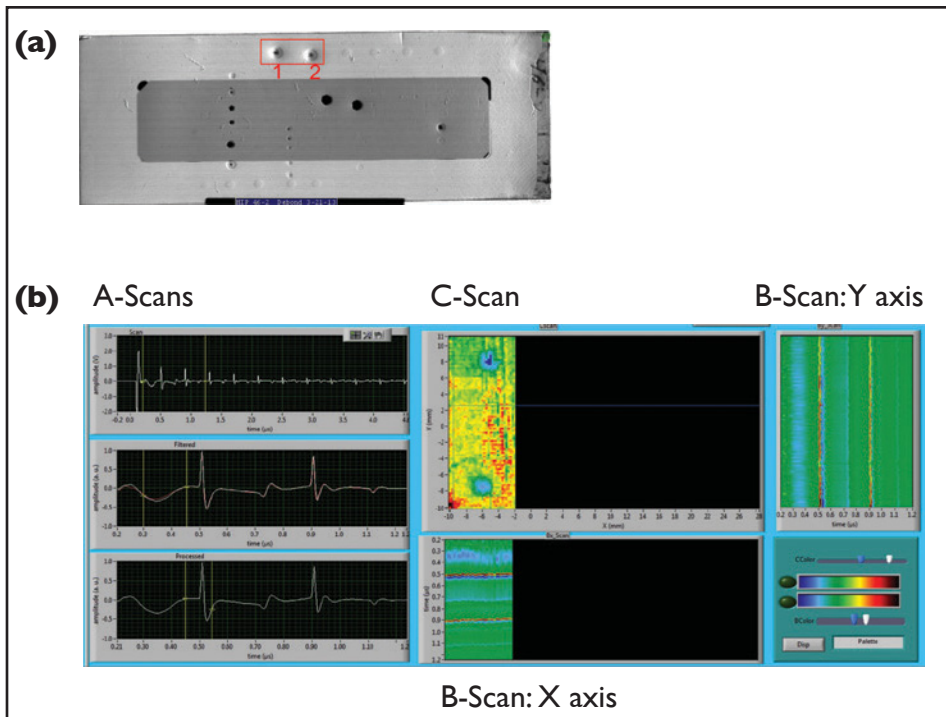


**Figure 2.** The laser shock locations being characterized are shown in the conventional ultrasonic C-scan (a). The laser ultrasonic processing necessary to characterize the laser shock locations is displayed (b). Signals at cursor location show good bonding and thinning of plate near the edge of the cladding (B-scan: X axis image).

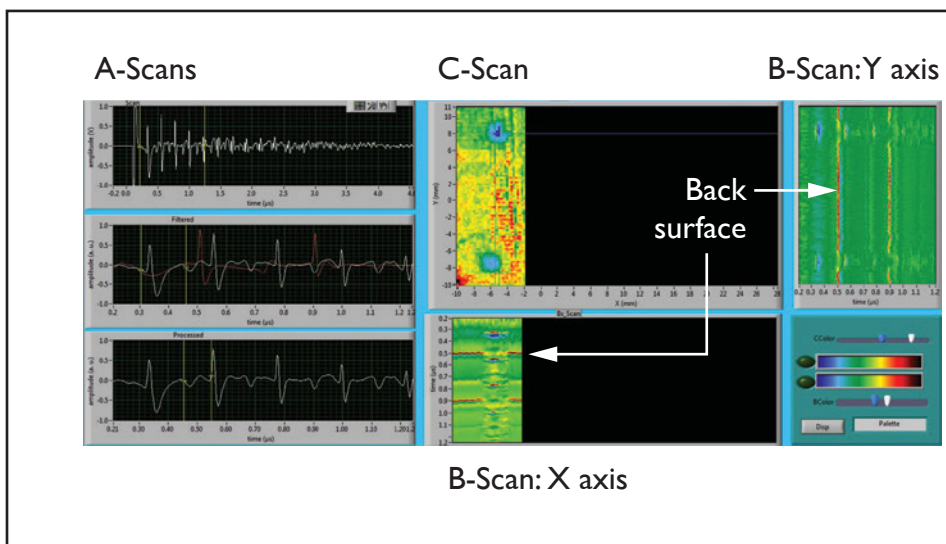


**Figure 3.** The three types of ultrasonic scans that are displayed show damage at laser-shock Location 1. The damaged interface adds a reflected return signal closer to the surface and keeps the back surface from receiving ultrasonic energy, hence the break in the back-surface echo line.

B-scans emphasize relative timing and magnitude of the ultrasonic reflections. C-scans emphasize geometry and relative magnitude of return signals.

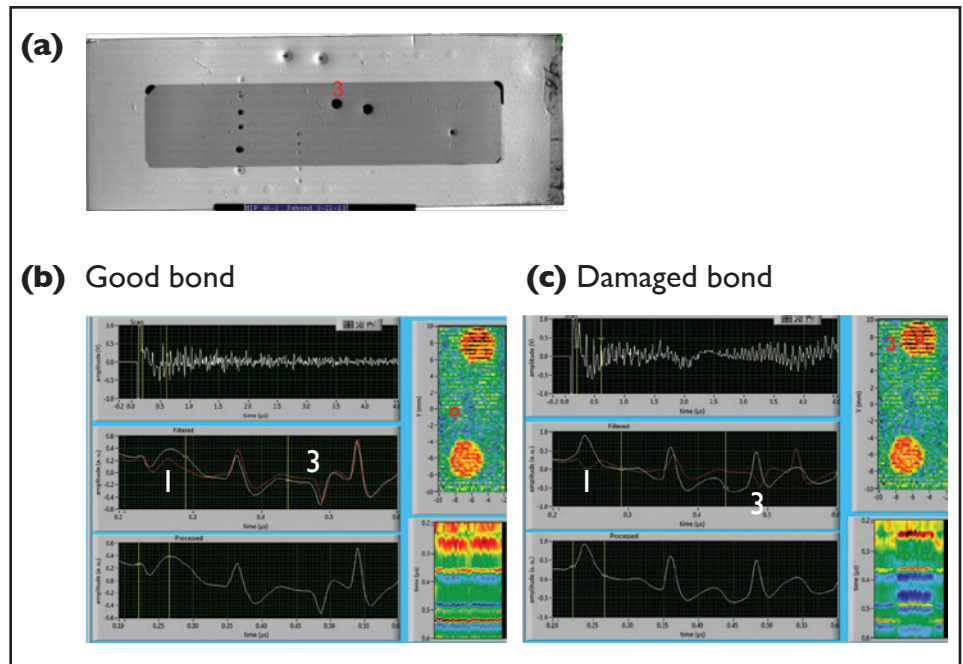
The blue cursor shown in the C-scan image of Figure 2b rests on a well-bonded region in a clad-only area. The B-scan images show contiguous lines formed from multiple back-wall reflections. The slope in the lines indicates that the plate thickness is decreasing as the edge of the plate is approached. The A-scans show the repetitive pattern of multiple back-wall reflections. C-scans identify the laser-shock locations and define the affected areas. The images in Figure 2b provide the baselines for comparison.

Figure 3 shows the resulting signals when there is a debond in the clad-clad interface. The regularity and order of the reflections in the A-scans are missing. The red signal in the middle A-scan is a baseline A-scan taken in a well-bonded region. The B-scans also show additional interface reflections from debonds that are distinctly different from the well-bonded areas.

Figure 4 shows the resulting signals when there is a well-bonded fuel-clad interface (a) and a debonded fuel-clad interface (b). In all cases, the fuel-clad interface complicated the resulting images. The debonded images show even more disorder. The A-scans show a signal inversion from the fuel-clad debond in the debonded images (Figure 4b). The first and third reflections show an amplitude inversion in the return signals when compared to the red baseline signal.

A roll-bonded dispersion fuel plate specimen has been tested and the results are shown in Figure 5. A large blister can be seen in the traditional C-scan image. The presence of the blister indicates that the clad-clad bonding may be weak. LST suggests that bonding improves in the section of the plate away from the blister because the laser-shock location (A) did not debond.

The results from testing a HIP fuel plate with a DU-10Mo fuel foil is shown in Figure 6. The images show that Location 8 is close to the debonding threshold. Damage at Location 8 can be identified in the B-scan, but the signature is not similar to a classic debond signature, as shown in Figure 4b. It is assumed that incipient debonding has occurred in laser-shock Location 8.



**Figure 4.** Laser C-scan data that show the signal over a well-bonded region (b) and over a damaged location from laser shock (c). In the expanded A-scan graph (middle image) for the damage location (c), the first and third arrivals are inverted. The red signal is the baseline from a well-bonded region. Signal inversion is clear evidence of debonding and reflection from a free surface.

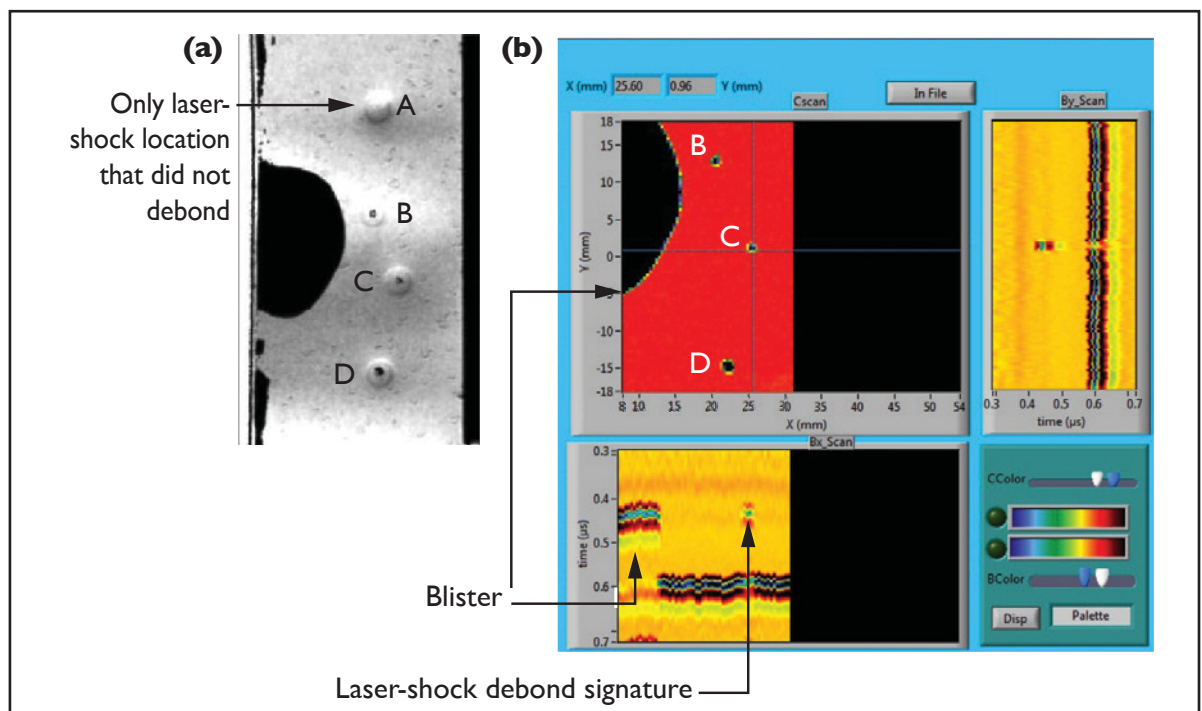


**Figure 5.** This roll bond process created a weak clad-clad interface as shown by the blister in the ultrasonic C-scan image (a). Laser ultrasound images indicate the presence of debonds at the laser-shock locations. The cladding interface strength appears to grow stronger above the blister because the interface at shock Location A remained intact.

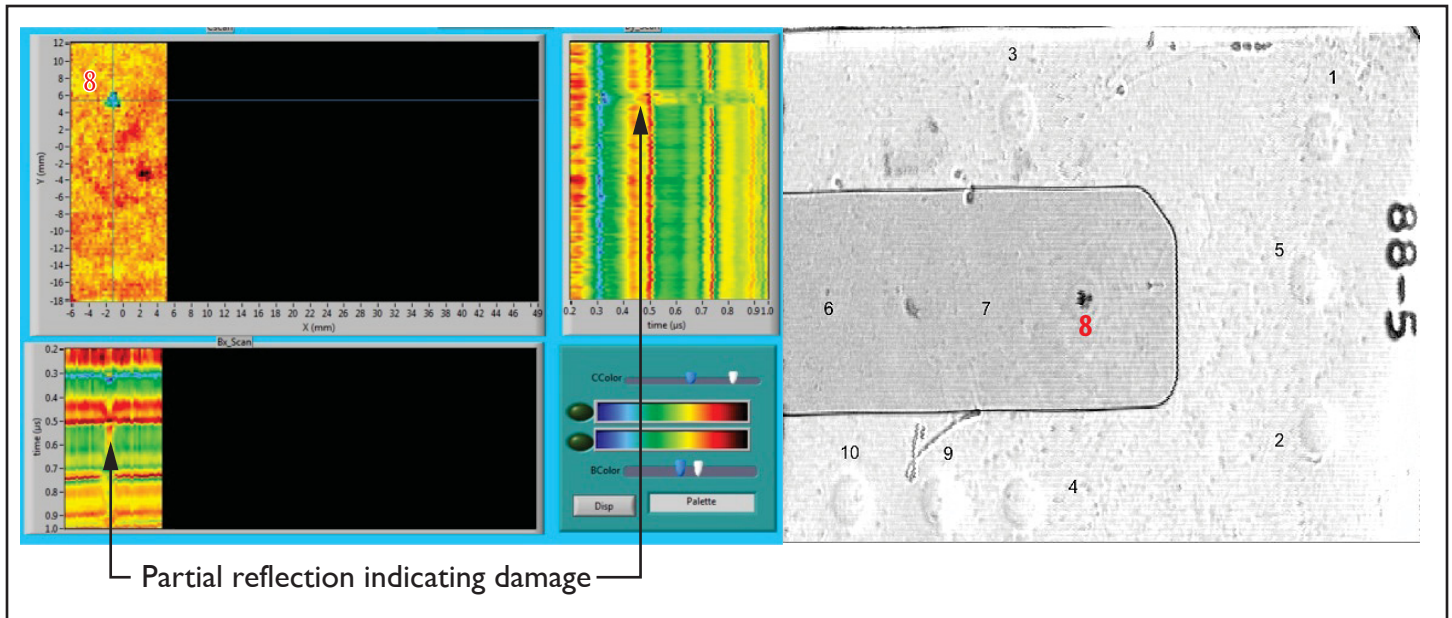


**Figure 6.** The results for fuel-cladding interface in a fresh fuel plate with a Du-10Mo foil is shown. B-scan imaging shows the beginning of damage (i.e., incipient debond) at laser-shock Location 8.

Friction stir-welded plates have also been tested. The fuel cladding interface can be debonded just as in the HIP examples shown. However, the clad-clad interface could not be failed as in the case of the clad-clad bond on the HIP fuel plate containing the DU-10Mo foil.

## Discussion

LST has shown the ability to debond weak clad-clad and all fuel-clad interfaces. The weak clad-clad interfaces have been produced by flawed or inadequate manufacturing processes. For all manufacturing processes, the fuel-clad interface has been successfully debonded using the LST system. This is not surprising because the fuel-clad interfaces comprise dissimilar materials that result in brittle interaction layers and residual stresses and may, therefore, be expected to exhibit lower strength than the clad-clad interface. At present, the LST system has not been able to debond a well-formed clad-clad interface. In such cases, it

is only possible to conclude that the interface strength is greater than the maximum stress value imposed during the test. The constraining technique used in the present study is adequate for fuel-clad characterization; however, a more efficient constraining mechanism may need to be developed for future clad-clad testing if it is to be used beyond a go vs. no-go type of test.

Table 1 is a summary of the interface strength characterization for clad-clad and fuel-clad interfaces in several fuel plates made by the different manufacturing processes investigated. Even though the constraining mechanism and maximum laser power are nominally identical for the different fuel plates, the maximum achievable stress at the back surface varies significantly. This behavior is consistent with observations made during testing on homogeneous 6061 aluminum alloy samples having various temper (Table 2), where it was observed that, for identical laser shock conditions, the softest temper (6061-O) produces a higher back

surface stress than hardened alloy (6061-T6). Thus, the magnitude of the stress induced by the LST will be material dependent.

The stainless steel clad interface in the HIP plate has interface strength more than two times the strength in the HIP plates with uranium fuel. The clad-clad interfaces in the stainless steel HIP and roll-bonded plates have a debonding threshold exceeding the maximum stress obtainable using the current constraining medium.

LST does cause significant plastic deformation in the aluminum alloy, which results in work hardening. The plastic deformation has similar effects on the wave propagation characteristics as tempering, as shown in Table 2. The LST converts an as-received 6061-O specimen into material that has post-shock elastic properties similar to 6061-T6.

**Table 1.** Debonding threshold measurements for clad-clad and fuel-clad interfaces in various fuel plates made by different manufacturing processes.

Specimen	Clad-clad threshold (MPa)	Fuel-clad threshold (MPa)
HIP plate with stainless steel foil using Neolube parting agent	1,850	1,400
Roll-bonded dispersion plate	1,500–1,600	no fuel-clad interface
HIP DU-10Mo fuel foil	>1,600	548
HIP LEU-10Mo fuel foil	>2,000	626
Friction stir welded cladding	>1,630	NA, no fuel

**Table 2.** Residual plastic deformation caused by the LST in 6061-0 results the treated locations having similar ultrasonic properties as 6061-T6.

6061-0 as received:	6061-0 after laser shock:
<ul style="list-style-type: none"> <li>• Sample 1 (unknown)               <ul style="list-style-type: none"> <li>- Thickness 1.574 mm</li> <li>- Speed 6.448971 m/s</li> <li>- STD 0.002798 m/s</li> </ul> </li> <li>• Sample 2 (spot 2)               <ul style="list-style-type: none"> <li>- Thickness 1.5507 mm</li> <li>- Speed 6.442015 m/s</li> <li>- STD 0.003011 m/s</li> </ul> </li> </ul>	<ul style="list-style-type: none"> <li>• 6061-0-1 (spot 1)               <ul style="list-style-type: none"> <li>- Thickness 1.5653 mm</li> <li>- Speed 6.407069 m/s</li> <li>- STD 0.003098 m/s</li> </ul> </li> </ul>
	6061-T6 as received:
	<ul style="list-style-type: none"> <li>• 6061-T6 (unknown)               <ul style="list-style-type: none"> <li>- Thickness 2.245 mm</li> <li>- Speed 6.38419 m/s</li> <li>- STD 0.004385 m/s</li> </ul> </li> </ul>

## Conclusion

The successful development of LEU monolithic fuel for research reactors requires a technique to characterize the strength of clad-clad and fuel-clad interfaces in both fresh and irradiated fuel plates. LST is currently being developed for this purpose. Currently, scoping studies are being performed to look at a variety of clad-clad and fuel-clad interfaces in fuel plates made using HIP, roll-bonded and friction stir welding bonding processes. Test procedures and data analysis methodologies are being developed to measure bond strength. During procedure development and analysis refinement, researchers will also gain a better fundamental understanding of LST effects on various materials and interfaces. A first order estimate of bond strength can be determined by measuring

back surface velocity corresponding to the debond threshold. LST data reported here show that interface strength can be successfully measured for fuel-clad interfaces. Measurement of bond strength for clad-clad interfaces will require the development of a more efficient constraining mechanism to generate larger stresses within the material. However, LST has shown the ability to detect weak clad-clad interfaces.

*Article previously published in the "40th Quantitative Nondestructive Evaluation (QNDE) & 10th International Conference on Barkhausen Noise & Micromagnetic Testing (ICBM) Conference," Denver, CO, July 21-26, 2013.*

## References

1. J.L. Vossen, *ASTMM Spec. Tech. Publ.*, 640, 122-131 (1978).
2. J. Yuan, V. Gupta, and A. Pronin, *J. Appl. Phys.* 74, 2405-2410 (1993).
3. M. Perton, A. Blouin, and J.-P. Monchalin, *J. Phys. D: Appl. Phys.*, 44 (2011).
4. M. Arrigoni, S. Barradas, M. Braccini, M. Dupeux, M. Jeandin, M. Boustie, C. Bolis, and L. Berthe, "Comparative study of three adhesion tests (EN 582 similar to ASTM C633 - LASAT (LASer Adhesion Test) - Bulge and blister test) performed on plasma sprayed copper deposited on aluminium 2017 substrates," *Journal of Adhesion Science Technology*, 20 (5), 471–487 (2006).
5. J.A. Smith, D.L. Cottle, and B.H. Rabin, "Laser Shockwave For Characterizing Diffusion Bonded Interfaces," to be published in *AIP Conf. Proc. Vol. 151*, D. O. Thompson, D.E. Chimenti, Editors, American Institute of Physics, Melville, NY, 2014.
6. J.A. Smith, B.H. Rabin, M. Perton, D. Lévesque, J.-P. Monchalin, and M. Lord, "Laser Shockwave Technique For Characterization Of Nuclear Fuel Plate Interfaces," *RERTR 2012 — 34th International Meeting On Reduced Enrichment For Research And Test Reactors*, Warsaw Marriott Hotel Warsaw, Poland, October 14-17, 2012.
7. M. Arrigoni, J.-P. Monchalin, A. Blouin, S.E. Kruger, and M. Lord, *Meas. Sci. Technol.* 20, 015302 (7pp) (2009).



**James A. Smith** (B.S., Engineering Science, Iowa State University, M.S. and Ph.D., Engineering, Texas A&M) is a Materials Characterization and Processes Systems Engineer at the Department of Energy's INL. He has worked at AT&T Bell Laboratories, Corning Incorporated, and the Mayo Clinic prior to joining INL. Jim is an innovative and goal oriented systems engineer/project manager with over 20 years of diverse experience, solving complex and ambiguous opportunities from first principles. He is diligent in envisioning new possibilities and developing visionary strategies that progress toward a shared vision. He is known for quickly turning system concepts into plant prototypes by developing close collaborations and understanding customer needs. He specializes in developing products and processes through pioneering measurements and data analysis techniques.



**David Cottle** (1988, Laser-Electro-Optics, Idaho State University, NDE Ultrasonics Testing Level 2 specializing in immersion ultrasonic testing) has over 20 years of experience with lasers, laser acoustics, pulsed laser acoustic generation, interferometer detection, immersion ultrasonic testing inspection, laser-based thermal diffusivity measurements, and many other material characterization techniques.



**Barry H. Rabin** (B.S., 1982, Metallurgical Engineering, Michigan Technological University; Ph.D., 1986, Materials Engineering, Rensselaer Polytechnic Institute) has over 25 years of research and development leadership experience working with a diverse range of advanced materials and manufacturing technologies. In addition to his career at INL, he has started several companies and worked in the private sector. He is currently serving as the technical lead for Material Properties on the Global Threat Reduction Initiative/U.S. High-Performance Research Reactors Fuel Development Program. Dr. Rabin has 14 issued patents and over 100 technical publications to his credit.



# **Multiscale Development of Materials Models for Fuel Performance Simulation**

# Multiscale Development of Materials Models for Fuel Performance Simulation

*M.R. Tonks, S.B. Biner, Y. Zhang, R.L. Williamson, S.R. Novascone, B.W. Spencer, J.D. Hales, D.R. Gaston, C.J. Permann, D. Andrs, S.L. Hayes (INL), P.C. Millett (UofArk), D. Andersson, C.R. Stanek (LANL)*

Radiation-induced microstructure evolution in  $\text{UO}_2$ , including radiation swelling and fission gas release, drastically affects fuel performance and can eventually result in fuel failure. Traditional fuel performance codes consider these microstructure effects using empirical fits to experimental data. While these empirical models accurately predict material behavior within tested conditions, they cannot predict the behavior outside of those conditions. In order for a fuel performance code to be predictive in a range of operating conditions, it must consider atomistic and microstructure effects. Here, we present the multiscale methodology that is the basis of the MOOSE-BISON-MARMOT (MBM) suite of fuel performance codes under development at Idaho National Laboratory (INL). MOOSE, the Multiphysics Object-Oriented Simulation Environment, is the basis of the MARMOT fuel microstructure code and the BISON fuel performance code. Here, we show how atomistic simulations are used to develop quantitative models of the effect of radiation damage on microstructure in MARMOT. From these models, mechanistic material constitutive models are developed for use with BISON. This approach is demonstrated by developing a model of the impact of grain boundary (GB) fission gas bubbles on the effective GB thermal resistance.

## Introduction

Microstructure changes that occur within the fuel during reactor operation dominate its performance. Radiation damage at the atomic scale causes fission product forma-

tion and point defect generation. This leads to the formation of microstructural features such as fission gas bubbles and solid fission product precipitates. These microstructural changes drastically alter material properties such as thermal conductivity, yield stress, elastic constants, volumetric swelling, and more. These effects result in the decrease of reactor efficiency and eventually in fuel failure.

Fuel performance codes have been created to predict behavior of the fuel to improve reactor design and decrease fuel failures. These codes do not represent the effects of radiation-induced microstructure evolution explicitly, but rather rely on empirical fits to experimental data. Such codes have proven very valuable in the design and maintenance of our current fleet of light water reactors. However, new safety concerns and global energy requirements necessitate the design of new advanced reactors that go above and beyond current light water reactors. The design of new innovative reactors requires a more predictive fuel performance modeling capability, which would be difficult with the current fuel performance codes and empirical materials models.

In the U.S. Department of Energy Nuclear Energy Advanced Modeling and Simulation (NEAMS) Program, a suite of codes is being developed to provide a more predictive fuel performance modeling capability. These codes, under development at INL, take advantage of modern code architectures to model a range of fuel geometries and fuel types using lower-length, scale-informed materials models. These codes are called

the MOOSE-BISON-MARMOT codes, or MBM.

In this paper, we provide an overview of fuel performance model development that is being carried out at INL as part of the NEAMS Program. We also discuss our use of atomic-scale simulations conducted at Los Alamos National Laboratory to improve our materials models. We begin by summarizing the overall MBM effort. We then go into detail about the MOOSE, BISON, and MARMOT codes. Finally, we summarize our multiscale material model development and give an example.

## MOOSE-BISON-MARMOT Overview

The goals of our development efforts were threefold:

1. Take advantage of modern code architectures, numerical methods, and parallelization to develop an efficient code that is easy to develop and that can be run on desktop computers and massive supercomputers
2. Accurately represent a large range of fuel types and geometries, including the contact between the fuel and cladding (one-dimensional [1D], two-dimensional [2D], and three-dimensional [3D])
3. Use atomistic and microstructure modeling to develop physically based materials models that describe radiation-induced microstructure evolution.

Accomplishing all three of these goals required a hierarchical development approach involving three code projects.

The MOOSE framework is the basis of the simulation tools and provides the advanced numerical capabilities required by our first goal. The BISON fuel performance code was created using the MOOSE framework and accurately represents the macroscale fuel behavior, as stated in our second goal. The MARMOT mesoscale simulation code was also built using the MOOSE framework. MARMOT builds on atomistic simulation results to model the microstructure evolution within the fuel, providing data needed to develop the materials models required by our third goal.

### The MOOSE Framework

As stated above, MOOSE is an advanced numerical framework that is the basis of both the BISON and MARMOT codes. In more detail, it is a parallel computational framework for enabling the solution of complex, fully implicit multiphysics systems using the finite element method (FEM) [1]. It enables complex analysis tools to be built rapidly by scientists and engineers, while also allowing them to take advantage of current high-performance computing architectures and efficiently prepare for future supercomputer designs. It has been used to solve complex systems of equations from subjects ranging from chemical reactions and transport to computational fluid dynamics. MOOSE has been utilized in many nuclear applications, including nuclear fuel performance and optimization, pebble bed reactor design, neutronics, CRUD deposition, thermal hydraulics, hydride formation, and full reactor core analysis.

The user-facing interface to MOOSE uniquely combines recognized computer science techniques with a consistent underlying mathematical description to allow scientists and engineers to develop engineering simulation tools in a relatively short amount of time. To add new physics

to a MOOSE-based application, users write actual C++ code (typically only a few lines, employing very simple syntax), rather than having to learn a domain-specific language or a complex, templated, meta-programming system. MOOSE has simple interfaces for defining the governing partial differential equations (PDEs), boundary conditions, material properties, post-processors, etc. All MOOSE code can be used for 1D, 2D, and 3D simulations. In addition, MOOSE applications can be run on one processor or on thousands of processors, without requiring the user to write any code for parallel communication.

In addition to allowing for easy implementation of physics models, MOOSE has an extended library of existing physics that can be used in any MOOSE-based application. This library provides access to a large selection of physics without the user having to write any additional code.

In addition to the BISON and MARMOT codes discussed below, many other applications have been created using MOOSE. For example, PRONGHORN [2] is a neutron diffusion code coupled to porous flow to model pebble bed reactors; RAT [3] models chemical reactive transport in porous media; and the code FALCON [4] simulates geomechanical systems fully coupled to underground water flow.

### The BISON Fuel Performance Code

BISON is the NEAMS flagship fuel performance code and has been under development at INL since 2008. As mentioned above, BISON is built on the MOOSE framework and has been built to model 2D-axisymmetric and 3D nuclear fuel performance problems [5]. Currently, it is being used to model light water reactor fuel, TRISO fuel, metal annular fuel, and metal plate fuel.

The BISON governing equations consist of fully coupled PDEs for energy, species, and momentum conservation. The energy balance equation is given in terms of the heat conduction equation

$$\rho C_p \frac{\partial T}{\partial t} + \nabla \cdot \mathbf{q} - E_f \dot{F} = 0, \quad (1)$$

where  $T$ ,  $\rho$ , and  $C_p$  are the temperature, density and specific heat, respectively, and  $E_f$  is the energy released in a single fission event from the volumetric fission rate. The heat flux is given as

$$\mathbf{q} = -k \nabla T \quad (2)$$

where  $k$  is the thermal conductivity.

Species conservation is given by

$$\frac{\partial C}{\partial t} + \nabla \cdot (-D \nabla C) + \lambda C - S = 0 \quad (3)$$

where  $C$ ,  $\lambda$ , and  $S$  are the concentration, radioactive decay constant, and the source rate of a given species, respectively. Additional terms can be added to capture migration of a species in a temperature gradient.

Momentum conservation is prescribed assuming static equilibrium at each time increment using Cauchy's equation

$$\nabla \cdot \boldsymbol{\sigma} + \rho \mathbf{f} = 0 \quad (4)$$

where  $\boldsymbol{\sigma}$  is the Cauchy stress tensor and  $\mathbf{f}$  is the body force per unit mass. The displacement vector  $\mathbf{u}$ , which is the primary solution variable, is connected to the stress field with the strain through kinematic and constitutive relations.

As mentioned previously, the constitutive and material behavior in the fuel is typically represented with empirical or semi-empirical relations that have been obtained by

fitting to experimental data. These models accurately represent the material behavior in typical reactor conditions, but they are not accurate for new fuel types or in accident conditions. Many of these empirical models have been implemented in BISON; see [5] for a detailed description of these materials models. Using these models, various experimental validations have been carried out, with good results.

To demonstrate the capabilities of BISON, we show a 3D BISON result taken from [6]. Manufacturing defects known as missing pellet surfaces (MPS) in fuel pellets cause conditions that can potentially lead to cladding failure. To demonstrate the 3D capabilities of BISON, we show results from two simulations of a five-pellet fuel rodlet with a MPS on the center pellet. In the first simulation, the defect is 0.25-mm deep and in the second it is 0.5-mm deep. The simulations predicted the behavior of the rod for 2.5 years in typical pressurized water reactor conditions with a zircaloy-4 cladding. The simulations were run using 160 processors and took 11 hours to complete.

The distance between the pellet and the clad is much greater adjacent to the MPS defect than for undamaged pellets. This causes a dramatic decrease in the conductance across the gap and a corresponding decrease in heat transfer between the pellet and clad adjacent to the defect. Therefore, the temperature is elevated in the fuel near the surface with the defect, as seen in Figure 1(a). Because of the higher fuel temperature, the cladding temperature is elevated around the boundaries of the defect, where the gap conductance is unaffected by the defect, as shown in Figure 1(b), which shows just the clad, with displacements magnified 15 times. Immediately adjacent to the defect, the cladding temperature is significantly decreased because of the lower gap conductance.

### MARMOT Mesoscale Modeling Code

Though radiation damage begins at the atomistic scale, with collision cascades and fissioning atoms, the impact of radiation on material behavior results from changes in the microstructure. The microstructure domain is commonly called the mesoscale and falls between hundreds of nanometers and hundreds of microns.

During its lifetime in the reactor, fission events and collision cascades are constantly forming point defects and fission products within the  $\text{UO}_2$  fuel. These defects migrate and eventually cluster, forming voids, interstitial loops, and bubbles. Small bubbles form within the grains, but much larger bubbles form on the grain boundaries (GBs). Gradients in stress and temperature also have large effects on this evolution. This damage degrades the thermal conductivity and leads

to swelling. In addition, the GB bubbles eventually interconnect and form pathways to free surfaces so the gas can enter the gap between the fuel and clad.

The MARMOT code is focused on simulations of this microstructure evolution at the mesoscale. To capture all necessary physics, three main types of equations are solved: phase field, solid mechanics, and heat conduction. Each of these defining PDEs is solved using FEM with the MOOSE framework [7].

In the phase field model, microstructural features are represented with continuous variables that are evolved with a system of PDEs. Conserved variables that represent things like vacancy or gas atom concentrations are evolved with a Cahn-Hilliard equation

$$\frac{\partial c_i}{\partial t} = \nabla \cdot M_i \nabla \frac{\partial F}{\partial c_i} \quad (5)$$

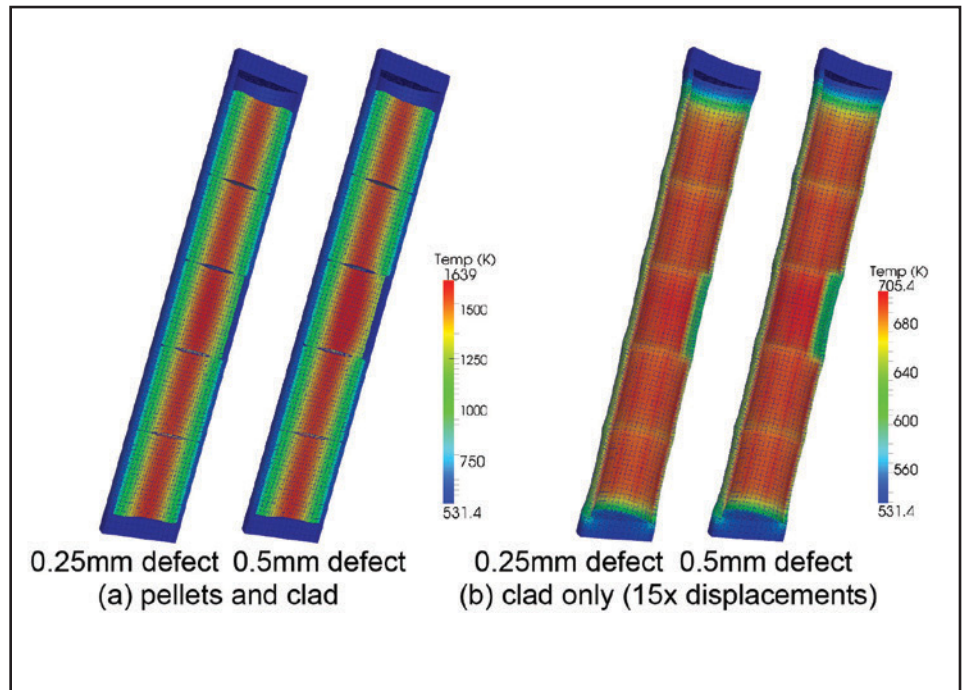


Figure 1. Temperature at end-of-power ramp in 3D MPS BISON simulations (taken from [6]).

where  $c_i$  is the conserved variable,  $M_i$  is the mobility, and  $F$  is the free energy functional that represent the Gibbs free energy as a function of the various variables. Non-conserved variables, representing things like grains or phases, are evolved with an Allen-Cahn equation

$$\frac{\partial \eta_i}{\partial t} = -L_i \frac{\partial F}{\partial \eta_i} \quad (6)$$

where  $\eta_i$  is the nonconserved variable and  $L_i$  is the mobility. For more information about the free energy functional and the solution of these equations with FEM, see [7]. The phase field method has been used to model a large range of microstructure evolution [8], including radiation damage [9].

The mesoscale mechanics of the fuel are modeled with Equation (4), where the constitutive model is treated as linear elastic, but with an anisotropic single crystal elasticity tensor. The elasticity tensor is a function of the grain orientation and the presence of voids or bubbles. Lattice strains from defects and pressure within the bubbles are represented with a stress-free Eigenstrain. Heat conduction is described with Equation (1), but the thermal conductivity varies spatially as a function of the phase field variables describing the microstructure.

Though MARMOT is a mesoscale code, it relies heavily on information obtained with atomistic calculations. First, many of the mechanisms with which the microstructure evolves are not well known, especially under irradiation. Therefore, atomistic calculations, both with density functional theory and molecular dynamics (MD), are used to explore the critical mechanisms, which are then incorporated into the phase field models. In addition, atomistic calculations are used to determine critical parameter values that are needed for the simulations that are not available experimentally. Once

the required parameters are obtained, MARMOT can model a large range of materials, including both fuel and cladding.

We demonstrate the capabilities of MARMOT with a simulation taken from [7] investigating the impact of void formation on the bulk thermal conductivity. In this simulation, a cube of  $\text{UO}_2$  is irradiated, resulting in the formation of gas bubbles. The bubble nucleation was modeled with a single conserved variable describing the concentration of vacancies within the material. A random source term was used to represent vacancies created by a collision cascade. In addition to the phase field variables, a heat conduction simulation was coupled to probe

how effectively the evolving microstructure conducted heat. From this, the effective thermal conductivity was computed.

Figure 2(a) shows the final void structure, along with temperature isosurfaces, showing the effect of the voids on the temperature profile in the material. After an initial nucleation period, voids begin to form, resulting in a rapid increase in porosity (see Figure 2(b)). Once the nucleation of the voids is complete, the rate of increase of the porosity decreases slightly as the voids continue to grow. The effective thermal conductivity of the material slowly drops as the vacancy concentration increases in the

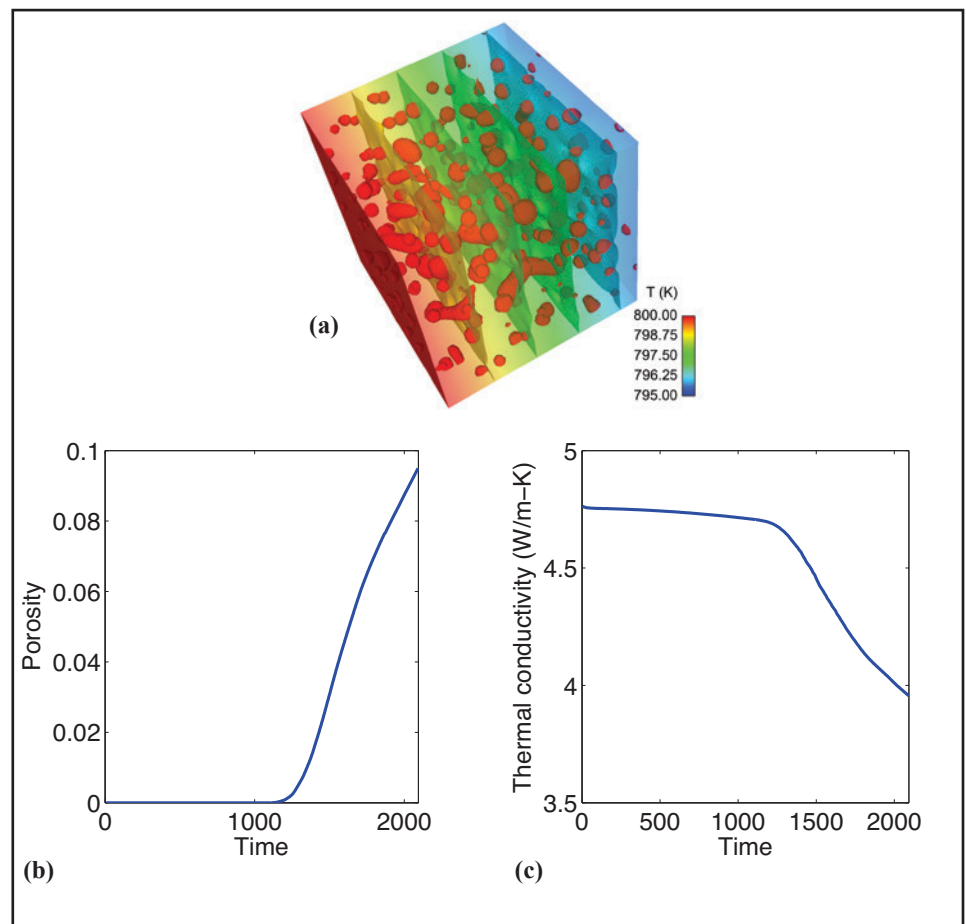


**Figure 2.** Simulation results showing the effect of void formation on thermal conductivity. The final void structure with temperature isosurfaces is shown in (a). The porosity is shown with time in (b) and the change in the effective thermal conductivity is shown in (c) (taken from [7]).

material (Figure 2(c)). However, once voids begin to form, the thermal conductivity begins to drop much faster. Once the voids stop nucleating and only grow, the drop in thermal conductivity slows.

## Multiscale Material Model Development

To create a predictive fuel performance code requires materials models that are not completely tethered to the existing sets of experimental data. We need models that are still accurate in accident conditions, where tests have not been conducted, and for new conditions and fuel types. In our multiscale approach, MARMOT simulation results compliment experimental data in the development of materials models. When possible, mechanistic materials models are developed that only use data for calibration and validation. However, when a mechanistic model is not possible, fits to simulation data still provide more flexibility than fits to experimental data.

For this approach to be accurate, the MARMOT models must be well validated against experimental data. This effort is just beginning, primarily because of the difficulty of obtaining data at the length and time scales used in MARMOT. However, significant strides have been made in post-irradiation examination and in development of separate effects tests that look at individual aspects of the microstructure evolution.

We demonstrate our multiscale model approach here by developing a model of the impact of fission gas bubbles on the effective thermal resistance of GBs within the fuel (taken from [10]). A similar multiscale approach could be applied to investigate thermal conductivity in the cladding, but is saved for future work. The fission gas release model used in the BISON code (from [11]) evolves the density of fission bubbles in the bulk of the material, as well as the bubbles on GBs. While both types of bubbles directly impact the thermal conductivity of the fuel, the empirical model for thermal conductivity in the fuel [12] does not couple the fission gas model to the thermal conductivity model. Here, we developed a coupled model of the impact of fission gas bubbles on the fuel thermal conductivity.

A model has been developed that computes the impact of both inter- and intragranular gas bubbles on thermal conductivity [13]. The model takes the form of multipliers that combine with the model from [12], (i.e.,  $k = \kappa_{in} \kappa_{GB} k_{UO_2}$ ), where the impact of intragranular gas bubbles  $\kappa_{in}$  is determined with the traditional Maxwell-Eucken formula [14]:

$$\kappa_{in} = \frac{1 - p}{1 + (\sigma - 1)p} \quad (8)$$

where  $p$  is the porosity and  $\sigma$  is a multiplier that considers the shape of the bubbles.

However, for the intergranular gas bubbles, we use an equation that considers the impact of the GB thermal resistance:

$$\kappa_{GB} = \frac{1}{1 + k_{UO_2} R'_k (X_{GB}^c)/d} \quad (9)$$

where  $d$  is the grain size and  $R'_k$  is the effective GB thermal resistance, which considers the impact of fission gas bubbles on the GB using the percentage of the GB covered by fission gas, or the grain boundary coverage  $X_{GB}^c$ .

In [13], the model of the effective GB thermal resistance, as a function of the grain boundary coverage, is an empirical fit to data from mesoscale calculations of bicrystals. Here, we use multiscale modeling to develop a mechanistic expression for the effective grain boundary resistance that is specific to  $UO_2$ .

### a. Atomistic simulations

The first step to developing a model particular to  $UO_2$  is to find the GB thermal resistance of clean GBs in  $UO_2$ . This information has never been obtained experimentally, thus we rely on atomistic simulations. MD calculations on four types of GBs were conducted using the Basak potential [15] at three different temperatures. The results are found in Table 1.

<b>Table 1. GB Thermal Resistance in <math>UO_2</math> from [10].</b>			
GB Type	Rk ( $\times 10^{-9}$ m <sup>2</sup> K/W)		
	300 K	800 K	1500 K
$\Sigma 5$ sym. tilt	1.69	1.14	0.92
$\Sigma 5$ tr. tilt	1.08	0.83	0.60
$\Sigma 5$ tr. twist	1.38	0.86	0.63
Random	1.48	0.87	0.66

### b. Mesoscale MARMOT simulations

With the GB thermal resistance, we are ready to investigate how the presence of bubbles on the GB contributes to thermal resistance. If we consider a straight boundary with several bubbles, it is reasonable to consider the system as two thermal resistors in parallel, in which the combined thermal resistance is

$$\frac{1}{R'_k} = \frac{1}{A_{GB} + A_{bub}} \left( \frac{A_{GB}}{R_k^0} + \frac{A_{bub}}{R_{bub}} \right) \quad (10)$$

where  $A_{GB}$  and  $A_{bub}$  are the areas of the GB and bubble, respectively, and  $R_{bub}$  is the thermal resistance of the bubble. The resistance of the bubble can be calculated from  $R_{bub} = d_{bub}/k_{gas}$ , where  $d_{bub}$  is the diameter of the bubbles and  $k_{gas} = 0.00565$  W/(mK) [16] is the thermal conductivity of Xe gas at 300 K. If we assume the GB bubbles are rectangular (though in reality they are lenticular) their area can be determined from

$$A_{bub} = d_{bub} X_{GB}^c \quad (11)$$

per unit length of GB. The area of the GB can be determined from

$$A_{GB} = d_{GB}(1 - X_{GB}^c) \quad (12)$$

per unit length of GB. However, the value for the GB distance is difficult to determine, because for thermal resistance GBs are considered as an infinitely thin interface in contrast to our diffuse GB representation. Another concern is that while this model is clear for straight boundaries perpendicular to the heat flow, it is unclear how relevant it is for a polycrystals in which GBs can be at various angles.

To determine the value for  $d_{GB}$  and what changes may be necessary for polycrystals, we conduct a series of mesoscale heat conduction simulations using the MARMOT code. To determine the effective GB thermal resistance in each simulated microstructure, a mesoscale heat conducted simulation is carried out in which a fixed temperature  $T_f = 800$  K is applied to one boundary and a heat flux  $q_f = 5.0 \times 10^6$  W/m<sup>2</sup> to the opposite boundary. The local thermal conductivity varies spatially, where in the bulk  $k_{UO_2} = 4.75$  W/(mK) [17], in the bubble the thermal conductivity equals  $k_{gas}$ , and in the GB, values are used consistent with GB thermal resistances of  $R_k = 1.0 \times 10^{-9}$ ,  $5.0 \times 10^{-9}$  and  $1.0 \times 10^{-8}$ . With these conditions, the temperature throughout the domain is determined by solving the nonlinear system defined by the steady-state form of Equation 1, where

$$k_{eff} = \frac{q_f l}{T_f - \bar{T}_o} \quad (13)$$

where  $l$  is the side length in the direction of the flux. The effective thermal resistance of the microstructure  $R'_k$  is calculated from the effective thermal conductivity with

$$R'_k = d \left( \frac{1}{k_{eff}} - \frac{1}{k_{UO_2}} \right) \quad (14)$$

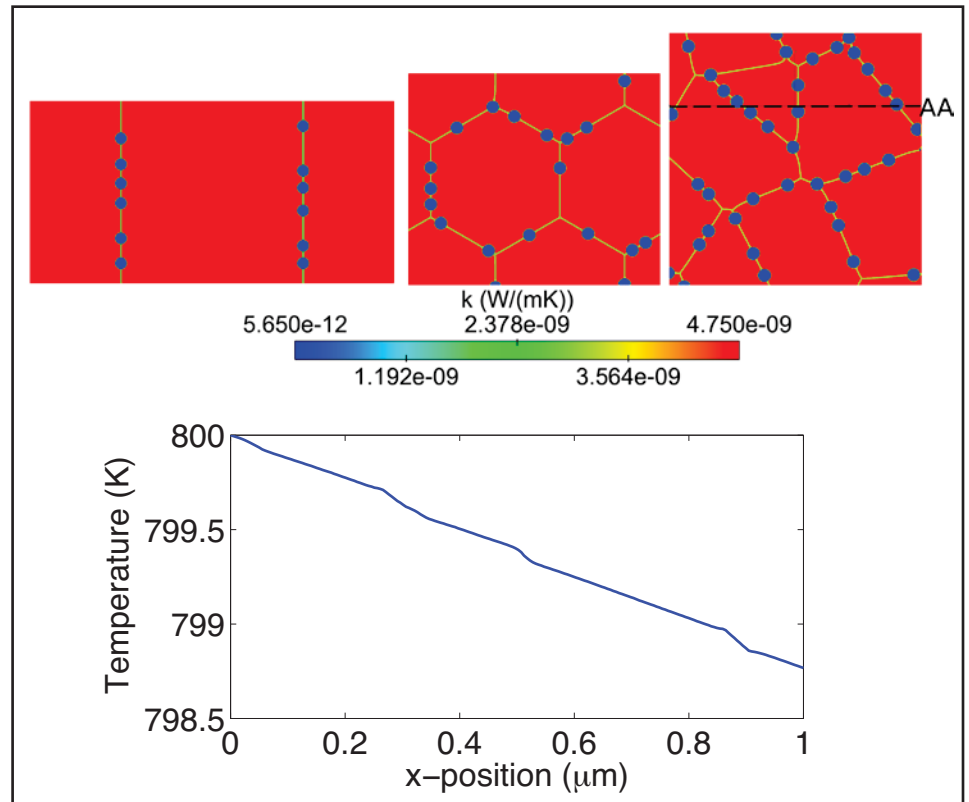


**Figure 3.** Mesoscale heat conduction simulations, where (a) shows examples of the simulation domains shaded by thermal conductivity, and (b) is a plot of the temperature vs.  $x$  position in the seven grain polycrystal along line AA (labeled in (a)). Figure taken from [10].

**Table 2.** Values for the GB distance  $d_{GB}$  determined by fitting to the mesoscale data. Note that the Kapitza length  $l_k$  is also shown, for reference, from [10].

$R_k$ ( $\times 10^{-9}$ m <sup>2</sup> K/W)	$l_k$ (nm)	$d_{GB}$ (nm)
1.0	4.85	4.0
5.0	24.49	15.0
10.0	50.84	25.0

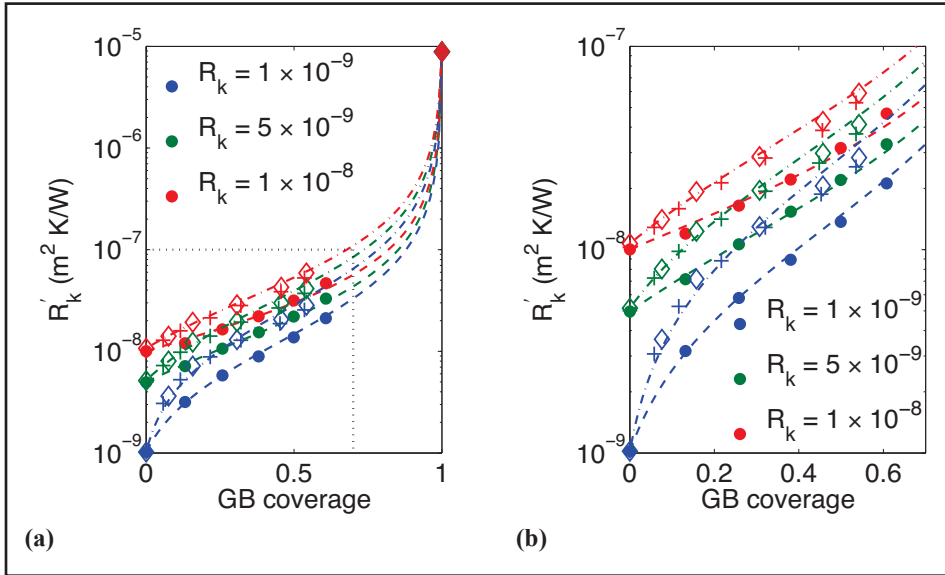


**Figure 4.** Model of the effect of GB coverage on the effective thermal resistance, where (b) is zoomed in on the section from (a) marked with dotted lines. In the plots, the dots show data from our bicrystal simulations: the plus signs from the four-grain hexagonal polycrystal and the diamonds from the seven-grain polycrystal. The lines show the values predicted by the model, where the dashed lines are for the bicrystal and the dot-dashed line are for the polycrystals. Taken from [10].

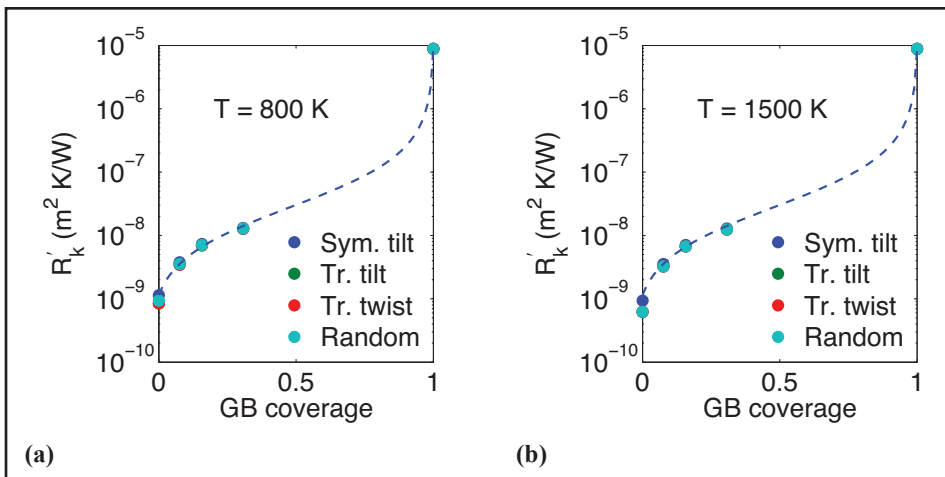


**Figure 5.** Model of the effect of GB coverage on the effective GB thermal resistance using the MD-determined values for the GB thermal resistance. Note that the GB type has little effect on the effective GB thermal resistance for both 800 and 1500 K. Figure taken from [10].

By fitting the value of  $d_{GB}$  for each set of bicrystal simulations, our model matched the mesoscale results accurately. The fitted values for  $d_{GB}$ , shown in Table 2, were close to the values for the Kapitza length,  $l_k = R_k k_{UO_2}$ , but not exact. We suspect this is because we are using a diffuse interface model to predict values for a model that assumes a sharp interface.

From our mesoscale simulations, we found that the two polycrystals behave similarly, but they had a higher thermal resistance than the bicrystal. This is because the bubble-laden GBs are often not parallel to the heat flow. To adjust our model for polycrystals, we double the value of the bubble area to account for the increased amount of bubbles in the system. With this correction, our model compares well to polycrystal mesoscale simulation results (see Figure 4).

We conducted additional seven-grain polycrystal simulations using the values for the GB thermal resistance calculated with MD simulation in the previous section to determine the corresponding values for  $d_{GB}$ . From the simulations, it is clear that the type of GB does not have a significant impact on the values of the effective GB thermal resistance, using the values for both  $T = 800$  K and 1500 K (Figure 5). Therefore, for our  $UO_2$  model, we used the values for the symmetric tilt boundary at 800 K, which gave a value of  $d_{GB} = 4.0$  nm.

### c. Macroscale BISON Simulations

With our mechanistic model developed with atomistically informed mesoscale simulations, we implemented the coupled fission gas/thermal conductivity model in BISON. Our simulations employed all of the materials models summarized in [5], with one change: we modified the fuel thermal conductivity model from [13] by replacing the multiplier for dissolved fission products with our fission gas thermal conductivity model. Note that our model did not capture all contributions to the reduction in thermal conductivity from dissolved fission products. Further additions in the model will be made in the future that will add in the missing contributions.

We then used the model in 10-pellet rodlet simulations with typical pressurized water reactor conditions to predict the behavior after two years in the reactor. The rodlet geometry is represented in 2D by taking advantage of axisymmetry, as shown in Figure 6. For each example shown in this section, we compared the simulation results to those from an identical simulation, except that the contribution of the fission gas to the thermal conductivity from our new model was set to zero. Thus, by comparing the two simulation results, we could easily observe the impact of our model on thermal conductivity. We conducted the simulations with four different average grain sizes, to see the impact of grain size on fuel behavior. Figures 6(a) through 6(c) show the change in GB coverage, intragranular porosity, and percent fission gas release, respectively, over time at the center of the fuel rodlet (point 1) for three grain radii. As grain radius decreased, GB coverage behavior (Figure 6(a)) was unchanged, showing that in the fission gas release model [11] the relative density of gas on the GB is unaffected by grain size. However, the total amount of gas on the GB did increase, because there was more GB area with a smaller grain size,

which resulted in a decrease in the intragranular porosity (Figure 6(b)) and an increase in the amount of gas that is released (Figure 6(c)).

Though GB coverage is insensitive to the grain size, the impact of GB coverage on thermal conductivity increases with decreasing grain radius (as shown in Figure 6(d)). The temperature difference due to our model also increases with decreasing grain radius

due to changes in the fuel thermal conductivity (Figure 6(e)). In order to illustrate the effect of the fission gas on multiple physics, we also plot the temperature (rather than the temperature difference) at point 1 (Figure 6(f)). There is an increase in temperature due to decreasing grain radius. However, only part of the increase is due to the decrease in the fuel thermal conductivity. A portion of the increase is caused by the increase in fission gas release (Figure 6(c)), which lowers

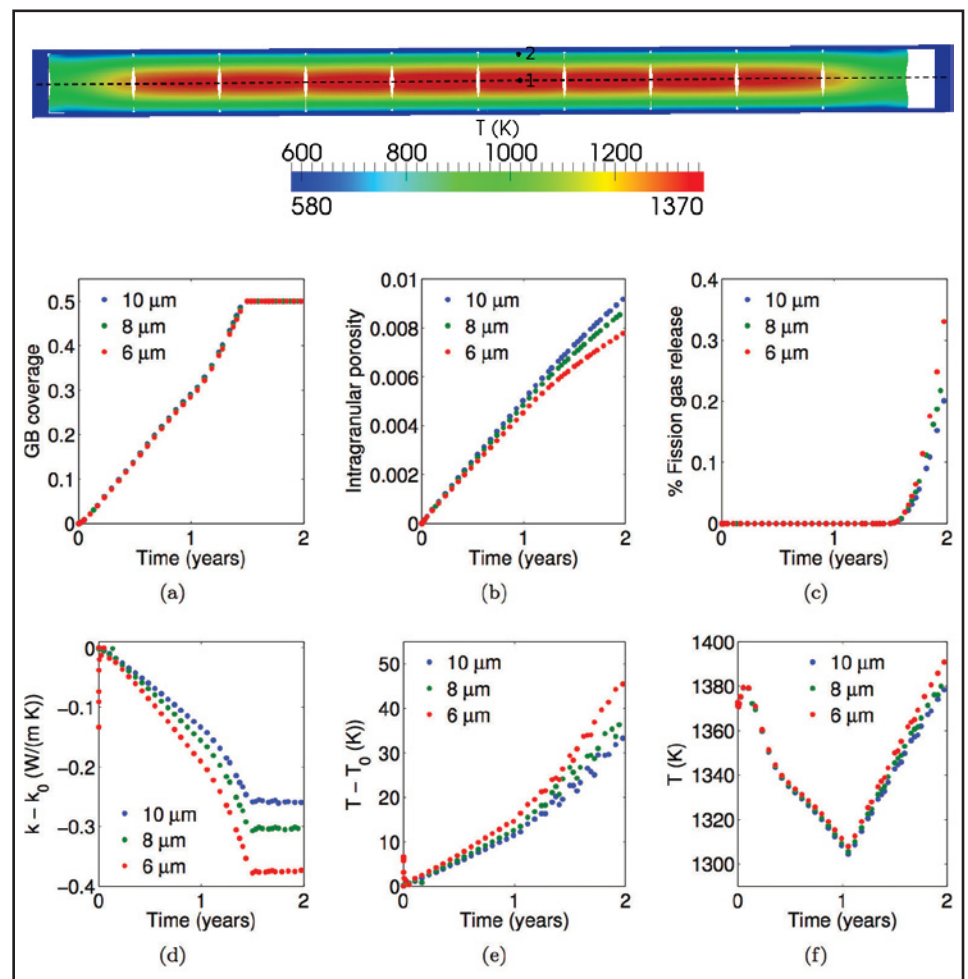


**Figure 6.** Results from the grain radius study at point 1 where (a) shows the change in grain boundary coverage over time, (b) shows intragranular porosity over time, (c) shows the percent of the fission gas that was released vs. time, (d) plots the change in thermal conductivity due to our ISV model over time, (e) plots the change in temperature over time, and (f) shows temperature over time. Note that in each plot, the different colored points represent the three average grain radii. Also, note that the temperature increases due to decreasing grain size because of the decrease in the fuel thermal conductivity and because of the increase in fission gas release. Figure taken from [10].

the thermal conductivity in the gap between the pellet and the cladding. Thus, with this coupled model, decreasing the grain radius decreases the  $\text{UO}_2$  thermal conductivity and the gap conductivity. In this way, multiple effects of fission gas were simultaneously captured with the model.

## Conclusions

In order to develop a more predictive fuel performance modeling capability for accident conditions and advanced fuel designs, INL has developed the MOOSE-BISON-MARMOT suite of codes, where MOOSE is the numerical framework, BISON is the macroscale fuel performance code, and MARMOT is a mesoscale code for the development of mechanistic materials models that consider microstructure effects.

In order to develop mechanistic materials models of radiation effects on fuel behavior, a multiscale approach, bridging from the atomistic to the macroscale, is employed. Atomistic calculations determine important material properties; mesoscale calculations investigate the microstructure evolution to develop mechanistic materials models, which are then used in the macroscale BISON code. This process was demonstrated on the development of a model of the impact of fission gas bubbles on the effective GB resistance within the fuel. The model was then implemented in BISON and used to investigate the impact of grain size on fuel performance.

*Article previously published in the "International Congress on Advances in Nuclear Power Plants and 28th KAIF/KNS Annual Conference," Jeju Island, Korea, April 14-18, 2013.*

## Acknowledgements

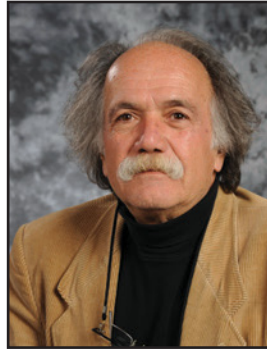
The authors would like to acknowledge the U.S. Department of Energy NEAMS program for funding this work.

## References

1. D.R. Gaston, C. Newman, G. Hansen, and D. Lebrun-Grandie, "MOOSE: A parallel computational framework for coupled systems of nonlinear equations," *Nucl. Eng. Design*, 239, 1768 – 1778 (2009).
2. H. Park, D.A. Knoll, D.R. Gaston, and R.C. Martineu, "Tightly coupled multiphysics algorithms for pebble bed reactors," *Nucl. Sci. Eng.*, 51, 2, 118 – 133 (2010).
3. L. Guo, H. Huang, D.R. Gaston, C.J. Permann, D. Andrs, G. Redden, C. Lu, D. Fox, and Y. Fujita, "A parallel fully-coupled fully-implicit solution to reactive transport in porous media using preconditioned Jacobian-Free Newton-Krylov Method," *Advances in Water Systems, to appear (2013)*.
4. R. Podgorney, H. Huang, and D.R. Gaston, "Massively parallel fully-coupled implicit modeling of coupled thermal-hydrological-mechanical processes for enhanced geothermal system reservoirs," in *Proceedings, 35th Stanford Geothermal Workshop*, Stanford University, Palo Alto, CA, Feb 1-3 (2010).
5. R.L. Williamson, J.D. Hales, S.R. Novascone, M.R. Tonks, D.R. Gaston, C.J. Permann, D. Andrs, and R. Martineau, "Multidimensional Multiphysics Simulation of Nuclear Fuel Behavior," *J. Nucl. Materials*, 423, 149 – 163 (2012).
6. B.W. Spencer, J.D. Hales, S.R. Novascone, and R.L. Williamson, "3D simulation of missing pellet surface defects in light water reactor fuel rods," in *Proceedings from Top Fuel, 2012, Manchester, England, Sept 2-6 (2012)*.
7. M.R. Tonks, D.R. Gaston, P.C. Millett, D. Andrs, and P. Talbot, "An object-oriented finite element framework for multiphysics phase field simulations," *Comp. Mat. Sci.*, 51, 20 – 29 (2012).
8. L.Q. Chen, "Phase-field models for microstructure evolution," *Annu. Rev. Mater. Res.*, 32, 113 – 140 (2002).
9. P.C. Millett and M.R. Tonks "Application of phase field modeling to irradiation effects in materials," *Current Opinion Solid State and Mat. Sci.*, doi:10.1016/j.cossms.2010.10.002.F (2010).
10. M.R. Tonks, P.C. Millett, P. Nerikar, S. Du, D. Andersson, C.R. Stanek, D.R. Gaston, D. Andrs, and R.L. Williamson, "Multi-scale development of a fission gas thermal conductivity model: Coupling atomic, meso and continuum level simulations," *J. Nucl. Mater*, 440, 193–200 (2013).
11. K. Forsberg and A.R. Massih, "Diffusion theory of fission gas migration in irradiated nuclear fuel  $\text{UO}_2$ ," *J. Nucl. Materials*, 135, 140 – 148 (1985).
12. P.G. Lucuta, H.J. Matzke, and I.J. Hastings, *J. Nucl. Materials* 232, 166 – 180 (1996).
13. K. Chockalingam, P.C. Millett, and M.R. Tonks, "Effects of intergranular gas bubbles on thermal conductivity," *J. Nucl. Materials*, 430, 166 – 170 (2012).
14. P. Winter and D. MacInnes, "IAEA technical committee on water reactor fuel element computer modelling in steady-state, transient and accident conditions," Preston, UK, *Paper No. IAEA-TC-657/5.6*, (1988).
15. C.B. Basak, A.K. Sengupta, and H.S. Kamath, "Classical molecular dynamics simulation of  $\text{UO}_2$  to predict thermo-physical properties," 360, 1-2, 210 – 216 (2003).
16. E. Thornton, "Viscosity and thermal conductivity of binary gas mixtures: Krypton-Argon, Krypton-Neon, and Krypton-Helium," *Proceedings of the Physical Society* 76, 104 (1960).
17. J.K. Fink, "Thermophysical properties of uranium dioxide," *J. Nucl. Materials*, 279, 1 – 18 (2000).



**Michael Tonks**, (Ph.D. in Mechanical Engineering from the University of Illinois), is the Computational Microstructure Science Group lead in the Fuels Modeling and Simulation Department at INL, where he develops multiscale models for predicting fuel behavior. He is also the lead developer of MARMOT, a fine element code that predicts microstructure evolution in irradiated materials. Dr. Tonks is a computational materials scientist and joined INL in 2008. He is a member of the American Materials Research Society and the Materials, Minerals and Metals Society and received the Materials, Minerals and Metals Society Structural Materials Division Young Leader Professional Development Award in 2014.



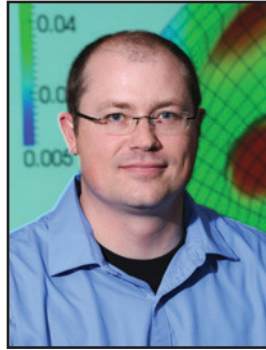
**S. Bulent Biner** (M.Sc., 1973, Istanbul Technical University, Istanbul Turkey, Ph.D. 1981, University of Aston, Birmingham England, M.B.A. 1996, Iowa State University, Ames, Iowa). Prior to joining the Modeling and Simulation Department at INL in 2010, he was a scientist at Ames Laboratory for the U.S. Department of Energy and an adjunct associate professor for Department of Materials Science and also for Department of Aerospace Engineering and Engineering Mechanics at Iowa State University for 22 years. He has over 80 publications in refereed journals and numerous presentations at national and international conferences. He also currently holds two patents.



**Yongfeng Zhang** (Ph.D., 2009, Mechanical Engineering, Rensselaer Polytechnic Institute) is currently a material scientist in the Fuels Modeling and Simulation Department at INL. His expertise lies in atomic scale modeling on the microstructural evolution of nuclear fuels and materials under radiation and mechanical loading. Dr. Zhang has more than 8 years of experience in computational material science. He is the author or co-author of over 30 peer-reviewed journal publications and has delivered over 20 presentations at professional conferences.



**Richard Williamson** (Ph.D., 1989, Mechanical Engineering, University of Idaho) leads the BISON development team within the Fuel Modeling and Simulation Department. He has over 36 years of experience in computational methods research and model development. His current research relates to developing models to simulate nuclear fuel behavior with specific emphasis on complex multiphysics and multidimensional phenomena. Dr. Williamson has over 40 peer-reviewed journal articles and many hundreds of citations to his work.



**Stephen Novascone** (B.S., 1996, Mechanical Engineering, Utah State University; M.S., 1998, Mechanical Engineering, Utah State University; Ph.D., 2003, Mechanical Engineering, University of Idaho) is a research and development engineer with over 15 years of experience. His professional interests are computational mechanics and experiment design. After a brief time at Thiokol analyzing rocket engines, he has spent his career at INL working on a variety of engineering projects. Since 2010, he had worked as a developer for BISON, INL's nuclear fuel performance code. His role on the BISON team is to develop simulation capability, evaluate BISON by comparing simulations results to experiment measurements, and provide technical support for BISON users.



**Benjamin Spencer** (Ph.D., Civil Engineering, University of Colorado) is a member of technical staff in the Fuel Modeling and Simulation Department at INL. In this capacity, he develops, maintains, and supports BISON, which is the fuels performance code in the MOOSE simulation framework. Before joining INL Dr. Spencer spent 9 years at Sandia National Laboratories, where he worked as a software developer on the solid mechanics applications in the SIERRA code suite and as a structural analyst for nuclear safety applications. His technical skills include development and support of massively parallel finite element analysis software and the application of both U.S. Department of Energy and commercial codes for analysis of solid mechanics problems. He is an experienced C++, Fortran, Python, and Perl programmer. .



**Jason Hales** (Ph.D., University of Illinois at Urbana-Champaign) is a computational scientist in the Fuel Modeling and Simulation Department where he develops massively parallel, nonlinear, fully coupled, multi-physics software for internal and external customers. He is a core contributor to BISON, with a principal focus on non-linear solid mechanics development. Before joining INL, Dr. Hales spent 9 years at Sandia National Laboratories, where he worked on the solid mechanics applications in SIERRA. His technical skills include numerical methods, high-performance computing, non-linear solid mechanics, material model development, finite element contact, and multiphysics coupling.



**Derek Gaston** holds advanced degrees in Computational Applied Mathematics and Computer Science. His background is in enabling large-scale, parallel, scientific simulation with a particular interest in software frameworks. Areas of research include generic frameworks for mesh adaptivity, error estimation, code verification and validation, scale bridging, fluid simulation, and fully implicit contact. Derek has previously held a position at Sandia National Laboratory developing simulation frameworks and is currently leading the Computational Frameworks group within the Fuel Modeling and Simulation department at INL. He has received multiple Laboratory Director awards at INL and received a 2011 Presidential Early Career Award for Scientists and Engineers.



**Cody Permann** (M.S. degree, Computer Science, University of Idaho) has over 14 years of experience working in scientific and technical computing fields at INL. As an undergraduate student, he received numerous merit and music-based scholarships. He has made numerous impacts at INL during his tenure, including innovative development of a handheld-based package tracking system still in use at INL today, significant process and cost savings improvements to a standard genomic patenting process, and most recently has contributed to the success of the MOOSE framework at INL. He is currently continuing his research and education toward his Ph.D. while studying at Mississippi State University.



**David Andrs** (Ph.D., Computer Science, University of West Bohemia, Czech Republic) is a software engineer in the Modeling and Simulation Department at INL. In this capacity, he works on developing MOOSE software. He also works on design and development of the nuclear power plant safety code RELAP-7.



**Steven Hayes** (Ph.D., Texas A&M University) is a nuclear engineer in the Nuclear Fuels and Materials Division. Dr. Hayes has extensive experience in the development and testing of nuclear fuels, including design of irradiation experiments, post-irradiation examinations, and fuel performance modeling and simulation. He serves as a leader in two national nuclear research programs: (1) as Technical Lead for Transmutation Fuel Development in the Fuel Cycle Research and Development Program's Advanced Fuel Campaign, and (2) as Technical Lead for the Fuels Product Line in the NEAMS Program.



**Paul Millett** (B.S., 1997, Vanderbilt University; Ph.D., 2006, University of Arkansas) is an Assistant Professor of Mechanical Engineering at the University of Arkansas (2013-present), after 7 years at INL (2006-2013). His research activities include theoretical and computational analysis of microstructure evolution in materials subjected to extreme environments. In particular, he has developed microstructural models of the transport of fission products and thermal heat within nuclear oxide fuels. These models have been developed through use of a variety of computational simulation techniques including the phase-field, Monte Carlo, and percolation methods.



**David Andersson** (Ph.D., Materials Science and Engineering, Royal Institute of Technology (KTH), Stockholm, Sweden) is a staff scientist in the Materials Science and Technology division at Los Alamos National Laboratory, where he works on modeling of nuclear fuels using atomic level simulations. As a postdoc at Los Alamos National Laboratory, Dr. Andersson's work focused on modeling the structure and chemistry of actinide oxides, in close collaboration with synchrotron x-ray scientists. After being converted to staff scientist, Dr. Andersson has spent most of his time working for the U.S. Department of Energy NEAMS Program. He is heavily involved in developing multiscale modeling and simulation tools for fission gas transport and thermal conductivity in oxide nuclear fuels.



**Chris Stanek** (B.S., Materials Science and Engineering, Cornell University, McMullen Scholar; Ph.D., Materials, Imperial College London). Stanek is currently a staff scientist at Los Alamos National Laboratory. His research interests focus on the interaction between multidimensional defects in ceramics, primarily via atomistic simulation. He is particularly interested in materials for nuclear energy, including oxide fuels, crystalline waste forms, and scintillator radiation detectors. Currently, Stanek is the Materials Performance Optimization focus area lead of the Consortium for Advanced Simulation of Light Water Reactors Energy Innovation Hub. Stanek has over 80 publications related to defect behavior in ceramics.



# **Synergistic Smart Fuel for Microstructure Mediated Measurements**

# Synergistic Smart Fuel for Microstructure Mediated Measurements

J.A. Smith (INL), R. Ali, S.L. Garrett (PSU)

Advancing the nuclear fuel cycle and next generation nuclear power plants requires enhancing our basic understanding of fuel and materials behavior under irradiation. The two most significant issues limiting the effectiveness and lifespan of the fuel are the loss of thermal conductivity of the fuel and the mechanical strength of both fuel and cladding. The core of a nuclear reactor presents an extremely harsh and challenging environment for both sensors and telemetry due to elevated temperatures and large fluxes of energetic and ionizing particles from radioactive decay processes. The majority of measurements are made in reactors using “radiation-hardened” sensors and materials. A different approach has been pursued in this research that exploits high temperatures and materials that are robust with respect to ionizing radiation. This synergistically designed thermoacoustic (TAC) sensor will be self-powered, wireless, and provide telemetry. The novel sensor will be able to provide reactor process information even if external electrical power and communication are unavailable. In addition, the form factor for the sensor is identical to the existing fuel rods within reactors and contains no moving parts. Results from initial proof-of-concept experiments designed to characterize porosity, surface properties, and monitor gas composition will be discussed.

## Introduction

Advancing the nuclear fuel cycle and next generation nuclear power plant requires an enhanced fundamental understanding of fuel and materials behavior under irradiation. The two most critical issues limiting the performance and lifetime of the fuel are the degradation of the thermal conductivity of the fuel and the mechanical integrity of both the fuel and cladding. To better understand thermal conductivity, high-fidelity in-core temperature and microstructure measurements are needed. Several technology barriers exist for implementing sensors into reactor vessels, especially in high-neutron-flux regions. They include (1) high-temperature materials and sensors that can operate up to 1500°C, (2) radiation-hardened materials and electronics, and (3) wireless communication methods compatible with harsh environments.

To better understand the mechanical integrity of fuels, we must have means to perform nondestructive analysis of the material. An efficient fuel must have the right microstructure within the reactor to perform properly. It is known that the evolution of defects in microstructures can change the overall material porosity. This research demonstrates that changes in porosity can be detected with a heat-engine-based sensor and remotely monitored as a change in acoustic frequency. Microstructure changes in fuel can be monitored directly, by sensing changes in porosity, or indirectly by monitoring fission gas release. Initial experimentation has been performed using surrogate materials representative of fuels/cladding, with precisely controlled porosity.

It has become increasingly evident that a paradigm shift is necessary to develop effective sensors for the harsh nuclear environment. The fundamental question that should drive sensor design is how the harsh environment can be used to the sensors’ advantage. Instead of working against the environmental conditions, the sensor must be synergistic and take advantage of its environment, as well as the intrinsic power source, cooling mechanisms, and thermal gradients provided in the reactor core.

This research introduces a TAC sensor that enables both high-temperature and porosity-sensing capabilities within a nuclear environment. The TAC requires no mechanical pump, moving parts, or electricity to provide a wireless indication of temperature. TAC sensors work synergistically with harsh in-pile environments and can potentially be incorporated within current cladding and capsule designs for in-pile use. The sensor is self-powered by the temperature differential between the fuel and the coolant.

Since TAC devices can be constructed from robust materials and have no moving parts, they are ideally suited for the hostile conditions within a reactor. The existing geometry of the Advanced Test Reactor experimental fuel rods and capsules makes excellent acoustical resonator cavities. The temperature differential between the fuel ( $\approx 1,000^\circ\text{C}$ ) and the cooling water ( $\approx 60^\circ\text{C}$ ) in the Advanced Test Reactor provide the ideal power source for the TAC device.

## Thermoacoustic Engine

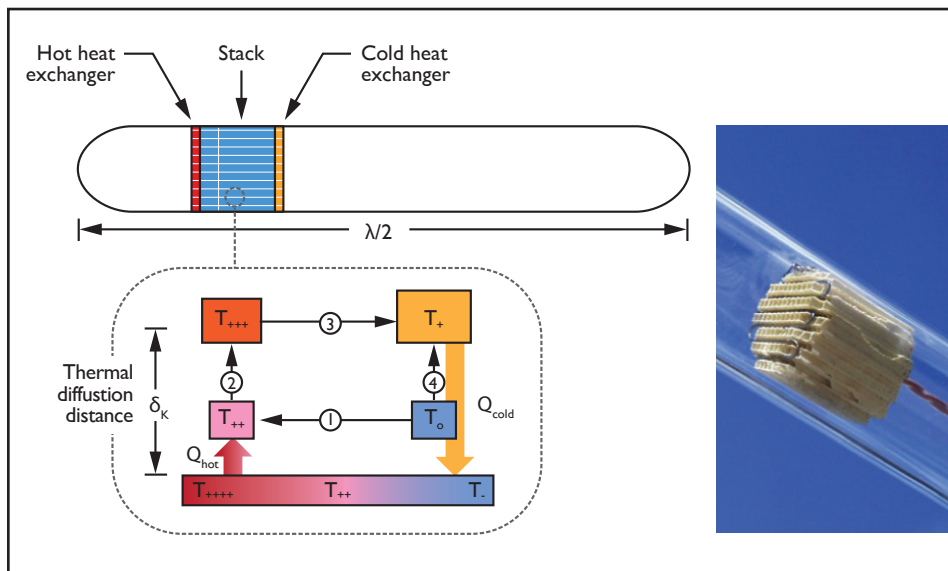
A TAC engine can be defined as the generation of acoustic waves from heat transfer. The TAC engine converts heat from a high-temperature source into acoustic power, while rejecting waste heat to a low-temperature sink (i.e., coolant) [1-3]. The temperature variation, imposed across a section of an acoustic cavity, drives heat into the gas, forcing the gas to do work on its surroundings and amplifying the acoustic oscillations. Each parcel of oscillating gas takes heat from the parcel behind and transfers it forward to adjacent gas molecules. A steep thermal gradient is necessary to induce TAC operation. For laboratory testing, the TAC device is powered by a resistive heater. In a reactor, fission or gamma heating will provide the gradient to power the TAC. The temperature within the reactor will then be related to the TAC frequency [4].

Figure 1 illustrates the operation of a stack-based TAC engine. The engine contains the stack material (Figure 1 and hot and cold heat exchangers in a closed-closed (half-wavelength) resonator [1, 2]. The stack that is used consists of a regular array of parallel channels. These stacks are the substrates for catalytic converters found in cars and can be made from any channeled material with high heat capacity such as glass or stainless steel. Heat is applied to the hot end of the stack and creates a temperature gradient across the stack. The stack's cold end needs to be maintained at a lower temperature. The TAC phenomenon is similar to a four-stroke car engine. Cool fuel gets injected and compressed to increase the gas temperature. As the gas reaches maximum compression, heat gets input (spark). As the combusted gas expands, gas temperature drops. The combusted gas and heat are exhausted. The cycle begins anew.

The four-stroke TAC cycle can be illustrated using Figure 1. When a gas parcel moves to the left (Step 1), the parcel's temperature increases ( $T_o \rightarrow T_{++}$ ) by adiabatic compression.

Heat is then transferred from the hot end of the stack to the gas parcel during Step 2. This increases the gas parcel's temperature ( $T_{++} \rightarrow T_{+++}$ ) and pressure. In Step 2, the gas parcel is at a stable high pressure. The increased temperature causes an increase in volume of the parcel. Consequently, work ( $p\Delta V$ ) is done to the gas parcel by the flow of heat from the stack to the gas parcel. The pressure increase pushes the gas parcel back slightly more each acoustic cycle.

The gas parcel then moves to the right (Step 3) and is cooled ( $T_{+++} \rightarrow T_+$ ) by adiabatic expansion. Heat is transferred from the parcel to the stack (Step 4). This lowers the gas parcel's temperature ( $T_+ \rightarrow T_o$ ) and pressure. Since the removal of heat from the gas occurs at a fixed low pressure, the volume of the parcel is decreased. Work ( $p\Delta V$ ) is done to the gas parcel. This pulls the gas back toward the hot end of the stack by slightly more each acoustic cycle. Eventually, the amplitude of the acoustic resonance grows to a steady-state level. Steady-state operation occurred when the acoustic energy dissipated during each cycle was equal to the TAC acoustic energy. Lord Rayleigh intuitively understood the TAC process in the 19th century [5] and stated a "vibration is encouraged when heat is added during compression and removed during rarefaction."



**Figure 1.** (Left) Half-wavelength resonator and the four-part cycle of a gas parcel within the stack. (Right) ceramic stack material inside a test tube. (Photo courtesy of Reh-Lin Chen).

## Experimental Capsule as a Thermoacoustic Resonator

An experimental capsule designed for insertion into the core of the Advanced Test Reactor at INL has been modified to develop a laboratory prototype TAC sensor [4, 6-8]. The Separate Effects Testing (SET)-1 capsule has been adapted to accommodate a stack. Figure 2 illustrates the TAC capsule designed and successfully used for thermometry experiments [4].

The cylindrical resonator in Figure 2 represents a typical SET-1 capsule. The heat source will be nuclear fuel or gamma-heated material. Electromagnetic radiation transfers heat to the stack's hot end. The stack's cold end is kept cool by immersion of the resonator in the cooling fluid and from the acoustic streaming [9-10] produced by sound. The resulting temperature gradient

is maintained in this manner for sustained acoustic resonance.

The sound that is produced in the capsule will propagate by radiating throughout the cooling fluid in the reactor. The omni-directional sound can be monitored at remote locations away from the high temperatures and radiation of the reactor core. The resonant acoustic frequency is representative of an effective temperature within the capsule. Additionally, there are no physical moving parts to fatigue or fail, and no electrical cabling requirements inside the capsule.

## Experimental Plan and Setup

Testing for direct and indirect measure of microstructure will be performed by changing the parameter of interest. The direct measure of microstructure will be performed

by inserting porosity specimens of various pore sizes into the hot end of the TAC's resonant cavity. The porosity specimens consist of various honeycombed steel pucks of fixed geometry. In addition, a dynamic porosity experiment will be performed using a porous puck that has been immersed in wax. The wax blocks the pores, making a nonporous specimen. When the specimen is placed in the TAC sensor, the wax melts and runs out of the porosity specimen. Resulting modulation to the acoustic signal will be evaluated. The indirect measurement of microstructure will be simulating fission-gas release by filling the resonant cavity with different gases. The baseline gas will be atmospheric air.

A water tank is used to simulate the reactor containment/coolant, as shown in Figure 3. The oscillatory movement of gas results in an omni-directional "singing tube" that launches acoustic energy into the water and into the room. A computer-controlled data acquisition system is configured to measure TAC's internal static pressure, dynamic pressure, gas temperatures in several locations, and power applied to the heater.

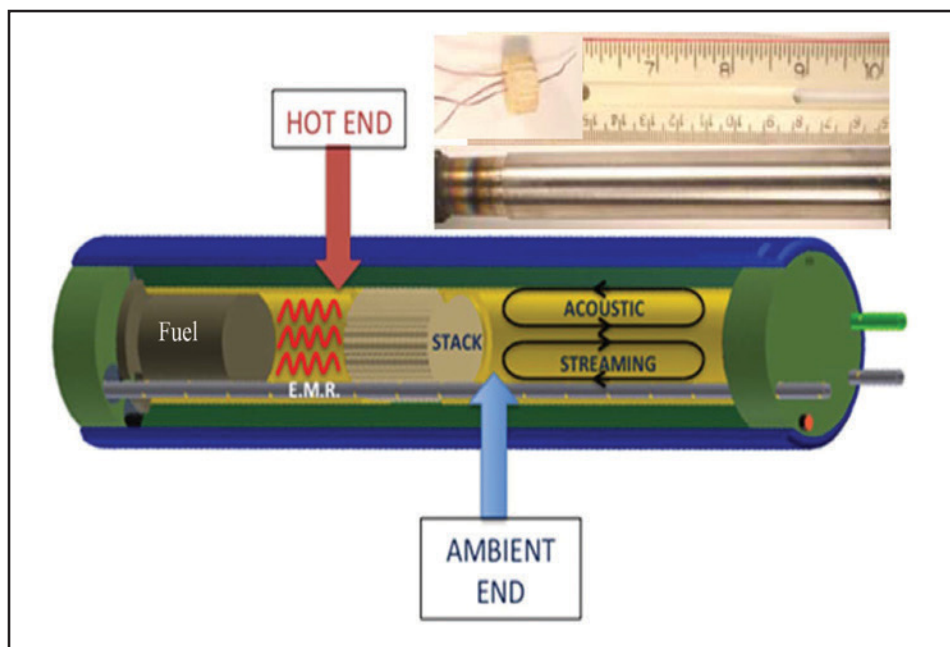


**Figure 2.** SET-1 experimental capsule adapted to create a prototype TAC sensor. The actual prototype is shown just above the schematic and the stack is shown at the approximate location within the capsule. The fuel heats the stack's hot end via electromagnetic radiation. Heat transfer from the stacks' ambient end is enhanced by the acoustic streaming gas flow, which is indicated by the oval arrows. Streaming also enhances the heat transfer from the gas to the surrounding cooling fluid.

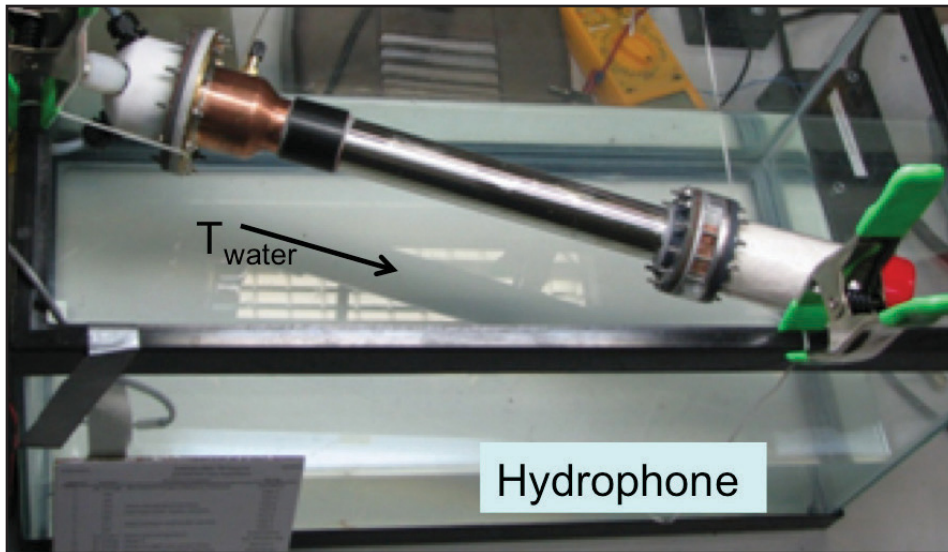


**Figure 3.** Submersible TAC sensor is shown suspended above the aquarium test tank prior to testing.



**Figure 4.** Porosity arrangement is displayed in graphic of the sample within the TAC for mediated microstructure measurements.

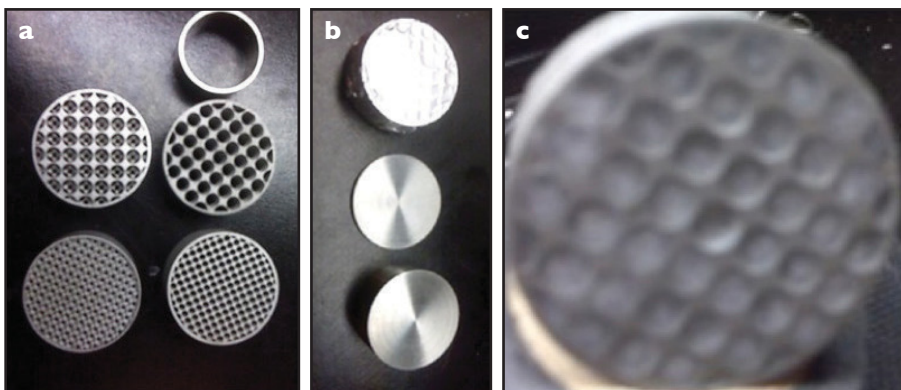


**Figure 5.** Photographs of microstructure specimens and spacers used for testing. (a) Samples representing interconnected porosity. (b) Samples representing surface microstructure and used as spacers. A low-density solid puck was simulated by wrapping a 3.46-mm aligned porous specimen with tin foil (top). (c) Picture of 3.46-mm aligned pores porosity specimen with wax filled pores. (Diameter of specimen is 32 mm, the height is 12.7 mm.)

## Porosity Experiments

The leading causes of fuel failure is swelling, crack growth, and deleterious interaction between fuel and cladding. Methods to measure in-core microstructure properties are desired. TAC sensors must enable the linking of fundamental microstructural damage mechanisms to the macroscopic degradation of the fuel components to be useful. TAC's ability to characterize microstructure has been evaluated. Experiments were conducted by fabricating steel porosity specimens and placing them within the hot end of the TAC (Figure 4). It should also be noted that specimens can be placed in the cold end of the TAC, thus enabling separate effects testing with a temperature differential on the order of 400°C at the same radiation flux.

Table 1 shows the results from the porosity experiments. Frequency invariants [4, 8] are recorded because the Ideal Gas Law predicts that the ratio of acoustic frequency to square root of absolute temperature is a constant. The hot end invariant is obtained from taking the frequency of the acoustic resonance and dividing it by the square root of the temperature in the hot end of TAC resonator (behind the heating coil). The cold end invariant is obtained in a similar manner. The spherical pores come in two sizes (3.46-mm and 1.73-mm diameters) and two configurations (columns aligned and columns offset). The microstructural specimens are shown in Figure 5.

Table 1 illustrates that the TAC exhibits different behavior in the presence of porous samples within the TAC and with microstructure configuration. The immediate feature that is clearly reinforced by the table is the robust nature of the cold end invariant. Significant variations in the measurements occur in the hot end. There is significant variation between the two 1.73-mm pore alignments in hot end invariants and temperatures. There does not appear to be any significant variations between the 3.46-mm pore alignments.

Table 2 shows a number of interesting trends based on the geometry of the fuel pellets. Note that the cold end invariant tends to follow the mass of the object inserted into the TAC engine, while the other parameters do not show an obvious correlation with mass. The hot end measurements tend to be independent of the placement of the specimen (with and without spacer). The placement of foil over the pucks' front surfaces had the largest effect on the hot end measurements. The effects from the foil are strong indications that the hot end is sensitive to surface microstructure. The cold end temperature remains consistently near the water temperature within a few °C. It is interesting to note that the long puck has the largest effect on the cold end invariant.

It is also interesting to note that hot end temperatures with the porous pucks tend to run hotter than solid pucks. The solid puck hot end temperatures clearly show that loss of convective flow has a minimal impact on hot end temperature when compared to baseline data. The exception is the foil-covered specimen, where another heat transfer mechanism is clearly involved. Thus, there are strong indications that the hot end is sensitive to bulk and surface microstructure.

**Table 1. Results from the TAC porosity experiments.**

Specimen—Porous Disks	Weight (grams)	Geometry Diameter × Height (mm)	Cold End Invariance (Hz/√K)	Hot End Invariance (Hz/√K)	Hot End Temp (Celsius)	Cold End Temp (Celsius)
Empty (baseline)	NA	NA	18.74	16.31	130	31.5
1.73 mm Aligned	33.5	32 × 12.7	19.28	15.91	163	31.7
1.73 mm Offset	23	32 × 12.7	19.25	15.51	205	31.5
3.46 mm Aligned	32	32 × 12.7	19.27	16.1	172	32.0
3.46 mm Offset	13	32 × 12.7	19.19	16.09	169	30.7

**Table 2. Behavior of mock-up fuel pellets of various dimensions and weights. Spacer serves as a TAC resonator standoff (5-gram mass).**

Specimen (Solid Pucks)	Geometry Diameter × Height (mm)	Weight (grams)	Cold End Freq Invariant (Hz/√K)	Hot End Freq Invariant (Hz/√K)	T Hot End (Celsius)	T Cold End (Celsius)
Long, with spacer	32 × 25.4	86	NA (acoustic onset never achieved)	NA	248.8	34.2
Long, no spacer	32 × 12.7	81	19.4	16.5	153.7	29.5
3.46-mm aligned porous puck and foil, with spacer	32 × 25.4	39	19.25	14.5	236.4	33.3
3.46-mm aligned porous puck and foil, no spacer	32 × 12.7	34	19.3	14.65	236.0	33.1
Short, spacer	32 × 15.8	17	19.2	16.4	143.7	32.3
Short, no spacer	32 × 3.1	12	19.05	16.3	144.2	33.6
80, long-term baseline (empty)	NA	NA	19.1	16.2	145	29.0

## Dynamic Microstructure Experiments

The porosity specimen consists of a honey-combed puck (3.46-mm aligned pores) that has been immersed in wax (Figure 5). The wax blocks the pores, making a nonporous specimen. When the specimen is placed in the TAC sensor, the wax melts and runs out of the specimen.

Resulting modulation to the acoustic signal has been noted, as shown in Figure 6. The salient phenomenon is that the movement of the melting wax perturbed the cavity such that the sonic resonance is temporarily extinguished. Once the melted wax stopped flowing, the resonance started back up, but at a slightly higher frequency. The wax-melt data show that the TAC engine can clearly track dynamic bulk microstructural (opening of interconnect pores) events.

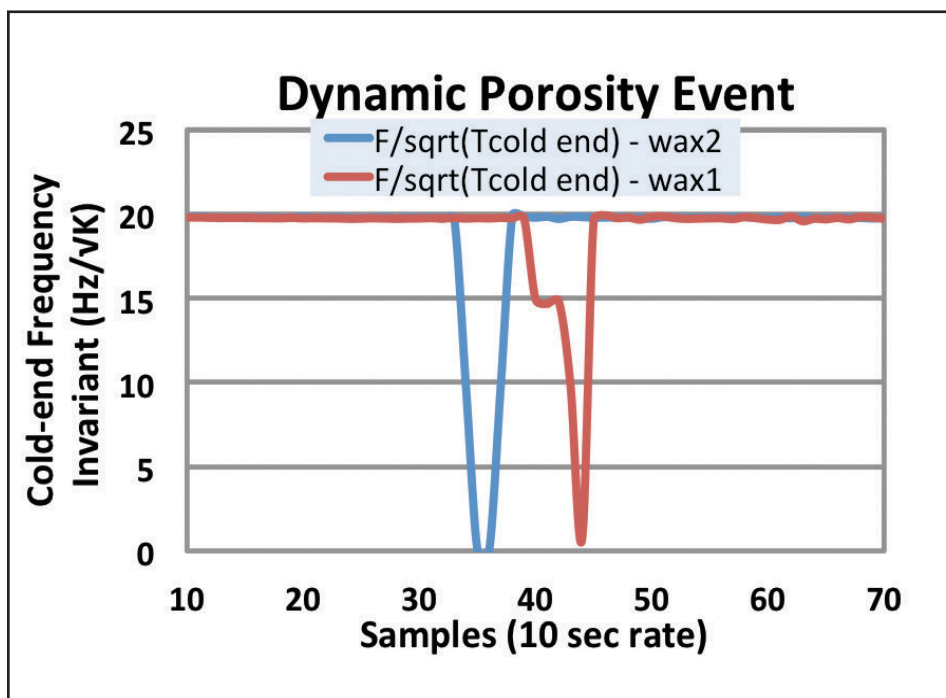


**Figure 6.** Plot showing the frequency invariant of the porosity specimen with time. As the porosity specimen heats up, the wax melts. The flowing wax keeps the TAC sensor from resonating and the signal drops out near 35 to 45 Sa. Once the liquid wax has finished flowing, the cavity is stabilized and sound resonance restarts. However, the recovered signal has slightly more variation.

## Gas Density Experiments

The TAC strategy can be extended to remote sensing of fission gas (particularly krypton and xenon) evolution as part of the radioactive decay of the fuel [11]; although, to separate effects, pairs of fuel rod resonators may be required (e.g., one to measure temperature and the other to identify gas mixture concentration). An indirect measure of microstructure evolution is simulated by filling the resonant cavity with various gasses. The TAC technique has merit because the universal gas constant is determined from the measurement of acoustical resonances at the National Institute of Standards and Technology. Future TAC designs will measure the rate of production of fissile gases, krypton and xenon, which are influenced by microstructural changes.

Initial experiments performed at INL confirm the practicality for fission gas monitoring, as shown in Table 3. The tabulated data show that resonance frequency is directly related to the ratio of the square root of the polytropic coefficient ( $\gamma = c_p/c_v$ ) to the mean molecular mass,  $M$ , of the gases. Evolving the gas within the TAC resonator will result in variations in the frequency of the sound radiated. The measured frequency ratios are not exactly equal to those based on the properties of the gases due to the fact that the temperatures during all four measurements were nearly, but not exactly, equal and the humidity of the air sample was unknown. Although “dry” air has a molecular weight larger than nitrogen, the presence of humidity in the air dropped the average molecular weight below nitrogen. TAC demonstrates the ability to resolve atmospheric air (~70% nitrogen) from pure nitrogen and moisture content. Thus, the TAC sensor can also be a humidity sensor if properly configured.

Accurate *in situ* measurement of fission gas release will enable the prediction of microstructure evolution and support development of fuel microstructure that can be designed to maximize fuel lifetime and reliability. The TAC engine can clearly differentiate gas molecules and mixtures that may result from microstructure changes and fission gas release.

## Conclusion

A novel sensor based on TAC phenomenon has been demonstrated. The TAC sensor is shown to be synergistic with conditions within a nuclear reactor. TAC technology takes advantage of the large thermal gradients caused by the nuclear fuel and surrounding cooling water and, therefore, requires no external power source. Because the phenomenon is simplistic and has no moving parts, the sensor can be constructed from inexpensive, yet robust materials. The signal generated is

**Table 3.** Acoustic frequency variation is shown for four different gases. The ratio of the measured frequencies to the frequency in helium is compared to the ratio calculated using molecular mass and the ratio of specific heats,  $\gamma = c_p/c_v$ .

Gas	Molecular Mass (a.m.u.)	Polytropic Coefficient ( $\gamma = c_p/c_v$ )	Ave. Freq. (Hz)	Freq. Ratio f/f <sub>He</sub>	Sq. Root Ratio ( $\gamma/M$ ) <sup>0.5</sup>
Helium	4.00	1.667	976.2	1.000	1.000
Nitrogen	28.01	1.400	315.7	0.323	0.346
(Dry) Air*	28.96	1.403	322.7	0.331	0.341
Xenon	131.29	1.667	173.0	0.177	0.175

\* Humid room air was used in the experiment

Note that the results for "room" air are slightly larger than nitrogen due to natural humidity.

acoustic and, thus, is transmitted efficiently through the cooling water or metal pipes/structures within the reactor.

Although there are a few labs worldwide working with TAC technology as applied to heat engines, INL is the only known laboratory that is developing TAC sensors. Novel process (e.g., temperature, gas composition, extension, pressure, etc.) and microstructure sensors have been developed and successfully tested at INL. The TAC engine can also be used for separate effects testing by providing hot and cold regions within the resonant cavity that have a temperature differential of  $\approx 400^\circ\text{C}$  with similar radiation flux. Thus, a whole new measurement architecture paradigm has been opened from the ability to have heat engine-based wireless and self-powered sensors. The new sensing architecture paradigm will reduce experiment complexity and be simple, robust, easy to install, and cost-effective.

The experiments discussed have been designed to demonstrate the microstructure characterization potential of TAC sensors. Two types of microstructure monitoring have been evaluated. Both direct monitoring of effects from interconnected porosity and indirect microstructure characterization from fission gas composition have been demonstrated. The TAC sensor differentiated the following gasses according to their

molecular weight: nitrogen, helium, xenon, and atmospheric air. The TAC sensor has sufficient fidelity to clearly differentiate between nitrogen and atmospheric air. Dynamic microstructure evolution has also been monitored. In a complex environment (such as a nuclear reactor), multiple sensors will be required to deconvolve various environmental conditions changing simultaneously.

Because the TAC sensor is robust, wireless, self-powered, and economical, it is an excellent choice as a new approach for in-pile monitoring within a nuclear reactor. The natural and synergistic properties of the TAC engine provide the confidence that testing within a reactor will be successful. A TAC sensor specifically designed for the Very High-Temperature Reactor Program is scheduled to go into a laboratory mock-up of an advance gas reactor test train in the winter of 2013. The SET-1 prototype for the Fuel Cycle Research and Development Program is scheduled for insertion in 2015.

*Article previously published in the "40th Quantitative Nondestructive Evaluation (QNDE) & 10th International Conference on Barkhausen Noise & Micromagnetic Testing (ICBM) Conference," Denver, CO, July 21-26, 2013.*

## Acknowledgements

This work was sponsored by the Department of Energy Office of Nuclear Energy: Fuel Cycle Research and Development and Very High-Temperature Reactor Programs.

## References

1. G.W. Swift, *Thermoacoustics: A unifying perspective for some engines and refrigerators*, Acoustical Society of America through the American Institute of Physics, 2002; ISBN 0735400652.
2. S.L. Garrett and S. Backhaus, "The Power of Sound," *American Scientist*, 88 (6), 516-525 (2000).
3. S.L. Garrett, "Resource Letter TA-1: Thermoacoustic engines and refrigerators," *Am. J. Phys.*, 72 (1), 11-17 (2004).
4. R.A. Ali, S.L. Garrett, J.A. Smith, and D.K. Kotter, "Thermoacoustic thermometry for nuclear reactor monitoring," *IEEE J. Instrumentation & Measurement*, 16 (3), 18-25 (2013).
5. J.W. Strutt (Lord Rayleigh), *Theory of Sound*, Vol. II (Dover reprint, New York, 1945) §322.
6. R.A. Ali and S.L. Garrett, "Heat transfer enhancement through thermoacoustically-driven streaming," *Proc. Mtgs. Acoust.*, 19, 030001 (2013).

7. S.L. Garrett, J.A. Smith, and D.K. Kotter, “Thermoacoustic Enhancements for Nuclear Fuel Rods,” U.S. Provisional Patent Application No. 61/683, 992 (Aug. 16, 2012).
8. R.A. Ali, S.L. Garrett, J.A. Smith, and D.K. Kotter, “Thermoacoustic device for nuclear fuel monitoring and heat transfer enhancement,” *J. Acoustical Soc. of America.*, 132 (3) 1993 (2012).
9. Gopinath, N.L. Tait, and S.L. Garrett, “Thermoacoustic streaming in a resonant channel: The time-averaged temperature distribution,” *J. Acoust. Soc. Am.*, 103 (3), 1388–1405 (1998).
10. G. Penelet, M. Guedra, V. Gusev, and T. Devaux, “Simplified account of Rayleigh streaming for the description of nonlinear processes leading to steady state sound in thermoacoustic engines,” *Int. J. Heat and Mass Transfer*, 55, 6042–6053 (2012).
11. W.M. Stacey, *Nuclear Reactor Physics*, 2nd ed., Wienheim: Wiley & Sons Inc. (2007).



**James A. Smith** (B.S., Engineering Science, Iowa State University, M.S. and Ph.D., Engineering, Texas A&M) is a Materials Characterization and Processes Systems Engineer at the Department of Energy's INL. He has worked at AT&T Bell Laboratories, Corning Incorporated, and the Mayo Clinic prior to joining INL. Jim is an innovative and goal oriented systems engineer/project manager with over 20 years of diverse experience, solving complex and ambiguous opportunities from first principles. He is diligent in envisioning new possibilities and developing visionary strategies that progress toward a shared vision. He is known for quickly turning system concepts into plant prototypes by developing close collaborations and understanding customer needs. He specializes in developing products and processes through pioneering measurements and data analysis techniques.



**Randall A. Ali** (B.S.E.E., University of the West Indies, Trinidad; M.S., 2013, Acoustics, Penn State, including research in TAC) is currently a member of the teaching faculty at the University of the West Indies in Trinidad. In addition to research and teaching, he is active in science education and development of acoustical demonstration apparatus for K-12 students. His previous research has involved measuring and modeling behavior of steel pans, which is the indigenous musical instrument of Trinidad and Tobago.



**Steven Garrett** received his Ph.D. in Physics from the University of California Los Angeles in 1977. He continued research in quantum fluids at the University of Sussex in England, followed by 2 years in the Physics Department at the University of California at Berkeley as a Fellow of the Miller Institute for Basic Research in Science. Dr. Garrett joined the faculty of the Naval Postgraduate School in 1982, where his research efforts were concentrated on the development of fiber-optic sensors and TAC refrigerators. He left the Naval Postgraduate School in 1995 to assume his current position as a Professor of Acoustics in the Graduate Program in Acoustics and as Senior Scientist in the Applied Research Laboratory, both at Penn State, where he is continuing his research in TAC engines and refrigerators. In 2001, he was a Fulbright Fellow at the Danish Technical University and in 2008 a Jefferson Fellow in the U.S. State Department where he served as a Senior Science Advisor East Asia and the Pacific. Professor Garrett is a Fellow of the Acoustical Society of America and recipient of the Popular Science Magazine Award for Environmental Technology, the Helen Caldecott Award for Environmental Technology, the Rolex Award for Enterprise (environment category), and has been issued over two dozen patents.

# **Assessment of Survival or Ultrasonic Transducers Under Neutron Irradiation**

# Assessment of Survival or Ultrasonic Transducers Under Neutron Irradiation

J.E. Daw, J.L. Rempe, J. Palmer (INL), B. Tittmann, B. Reinhardt (PSU), G. Kohse (MIT), P. Ramuhalli (PNNL), H.T. Chien (ANL)

## Introduction

Many U.S. Department of Energy-Office of Nuclear Energy (DOE-NE) programs are investigating the long duration irradiation performance of candidate new fuels and materials for use in nuclear reactors. Ultrasonic measurements have a long and successful history of use for materials characterization, including detection and characterization of degradation and damage [1], measurement of various physical parameters used for process control (such as temperature and flow rate) [2], and in nondestructive evaluation. Although many types of ultrasonic sensors can be used to measure different properties of interest, all ultrasonic sensors incorporate a transducer, which can limit the survivability of the sensor in an irradiation test. The development of ultrasonic tools to perform different in-pile measurements requires a fundamental understanding of the behavior of ultrasonic-transducer materials in high-radiation environments. Irradiation studies of ultrasonic transducers have been described in literature, but a one-to-one comparison of these studies is difficult because materials and test conditions often differ. Additionally, tests to date are generally at lower flux/fluences than what might be seen in U.S. material test reactors (MTRs).

Pennsylvania State University (PSU) leads an effort that was selected by the Advanced Test Reactor National Scientific User Facility (ATR NSUF) for irradiation of an ultrasonic transducer in the Massachusetts Institute of Technology (MIT) Nuclear Research Reactor (MITR). This test is an

instrumented lead test, allowing real-time signals to be received from the transducers. The test is unique because it is the first irradiation to include piezoelectric transducers that rely on the electric charge that builds within certain materials under mechanical stress, and magnetostrictive transducers that rely on the tendency of ferromagnetic materials to change shape as they are magnetized. Additionally, it exposes the included transducers to higher fluences than were achieved in prior irradiations. The objective of this test is to evaluate the degradation of candidate transducer materials under irradiation. It has been designed to provide fundamental data on piezoelectric and magnetostrictive material performance in irradiation environments; hence, these data are directly comparable to results of prior irradiations. Collaborators in this endeavor include PSU, the Massachusetts Institute of

Technology (MIT), Idaho National Laboratory (INL), Pacific Northwest National Laboratory (PNNL), Argonne National Laboratory, and the French Commissariat à l'énergie atomique et aux énergies alternatives.

## Background

Several U.S. DOE-NE programs are investigating new fuels and materials for advanced and existing reactors, including sodium-cooled faster reactors (SFRs), high-temperature gas-cooled reactors, and light water reactors (LWRs). Significant portions of these programs focus on characterizing the irradiation performance of these fuels and materials.

Some key parameters needed to evaluate fuel performance, which could potentially be



Research team participants discussing test capsule design (left to right, Pradeep Ramuhalli, PNNL; Brian Reinhardt, PSU; Gordon Kohse, MIT; Joshua Daw, INL, and Hual-Te Chien, Argonne National Laboratory).

**Table 1. Summary of desired fuel measurement parameters for irradiation testing.**

Parameter	Representative Peak Value	Desired Accuracy	Desired Spatial Resolution
Fuel Temperature	Ceramic LWR: 1400°C	2%	1-2 cm (axially)
	Ceramic SFR: 2600°C		0.5 cm (radially)
	Metallic SFR: 1100°C		
	Tristructural-isotropic (TRISO) High-Temperature Gas Reactor: 1250°C		
Cladding Temperature	Ceramic LWR: <400°C	2%	1-2 cm (axially)
	Ceramic SFR: 650° C		
	Metallic SFR: 650° C		
Fuel Rod Pressure	Ceramic LWR: 5.5 MPa	5%	NA
	Ceramic SFR: 8.6 MPa		
	Metallic SFR: 8.6 MPa		
Fission Gas Release	0-100% of Inventory	10%	NA
Fuel and Cladding Dimensions and Density	Initial Length: 1 cm	1%	NA
	Outer Diameter/Strain: 0.5 cm/5-10%	0.10%	NA
	Fuel-Cladding Gap: 0-0.1 mm	0.10%	NA
	Density:	2%	NA
	Ceramic: < 11 g/cm <sup>3</sup> ; Metallic: < 50 g/cm <sup>3</sup> ; TRISO pebble/compact: 2.25 g/cm <sup>3</sup>		
Fuel Microstructure	Grain size, 10 mm	5%	1-10 mm
	Swelling/Porosity: 5-20%	2%	NA
	Crack formation and growth	2%	10-100 mm
Thermal Conductivity	Ceramic: 1-5 W/m·K	4%	<1 cm (radially)

**Table 2. Selected instrumentation available in MTRs.**

Parameter	Sensor	Comments
Temperature	Melt Wires	Peak value, resolution limited by number of wires, post-irradiation examination (PIE) required
	Silicon Carbide Temperature Monitor	Peak value, 100–800°C temperature range, PIE required
	Thermocouples (Types N,K)	1100°C maximum operating temperature, limited by constituent migration
	Thermocouples [Doped Mo/Nb-alloy High-Temperature Irradiation-Resistant Thermocouples (HTIR-TC)] [7]	1800 °C maximum operating temperature, limited by electrical insulation degradation
	Thermocouples (Types C, D, B, R, and S)	Decalibration due to transmutation caused by thermal neutron flux
Density/Displacement	Linear Variable Differential Transformer	Qualified to 500°C
	Diameter Gauge	Qualified to 500°C
Crack Initiation/Growth	Direct Current Potential Drop Method	Sensitive to water chemistry, accuracy limited to ~20%
Young's Modulus	Loaded Creep Specimen	Linear variable differential transformer-based measurement, accuracy limited to ~10%
Thermal Conductivity	Multiple Thermocouple	100-2000°C, ~2-8% accuracy
	Hot Wire Needle Probe	100-1800°C, ~2% accuracy

measured with ultrasound sensors possessing the desired accuracies and resolutions, are shown in Table 1[3]. Similar measurement parameters exist for structural material tests.

Table 2 lists selected instrumentation available for irradiation tests in international MTRs [4]; these instruments could potentially be replaced by ultrasound-based sensors. Many of the sensors used in foreign MTRs often require enhancement before they can be successfully deployed in the higher flux, harsher test conditions typical of U.S. MTRs. If enhanced, these sensors can provide insights into temperature, thermal conductivity, and crack growth. However, in general, the spatial resolution available with these sensors is limited both because of the limited size of the irradiation test and the desire to minimize the impact of the sensor on test results. In addition, existing and near-term sensor technologies do not provide any proven capability for detecting changes in fuel microstructure or constituent migration in high-temperature (potentially in excess of 2000°C), high-fluence radiation environments.

For decades, ultrasonic instruments have non-destructively measured various process control parameters successfully. They have been used, for example, to characterize materials and detect flaws. If ultrasonic transducers could be used to make these measurements and survive irradiation test conditions, all of the parameters listed in Tables 1 and 2 could be monitored ultrasonically, offering the potential for higher fidelity data than possible with currently available sensors. For high-accuracy measurements, most of these applications will likely require the high-frequency operational capabilities of piezoelectric transducers, but some measurements can be made with magnetostrictive transducers as well. For example, post-irradiation examinations (PIEs) show that fuel microstructure parameters, such as

porosity and grain size, can be correlated to ultrasonic velocity [5] (and, therefore, detected by ultrasonic transducers). As noted by Villard [6], frequency requirements for such measurements are typically restricted to greater than 10 MHz. However, lower frequencies can be used for some applications, such as ultrasonic thermometry, where frequency requirements may be 100–150 kHz or lower (such as magnetostrictive transducer-based ultrasonic thermometry).

### Ultrasonic Transducers

To generate and receive ultrasonic pulses and signals, two of the most commonly used technologies are piezoelectric and magnetostrictive transducers. Ultrasonic measurements using piezoelectric transducers have been demonstrated over a wide frequency range—from kHz to GHz. Since most nondestructive evaluation, materials characterization, and process monitoring are performed in the range from 1–20 MHz, piezoelectric transducers are ideal. The current capabilities of magnetostrictive transducers are typically limited to operation at frequencies up to about 200 kHz, although recent research suggests that higher frequencies may be possible for small magnetostrictive transducers [7]. However, mechanical coupling, as well as enhanced guided-wave mode generation, makes magnetostrictive transduction ideal for low-frequency measurements, such as ultrasonic thermometry [10]. Therefore, radiation-tolerant sensors that use piezoelectric or magnetostrictive materials are being considered as candidates for instrumentation in U.S. MTR testing. The PSU-led MITR irradiation test is unique because it will include both piezoelectric and magnetostrictive transducers and because it will involve higher fluences for the candidate materials.

### Piezoelectric Transducers

The piezoelectric transducer design proposed for this irradiation test was chosen based on research by Parks and Tittmann [11] and information from early ultrasonic sensors developed at the Hanford Engineering Development Laboratory [12] for under-sodium viewing. They share similar constraints with respect to thermal and neutron radiation tolerance. These transducers rely on pressure for coupling the piezoelectric element to the waveguide. Electrical contact with the piezoelectric element is achieved through application of pressure. A backing layer behind the piezoelectric sensor provides damping and prevents excessive ringing of the transducer. A schematic of the piezoelectric transducer design is shown in Figure 1.

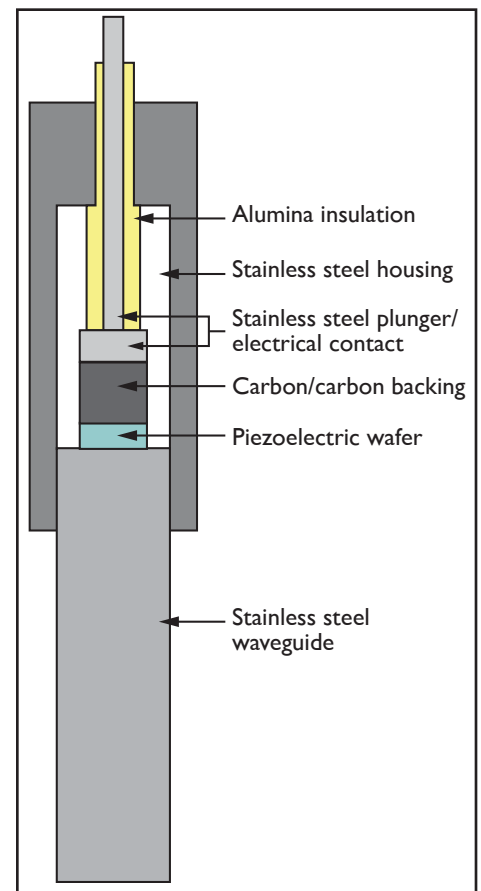


**Figure 1.** Schematic of piezoelectric transducer design.

The irradiation volume available in this test limits the number of piezoelectric transducer materials that can be included. Piezoelectric transducer materials were selected based on prior irradiation test results, anticipated radiation tolerance, transition temperature, and ease of incorporation into sensor designs. The piezoelectric materials selected for inclusion in this test are described below.

### 1) Bismuth Titanate

Suggested literature review and subsequent analysis suggested bismuth titanate ( $\text{Bi}_3\text{TiO}_9$ ) as the most promising material extensively tested to date [13]. However, this material lost roughly 60% of its one-way piezoelectric response at a fast neutron fluence of  $10^{20}$  n/cm<sup>2</sup>, suggesting that it is not an ideal candidate. The decrease in the signal response is in agreement with the statements provided in Reference [14], which indicates that disordered Ti-O-Ti bridges of highly covalent character form in titanates when subjected to the effects of neutron radiation, causing damage to the crystal structure and degradation of the piezoelectric properties of the material. Given that this material has shown the greatest promise to-date, it has been selected as a baseline for comparison in this irradiation test.

### 2) Aluminum Nitride

Aluminum nitride (AlN) is a relatively new, bulk single-crystal material. In fact, the work of Parks and Tittmann with this material is the first of its sort. In the past, thin film AlN has been shown to be unaffected by gamma irradiation up to 18.7 MGy [15] and temperatures of 1000°C. [16],[17]. Moreover, this material has been explicitly cited in numerous independent studies as a highly radiation-tolerant ceramic [14]. This behavior is thought to be at least partially due to its wurtzite crystal structure [11]. Further, tests of bulk, single-crystal AlN in a Training, Research, Isotopes, General Atomics (TRIGA) nuclear reactor core showed

this material to be completely unaffected by fast and thermal neutron fluences of  $1.85 \times 10^{18}$  n/cm<sup>2</sup> and  $5.8 \times 10^{18}$  n/cm<sup>2</sup>, respectively, and a gamma dose of 26.8 MGy [11]. This work, along with research by Yano [18] and Ito [19], indicates that the  $^{14}\text{N}(n,p)^{14}\text{C}$  is not of concern and AlN is an excellent candidate material.

### 3) Zinc Oxide

Zinc oxide, like AlN, has a wurtzite crystal structure and has been cited as a highly radiation-tolerant material [14]. The evaluated nuclear data files (ENDF) [20] do not show any detrimental nuclear cross sections and this material possesses a high transition temperature and moderate piezoelectric coupling (a measure of its efficiency in converting electrical energy to mechanical energy).

### Magnetostrictive Transducers

The magnetostrictive transducer design proposed for this test was selected based on research by Lynnworth [21] and Daw [22]. The transducer designs consist of a small driving/sensing coil, a biasing magnet (which recent results indicate is not necessary in all cases), and a magnetostrictive waveguide. The ultrasonic signal is generated when a high-frequency alternating current pulse is driven through the coil. The induced magnetic field causes magnetic domains within the material to oscillate. The domains are pre-biased by the magnet to maximize the response. Received echoes of the oscillations are sensed through the coil via the reciprocal effect. A schematic of the magnetostrictive transducer design is shown in Figure 2.

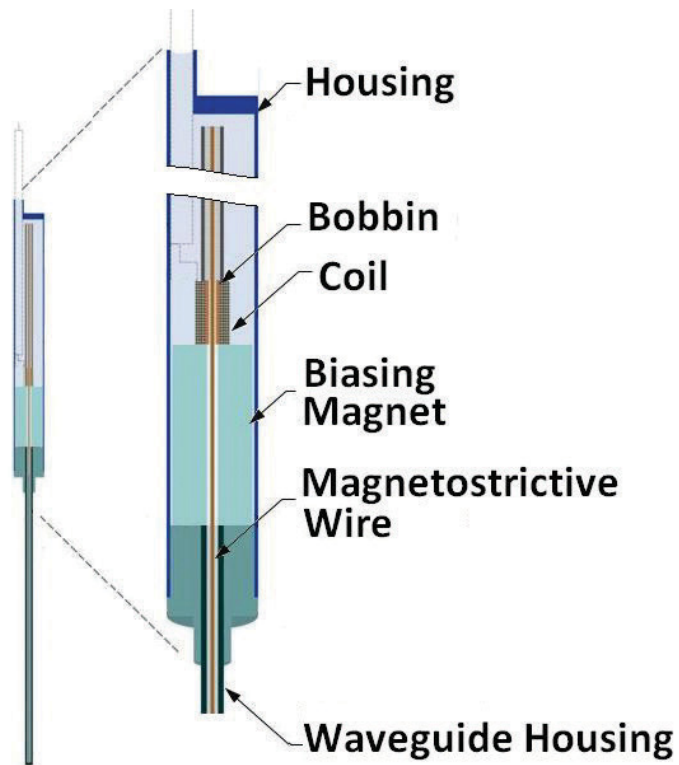


**Figure 2.** Schematic of magnetostrictive transducer design.

The magnetostrictive transducer materials were selected based on previous use in radiation environments, amounts of neutron sensitive materials, Curie temperature, and saturation magnetostriction.

### 1) Remendur

Remendur has the most history of use in nuclear applications of all magnetostrictive alloys, having been used previously for short-duration thermometry applications. Remendur is an alloy composed of approximately 49% iron, 49% cobalt, and 2% vanadium. This alloy has a high Curie temperature (950°C) and relatively high saturation magnetostriction (~70 mstrains). Because of its cobalt content, Remendur is not considered an ideal choice (due to concerns about the production of Cobalt-60 during irradiation). However, its successful prior use warrants inclusion.

### 2) Galfenol [23]

Galfenol is a relatively new alloy of iron and (approximately 13%) gallium. Galfenol is a member of the so-called giant magnetostrictive alloys and has a very large saturation magnetostriction (100–400 mstrains). It also has an appropriately high Curie temperature (700°C). Neither of its constituent elements reacts strongly with neutron radiation. These factors suggest that Galfenol is the most appealing magnetostrictive material candidate.

### 3) Arnokrome [24]-[26]

Arnold Magnetics produces several magnetostrictive alloys. The most promising alloys, Arnokrome 4, and Arnokrome 5, are included in this study. However, initial testing of transducers constructed with these alloys indicates that the signal decreases with increasing temperatures to the extent that the signal becomes indistinguishably small at the temperatures expected in the irradiation test. Therefore, these Arnokrome alloys will only be included as loose samples, which will be tested during PIE (see Section IV-C).

## Experiment Design

### MITR

The MITR is a tank-type research reactor [27] operating at atmospheric pressure. It began operation in 1958 and its current license, issued in November 2012, authorizes steady-state 6-MW operation. The reactor comprises two tanks: an inner tank for light water coolant/moderator and an outer tank for the heavy-water reflector. A graphite reflector surrounds the heavy water tank. The MITR is equipped with a wide variety of sample irradiation facilities, with fast and thermal neutron fluxes up to  $3.6 \times 10^{13}$  and  $1.2 \times 10^{14}$  n/cm<sup>2</sup>·s, respectively. The test position within the MITR core is shown in Figure 3.

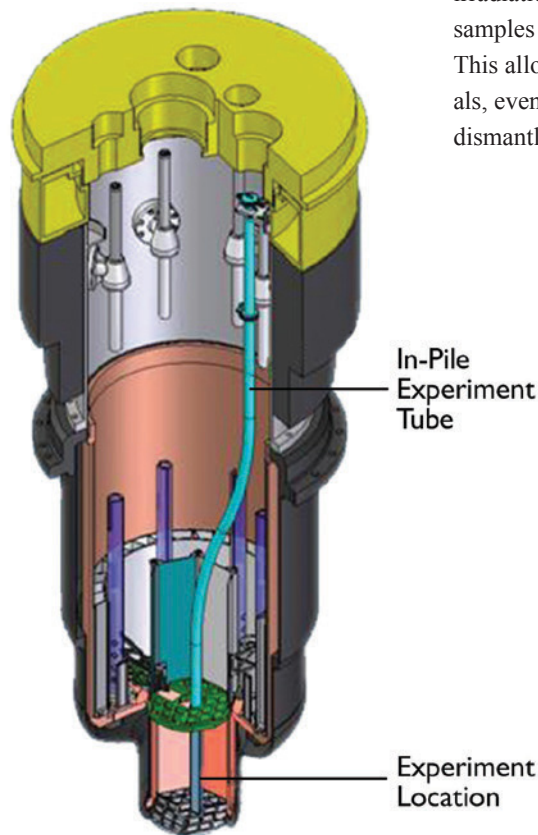


**Figure 3.** Cutaway view of the MITR reactor, showing the locations of the in-pile experiment tube and the experiment location within the core.

### Capsule

The MITR configuration restricts the test capsule to a cylinder 42 mm in diameter and 152.4 mm in length (see Figure 4). The capsule design for this test uses structural graphite as a holder material. Graphite is an ideal material because it has low density (for reduced gamma heating). In addition, graphite is thermally conductive (to produce a uniform predictable temperature), exhibits low neutron activation, and can be used at very high temperatures. During irradiation, the graphite holds the test specimens in place, while also efficiently conducting heat generated to the coolant.

Based on estimated space requirements, four piezoelectric transducers and two magnetostrictive transducers were included for this irradiation. Additionally, loose “tuck in” samples of each test material were included. This allows for PIE of all transducer materials, even for those transducers that cannot be dismantled after irradiation.

An array of sensors are included in the irradiation capsule to ensure that test conditions are well characterized. Two type-K thermocouples and a selection of melt wires are used to monitor temperatures online and verify maximum test temperature. Thermal neutron flux is monitored online using a vanadium emitter self-powered neutron detector, and thermal and fast neutron flux are verified using flux wires. Gamma flux is monitored online using a platinum emitter self-powered gamma detector.

**Irradiation Conditions**

The capsule was inserted in the MITR and the irradiation was initiated in February 2014. Transducer temperature is adjusted by controlling the composition of the gas in the gap between the capsule and the experiment guide tube. The test temperature is approximately 450°C. It was planned that the test would exceed fast neutron fluences of prior piezoelectric transducer irradiations (e.g., greater than  $1 \times 10^{21}$  n/cm<sup>2</sup> [28]). Given a fast neutron flux of  $3.6 \times 10^{13}$  n/cm<sup>2</sup>·s, the capsule would be irradiated for at least 310 days. In order to observe rapid changes at relatively low fluences, the test was initiated

with the reactor slowly ascending to power. The identified irradiation position and flux conditions at the MITR are summarized in Table 3.

<b>Table 3. Expected irradiation test conditions.</b>	
MITR In-Core Experimental Facility	
Capsule dimensions	42 mm OD x 152.4 mm long
Thermal flux	$3.6 \times 10^{13}$ n/cm <sup>2</sup> sec
Fast flux (>1 MeV)	$1.2 \times 10^{14}$ n/cm <sup>2</sup> sec
Gamma dose rate	$1 \times 10^9$ R/hr
Temperature	400–500°C
Testing pPeriod	310 effective full-power days requiring approximately 540 calendar days (18 months)

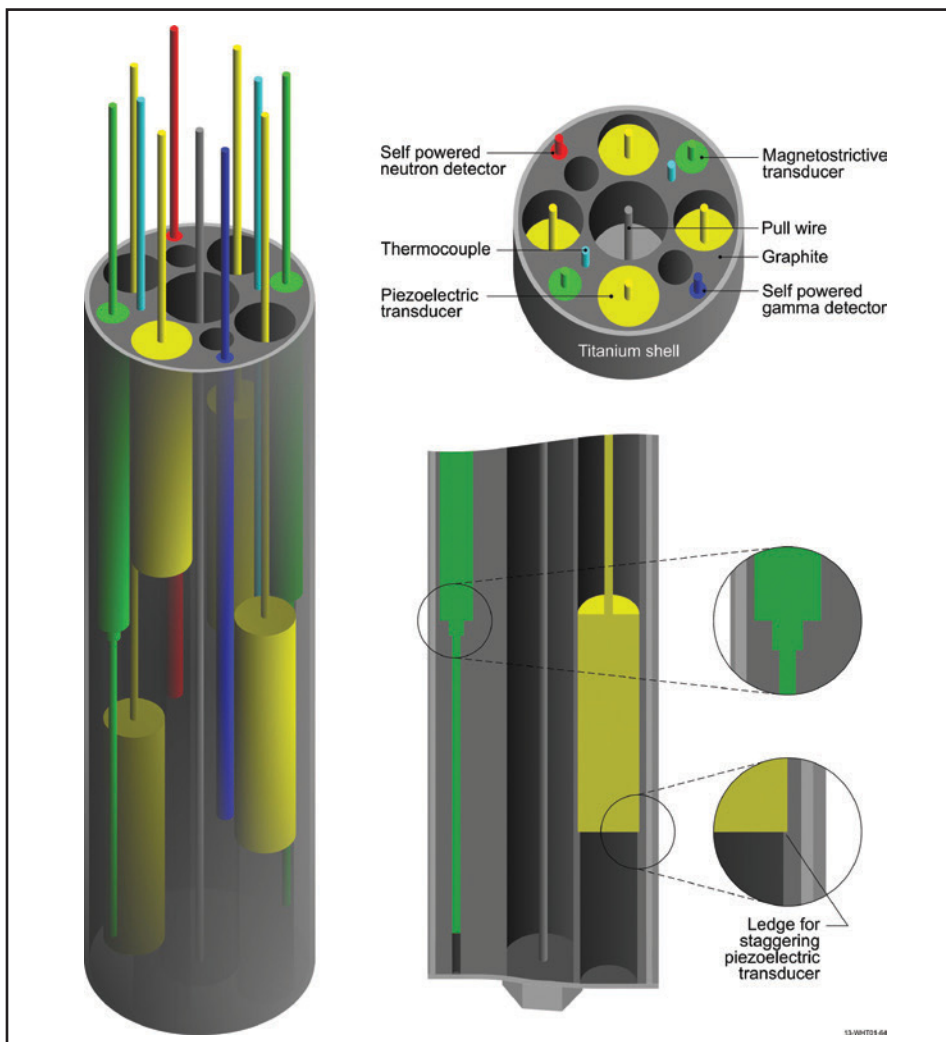


**Figure 4.** Schematic of test capsule design, showing positions of test transducers and sensors.

**Laboratory Tests**

Laboratory tests are being used to separate the effects of elevated temperatures from irradiation effects on the transducers. These tests also help optimize the transducer designs for thermal cycling and for high-temperature, long-duration operation. Temperature cycling tests are first performed to identify heating rate limitations (i.e., thermal shock) of each sample material. The second tests evaluate the maximum operating temperature of each transducer. Finally, a long-duration test that closely matches the temperatures and duration of the in-reactor test provides insights related to temperature. This test begins with a slow ramp up to temperature, matching the initial power-up temperatures in the reactor. The test is performed at anticipated steady-state in-core temperature, approximately 450°C, with intermittent cool downs simulating scheduled reactor shutdowns. The test will last for up to 10 months (the anticipated in-pile test duration at power).

### *Post-Irradiation Examination*

Irradiation effects on candidate materials will be quantified through PIE, and results will be compared with pre-irradiation values. A description of the planned PIEs follows.

First, researchers will complete simple pulse-echo measurements, which reveal much information about the quality of the transducer. These measurements can be taken without disassembling the transducer. They can be made either in-pile (after reactor shutdown) or after removal from the reactor. The pulse-echo measurement is used to measure signal-to-noise ratio (indicating sensitivity of the transducer), resonance frequency, bandwidth, and the quality factor (a measure of the intrinsic damping of the crystal). These factors are used as a go/no go test for sensor performance and are most important in ascertaining transducer performance.

Impedance measurements can be used to calculate loss tangent, which is related to dielectric property changes. It also reveals resonance frequency, stiffness, and dielectric constant. This is important in determining loss mechanisms. Like pulse-echo measurements, this measurement can be taken without disassembling the transducer.

Hysteresis measurements show remnant polarization, which is necessary for transduction in ferroelectrics and the degradation mechanism, such as metamictization versus antiferroelectric tendencies. This measurement can be made without disassembling the transducer.

Density data are needed to determine material properties from the pulse-echo and impedance measurements. During temperature testing, it is common to see variations in densities of many piezoelectric materials, and it is important to characterize these changes. The sensor material must be removed from the transducer assembly, measured, and weighed for this measurement.

The d33 parameter is a material constant important to piezoelectric transducer signal amplitude. This parameter is most significantly affected during neutron testing in most materials; thus, it is also important to characterize observed d33 changes. It will be necessary to remove the sensor material from the transducer in order to measure this material property with a d33 meter.

Some materials change color during irradiation, which can indicate absorption of oxygen and other contaminants. Optical examination requires that the sensor material be removed from the assembly and photographed with a high-resolution camera.

Scanning electron microscopy (SEM) is important to characterizing the grain structure of the sensor and changes that occur during irradiation. SEM examinations may provide insights about the damage mechanisms and how polar domains change during irradiation. SEM examples also require that samples be removed from the transducer assembly.

### **Conclusion**

---

Ultrasonic measurements have a long and successful history of use in materials characterization, measurement of various physical parameters used for process control, and nondestructive examination. To develop advanced in-core sensors based on ultrasonic technologies, a fundamental understanding of the behavior of ultrasonic transducer materials in high-radiation environments is needed. While a number of irradiation studies of ultrasonic transducers has been performed, a direct comparison of these studies is difficult due to differences in the included materials and test conditions. In addition, tests to-date have generally been performed at lower flux/fluences than what might be required for U.S. MTRs.

A PSU-led effort to perform an ultrasound transducer irradiation is being funded by the ATR NSUF for irradiation in MITR. The test is unique because it is the first irradiation to include both piezoelectric and magnetostrictive transducers and because it will expose transducers to higher fluences than prior irradiations. This test is an instrumented lead test; real-time signals will be received from the transducers. Such a test enables accurate measurement of the performance and degradation of candidate piezoelectric and magnetostrictive transducer materials under irradiation and, ideally, identification of an appropriate ultrasonic transducer material to enable development of new ultrasonic sensors capable of monitoring many physical parameters in-core.

### **Acknowledgements**

---

Work supported by the U.S. DOE-NE, Science, and Technology, under DOE-NE Idaho Operations Office Contract DE-AC07-05ID14517.

## References

1. D. Ensminger and L.J. Bond, *Ultrasonics; Fundamentals, Technologies, and Applications*, CRC Press, 2012.
2. L.C. Lynnworth, "Ultrasonic Measurements for Process Control: Theory, Techniques, and Applications," Academic Press, 1989.
3. J. Rempe, H. MacLean, R. Schley, D. Hurley, J. Daw, S. Taylor, J. Smith, J. Svoboda, D. Kotter, D. Knudson, S.C. Wilkins, M. Guers, L. Bond, L. Ott, J. McDuffee, E. Parma, and G. Rochau, "New In-Pile Instrumentation to Support Fuel Cycle Research and Development," FCRD-FUEL-2011-000033 (also issued as INL/EXT-10-19149), January 2011.
4. B.G. Kim, J.L. Rempe, J-F Villard, and S. Solstad, "Review of Instrumentation for Irradiation Testing of Fuels and Materials," *Nuclear Technology*, 176, p 155-187.
5. K. Phani et. al, "Estimation of Elastic Properties of Nuclear Fuel Material Using Longitudinal Ultrasonic Velocity - A New Approach," *J. Nucl. Mat.*, 366, 129-136 (2007).
6. J.F. Villard et. al., "Acoustic Sensor for In-Pile Fuel Rod Fission Gas Release Measurement," *IEEE Transactions on Nuclear Science*, 58, 2011, 151-155 (2011).
7. J.L. Rempe, D.L. Knudson, K.G. Condie, and S.C. Wilkins, "Thermocouples for High-Temperature In-Pile Testing," *Nuclear Technology*, 156, 320-331 (December 2006).
8. J.E. Daw, J.L. Rempe, and J.C. Crepeau, "Update On Ultrasonic Thermometry Development At Idaho National Laboratory," *8th International Topical Meeting on Nuclear Plant Instrumentation, Control, and Human Machine Interface Technologies* (NPIC&HMIT 2012), San Diego, CA, July 22-26, 2012.
9. J.Daw, J.Rempe, J. Palmer, P. Ramuhalli, R. Montgomery, H-T. Chien, B. Tittmann, B. Reinhardt, and G. Kohse, "Irradiation Testing of Ultrasonic Transducers," *2013 Conference on Advancements in Nuclear Instrumentation, Measurements Methods* (ANIMMA 2013), Marseilles, France, June 23-27, 2013,.
10. N. Gopalsami, A.C. Raptis, "Acoustic Velocity and Attenuation Measurements in Thin Rods with Application to Temperature Profiling in Coal Gasification Systems," *IEEE Transactions on Sonics and Ultrasonics*, SU-31, 32-39 (1984).
11. D.A. Parks, and B.R. Tittmann. "Ultrasonic NDE in a Reactor Core," *Presented at Review of Progress in Quantitative Nondestructive Evaluation*, Burlington, VT, July 17-22, 2011.
12. R.N. Ord and R.W. Smith, "Ultrasonic Under-Sodium Viewing System Development for the FFTF," HEDL-SA-335. Westinghouse Hanford Co., Richland, Washington (1972).
13. Y. P. Meleshko, S.G. Karpechko, G.K. Leont'ev, V.I. Nalivaev, A.D. Nikiforov, and V.M. Smirnov, "Radiation Resistance of the Piezoelectric Ceramics TsTS-21 and TNV-I," Translated from *Atomnaya Energiya*, 50-52 (1986).
14. K. Trachenko, "Understanding resistance to amorphization by radiation damage," *Journal of Physics: Condensed Matter*, 16 (49), R1491-R1515 (2004).
15. R. Kazys, V. Voleisis, R. Sliteris, B. Voleisiene, L. Mazeika, and H. Abderahim, "Research and Development of Radiation Resistant Ultrasonic Sensors for Quasi-Image Forming Systems in a Liquid Lead-Bismuth," *Ultrasonics (Ultrasound)*, 62 (3), 7-15 (2006).
16. N.D. Patel and P.S. Nicholson, "High Frequency - High Temperature Ultrasonic Transducers," *NDT International*, 262-266 (1990).
17. D. Stubbs and R. Dutton , "High-Temperature Ultrasonic Sensor for in Situ Monitoring of Hot Isostatic Processing," *SPIE*, 164-172 (1996).
18. T. Yano, K. Inokuchi, M. Shikama, and J. Ukai, "Neutron irradiation effects on isotope tailored aluminum nitride ceramics by a fast reactor up to  $2 \cdot 10^{26}$  n/m<sup>2</sup>," *Journal of Nuclear Materials*, 1471-1475 (2004).
19. Y. Ito et al., "Radiation Damage of Materials Due to High Energy Ion Irradiation," *Nuclear Instruments and Methods in Physics Research*, 530 (2002).
20. Evaluated Nuclear Data File (ENDF) Database Version of August 13, 2013, <http://www-nds.iaea.org/exfor/endl.htm>.
21. L.C. Lynnworth, E.H. Carnevale, M.S. McDonough, and S.S. Fam, "Ultrasonic Thermometry for Nuclear Reactors," *IEEE Transactions on Nuclear Science*, NS-16, 184-187 (1968).
22. J. Daw, J. Rempe, S. Taylor, J. Crepeau, and S.C. Wilkins, "Ultrasonic Thermometry for In-Pile Temperature Detection," *Proceedings of NPIC&HMIT 2010* (2010).
23. "What is Galfenol?," Etrema Products, Inc., <http://www.etrema-usa.com/core/galfenol/>, accessed 08/09/2012.

24. Arnokrome-3 Datasheet, Rev. 01-11-11, [www.arnoldmagnetics.com/WorkArea/DownloadAsset.aspx?id=5262](http://www.arnoldmagnetics.com/WorkArea/DownloadAsset.aspx?id=5262), 25] Arnokrome-4 Specification, Rev. 1/11/11, [www.arnoldmagnetics.com/WorkArea/DownloadAsset.aspx?id=5263](http://www.arnoldmagnetics.com/WorkArea/DownloadAsset.aspx?id=5263), accessed 08/09/2012.
26. Arnokrome-5 Specification, Rev. 2/24/11, [www.arnoldmagnetics.com/WorkArea/DownloadAsset.aspx?id=5328](http://www.arnoldmagnetics.com/WorkArea/DownloadAsset.aspx?id=5328), accessed 08/09/2012.
27. *MITR Users Guide*, Rev. 3, July 2012, Massachusetts Institute of Technology (2012).
28. F. Augereau, J-Y. Ferrandis, J-F. Villard, D. Fourmentel, M. Dierckx, and J. Wagemans, "Effect of intense neutron dose radiation on piezoceramics," *Acoustics'08*, Paris(2008).



**Joshua Daw** (B.S., 2006, Mechanical Engineering, Idaho State University; M.S., 2008, University of Idaho) is a Research Engineer at INL where he leads ultrasound-based in-pile instrumentation development and deployment efforts. In 2014, he was awarded the Laboratory Director's Achievement Award for Exceptional Engineering Achievement for his leadership in this area. He is currently pursuing his Ph.D. in Mechanical Engineering at the University of Idaho. He completed an assignment at the Norwegian Halden Reactor Project where he led efforts on an instrumented fuel assembly test investigating fission gas release. Mr. Daw has received several recognition awards for his outstanding research in high-temperature in-pile instrumentation, including being named the 1st place winner in the Nuclear Fuels Open Competition of the 2013 Innovations in Fuel Cycle Research Awards, and the 2nd place winner in the Nuclear Fuels Open Competition of the 2012 Innovations in Fuel Cycle Research Award. Additionally, he was named the Spring 2008 University of Idaho, College of Engineering Outstanding Masters Student, and attended the 11th Annual National Academies Keck Futures Initiative conference. He has authored or co-authored over 30 peer reviewed archival journal publications/peer-reviewed conference papers and is the inventor/co-inventor for three invention disclosures/patents on high-temperature testing and in-pile instrumentation.



**Joy Rempe** (B.S., 1981, Nuclear Engineering, University of Missouri-Rolla; M.S., 1983 and PhD., 1986; Massachusetts Institute of Technology) is a Laboratory Fellow and Group Leader at INL where she leads in-pile instrumentation development efforts for INL's ATR NSUF. She also provides consulting assistance to vendors, utilities, and regulators on severe accident issues. With over 28 years of research experience, Dr. Rempe has authored or co-authored over 50 archival peer-reviewed journal publications and over 90 peer-reviewed conference papers on reactor safety, severe accident phenomena, high-temperature testing, and in-pile instrumentation. She is an inventor/co-inventor on five patents (pending). In 2005, Dr. Rempe was elected a Fellow in the American Nuclear Society; between 2009 and 2012, she served on the American Nuclear Society Board of Directors; in 2010, she was appointed to the U.S. Nuclear Regularly Commission's Advisory Committee on Reactor Safeguards; in 2012, she received the U.S. Department of Energy Secretarial Honors Award; and in 2014, she was appointed by Energy Secretary Moniz to the U.S. Department of Energy's Nuclear Energy Research Advisory Committee.



**Joe Palmer** (B.S., 1987, Mechanical Engineering, Brigham Young University; M.S., 1988, Mechanical Engineering, Brigham Young University) is a mechanical design engineer at INL, where he designs temperature-controlled experiments and experiments for the Hydraulic Shuttle Irradiation System. Mr. Palmer has 25 years of extensive experience in reactor experiment design, chemical process equipment design, dynamic systems modeling, piping systems, finite element stress, and thermal analysis. He also holds a Professional Engineering license in Idaho.



**Bernhard R. Tittmann** received his Ph.D. from the University of California at Los Angeles as a Howard Hughes Fellow. He joined the North American Science Center in 1966. Since then, he has held the position of Schell Professor of Engineering at Pennsylvania State University. He is best known for his contributions in physical acoustics to materials characterization, which first led to the study of superconductivity, then rock mechanics, surface acoustic wave devices, non-destructive examination sensors for process monitoring and control of composites, sensors for health monitoring of pressure vessels and more recently acoustic microscopy of biological cells and tissue. Dr. Tittmann is a Fellow of the Acoustical Society of America and the American Society of Materials International. He was a Senior Fulbright Scholar, IEEE-UFFC Distinguished Lecturer, and winner of the PSU Engineering Society Outstanding Research Award.



**Brian Reinhardt** is a graduate student at the PSU and cofounder of Lasers for Innovative Solutions, LLC. At PSU Brian has worked on projects related to nonlinear ultrasonic wave propagation in fatigued wavy slip metals to sensor design for nuclear reactor environments. At Lasers for Innovative Solutions, Brian is responsible for leading commercialization efforts of a new tomography technique based on laser ablation.



**Gordon Kohse**, received his Ph.D. in Nuclear Engineering from MIT and a B.Sc. in Chemical Engineering from the University of Calgary. Since since 1983, has participated in and directed all phases of nuclear engineering research at MITR, including experiment design, construction, operation, and data analysis and reporting in the areas of light water power reactor coolant chemistry and coolant/materials interaction. This research has resulted in development and use of seven in-core facilities at the MITR-II 5-MW research reactor, many of which have unique capabilities. His responsibilities at the MIT reactor laboratory also include supervision of thesis students at the Ph.D., masters, and undergraduate levels. For several years, Dr. Kohse has collaborated with INL staff members as part of MIT's partnership in ATR NSUF.



**Pradeep Ramuhalli** (Ph.D., 2002, Electrical Engineering, Iowa State University) is a senior research scientist at PNNL. Prior to joining PNNL, he was an assistant professor in the Department of Electrical and Computer Engineering at Michigan State University, East Lansing. Pradeep Ramuhalli's research expertise is in resilience and reliability. His research has spanned multiple areas, and includes sensors, integrated system health monitoring and prognostics, ultrasonic and electromagnetic inverse problems, multisensor data fusion, numerical methods, and image/signal processing. Currently, he is developing and evaluating ultrasonic and electromagnetic sensors and algorithms for continuous online monitoring of stressors and systems for condition estimation, prognostics algorithms to assess remaining useful life, and methodologies to assure resilience of degraded systems. Applications of his research are in life extension of legacy nuclear power plants, safe and economic operation of next generation nuclear power plants, cyber-security, safeguards, and national security.



**Hual-Te Chien** (Ph.D., 1991, Aerospace Engineering and Engineering Mechanics, University of Cincinnati) joined the Energy Technology Division of Argonne National Laboratory. Dr. Chien is the section manager of Sensors and Instrumentation of the Nuclear Engineering Division. He has 26 years of experience in the area of sensor and instrumentation, nondestructive evaluation and testing, acoustics and vibration, data and image processing, experimental stress analysis, and smart/intelligent materials and structures development. He has developed photoacoustic, microwave, millimeter, and Terahertz spectroscopy techniques for remote sensing and monitoring of chemicals and explosives. Currently, Dr. Chien is developing an ultrasonic waveguide transducer technique for under-sodium viewing of sodium-cooled fast reactors. Dr. Chien shared a 1994 and 2011 R&D 100 Awards for two inventions and was also awarded an Argonne's Pacesetter Award for excellence in achievement and performance in 1997. He has been author or co-author of more than 60 publications and awarded nine U.S. patents.



# **In-Core Flux Sensor Evaluations at the ATR Critical Facility**

# In-Core Flux Sensor Evaluations at the ATR Critical Facility

*T. Unruh, B.M. Chase, J.L. Rempe, D.W. Nigg (INL), G. Imel, J.T. Harris, T. Sherman (ISU), J-F. Villard (CEA, DEN, DER, Instrumentation, Sensors and Dosimetry Laboratory, Cadarache, France)*

As part of an Idaho State University (ISU)-led Advanced Test Reactor National Scientific User Facility (ATR NSUF) collaborative project that includes Idaho National Laboratory (INL) and the French Alternative Energies and Atomic Energy Commission (CEA), flux detector evaluations were completed to compare the accuracy, response time, and long-duration performance of several flux detectors. Special fixturing, developed by INL, allows real-time flux detectors to be inserted into various Advanced Test Reactor Critical (ATRC) core positions and to perform lobe-power measurements, axial-flux profile measurements, and detector cross calibrations. Detectors evaluated in this program included miniature fission chambers, specialized self-powered neutron detectors (SPNDs), and specially developed commercial SPNDs. Result from this

program provide important insights related to flux-detector accuracy and resolution for subsequent ATR and CEA experiments and yield new flux data required for bench-marking models in the ATR Validation & Verification Upgrade Initiative.

## Introduction

ATR and its associated low-power nuclear mock-up, ATRC, are premier facilities for scientific investigation of nuclear fuel and materials [1]. Although unsurpassed with respect to irradiation testing capabilities, these facilities have not investigated instrumentation in irradiations to obtain direct, real-time measurements of thermal-neutron flux and fission reaction rates for irradiation capsules. Recent technological developments offer the possibility for such direct measurements without resorting to complicated

correction factors. In addition, it is possible to directly measure minor actinide fission reaction rates and to provide time-dependent monitoring of the fission reaction rate or fast/thermal flux ratio during transient testing.

An ISU-led ATR NSUF collaborative project that includes INL and CEA is evaluating real-time, state-of-the-art, in-pile, flux-detection sensors. The primary objective of this effort was to investigate the feasibility of using various types of neutron sensors to provide real-time measurement of the fission reaction rate in ATRC. A second objective was to provide neutron spectrum and flux distribution information using activation spectrometry, both as an aid in interpreting data from the real-time sensors under evaluation and for use in the validation of advanced physics modeling codes to support the ATR Life Extension Project Program. Detailed activation measurements were made to provide additional calibration data for the real-time sensors of interest, as well as high-quality benchmark neutronics data that will be useful for the Life-Extension Project Methods and Validation & Verification Upgrade Project that is upgrading reactor physics codes. Calculations were performed to assess the performance of, and reduce uncertainties in, flux detection sensors and to compare data obtained from these sensors with data from existing integral methods employed at ATRC [2].



**Figure 1.** CEA/INL/ISU researchers performing miniature fission chamber evaluations in ATRC.

A new capability for evaluating flux detectors, which includes specialized instrument positioning hardware and associated software, was developed to facilitate these evaluations at the INL ATRC. This project initially focused on detectors readily available to the research team such as activation detectors (foils and wires) from the existing, well-characterized INL inventory. As part



Figure 2. ATRC layout.

of an on going ATR NSUF international cooperation, CEA provided miniature fission chambers, one for detecting fast neutron flux and two for detecting thermal-neutron flux. CEA researchers visited ATRC and instructed INL and ISU researchers on the use of CEA’s specialized fission chambers. Evaluations also included specialized commercial SPNDs that were initially used at the Transient Reactor Experiment and Test Facility and Neutron Radiography Reactor at INL. The project also evaluated data obtained from rhodium SPNDs, which were designed and built at the Argentinean National Energy Commission (see Figure 1).

This article highlights results from this effort, including descriptions of the specialized fixtures developed to allow various types of detectors to be evaluated. More detailed information about this project may be found in [3] and [4].

## ATR/ATRC Description

The ATRC is a low-power nuclear mock-up of the ATR core that allows advanced characterization of the expected changes in core reactivity of a proposed ATR test. ATRC operates at a thermal power of less than 5 kW. ATRC criticality is normally attained at a power greater than 0.25 mW. This pool-type reactor (Figure 2) operates at a power level of about 600 W for the majority of tests and provides useful physics data for evaluating the following:

- Worth and calibration of control elements
- Excess reactivities and charge lifetimes
- Thermal and fast neutron distributions
- Gamma heat generation rates
- Fuel loading requirements
- Effects of inserting and removing experiments and experiment void reactivities
- Temperature and void reactivity coefficients.

The ATRC core consists of a 4 ft high (122-cm), uniform-width, vertical 40-element fuel annulus shaped in a serpentine fashion between and around nine flux trap areas located in a 3 × 3 array (see Figure 3).

The reactivity of the core is controlled primarily by eight pairs of rotating outer shim control cylinders that use hafnium plates as neutron absorbers. Small reactivity adjustments were performed with one of the 24 vertically withdrawn hafnium neck shim rods. In addition, rapid shutdown is accomplished with five vertically withdrawn safety rods that use cadmium as the poison material.

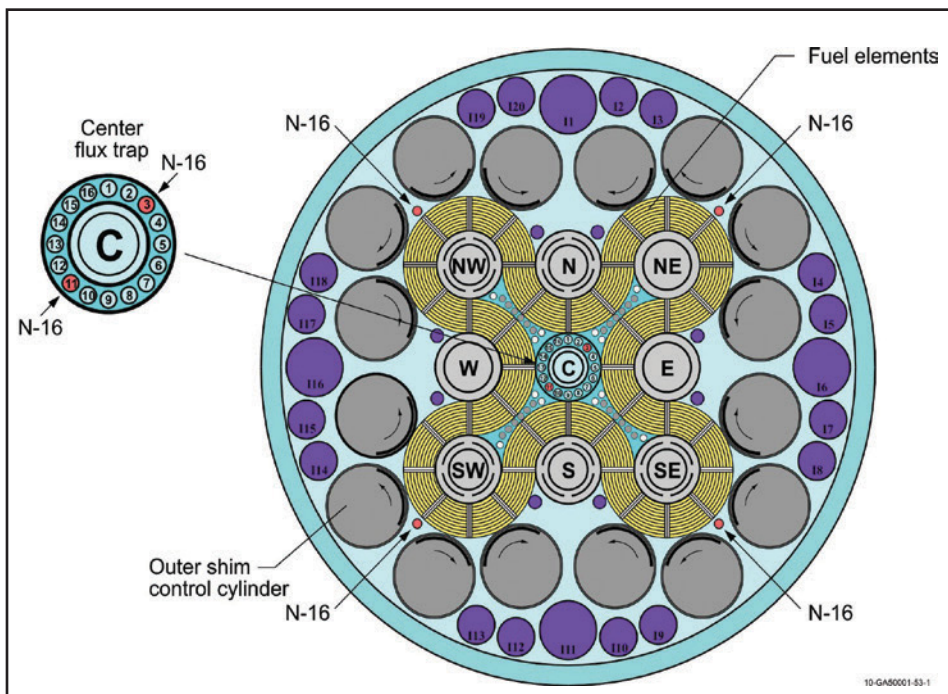


Figure 3. ATRC core configuration.

There are several design features incorporated into the ATR core and, similarly, the ATRC core, to optimize experimental capabilities. These features include the use of flux traps to provide high thermal neutron fluxes for irradiation or experiments in nine regions; incorporation of special control shim design to retain axial flux symmetry throughout an ATR fuel cycle; and regional power control to provide capability for power shifting between core lobes and thereby optimize neutron flux for a wide range of uses, studies, and experiments. There is no regional online power measurement in ATRC core as there is in the ATR (i.e., real-time lobe or quadrant power measurement).

In ATR, part of the real-time regional power measurement comes from the N-16 Lobe Power Calculating and Indicating System that monitors fast neutron flux by measuring the beta decay of N-16 in water. This system flows water through 10 re-entrant flow tubes, eight in the beryllium reflector and two in the center flux trap. Dummy re-entrant tubes are located in the reflector and center flux trap. During experimental evaluations, in-core sensors were inserted into these dummy N-16 tubes to allow real-time flux/power measurements.

## Detector and Measurement Equipment

Several types of neutron-activation detectors and real-time neutron detectors were evaluated in this project (see Table 1). More detailed descriptions of each type of sensor and associated test rigs developed for these evaluations at ATRC are provided.

### Activation Detectors

Test hardware with typical activation wires and foils used for activation spectrometry and flux profiling in ATRC are shown in Figure 4. Various materials with different neutron sensitivities as functions of neutron energy were used. During initial evaluations, six different sets of activation foil measurements were performed in the

ATRC northwest and southeast flux traps at the axial core mid-plane to determine detailed neutron spectral information at these locations for benchmarking purposes.

Detailed measurements of the core flux distribution were also performed, using standard ATRC flux wands placed in selected fuel elements to position flux wires at the core axial mid-plane.

Activation foils for these evaluations are listed in Table 1, grouped by the range of neutron energies to which each set of foils is sensitive. Some foils were placed inside standard cadmium-foil covers or boron-10 spectral modification shields to enhance their response in the epithermal and fast neutron ranges. Further experimental setup details related to activation foils can be found in [5] and [6].

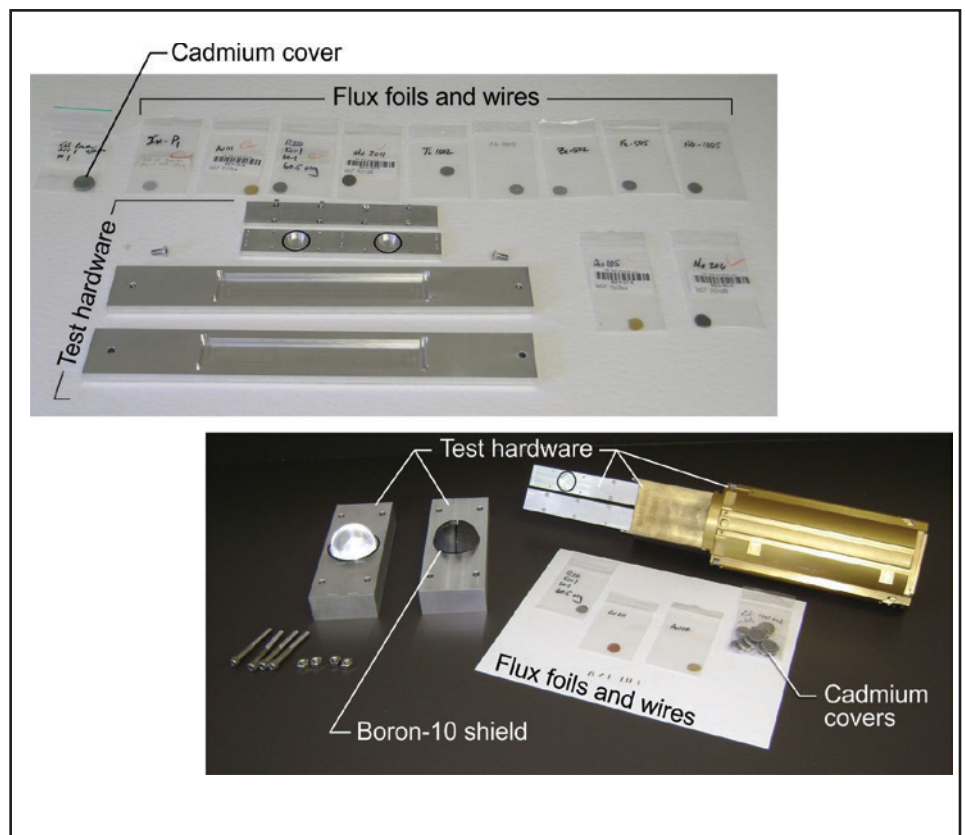


**Figure 4.** ATRC test hardware and activation foils.

<b>Table 1. Flux detectors for ISU/INL ATRC evaluations.</b>				
<b>Detector</b>	<b>Characteristics of Interest</b>			
Flux Wires	Materials			
	U <sup>235</sup> -Aluminum			
	Copper-1.55 Gold			
Flux Foils	Material	Encapsulation Material		
Thermal Neutron Detection	Gold (100 %)	None		
	Manganese-Copper (80% / 20% wt)			
Epithermal Neutron Detection	Indium (> 99%)	Cadmium (>99%) Covers		
	Gold (> 99%)			
	Tungsten (>99%)			
	Cobalt (>99%)			
	Manganese-Copper (80%/20%)			
	Copper (>99%)			
	Scandium (>99%)			
Fast Neutron Detection	Niobium (>99%)	Boron Sphere (>99%)		
	Rhodium (>99%)			
	Indium (>99%)			
	Titanium (>99%)			
	Zinc (>99%)			
	Nickel (>99%)			
	Iron (>99%)			
	Copper (>99%)			
SPNDs	Emitter	Lead Wires	Insulation	Sheath (Collector)
Hafnium (commercial) Response: Fast Sensitivity: 4.7e-21 A/nv	Hafnium (minimum 97.5% with up to 2.5% Zirconium)	Inconel 600	Alumina (99.65%)	Inconel 600
Gadolinium: Response: Fast Sensitivity: 5.0e-22 A/nv	Gadolinium (99.7%)	Inconel 600	Alumina (99.65%)	Inconel 600
Rhodium (CNEA) Response: Delayed Sensitivity:	Rhodium	Copper	Acrylic	Stainless steel-304
CEA Miniature Fission Chambers	Fissile Deposit	Anode /Fill Gas	Cathode / Fill Gas	Extension Cable
Miniature Thermal Fission Chamber	Deposit on anode: Uranium (U)-235: 98.5 % U-234: 0.063% U-236: 0.038% U-238: 1.409%	SS304L (impurities of cobalt 0.02%) Fill Gas:Argon+ 4% nitrogen	SS347(impurities of cobalt 0.2%) Fill Gas:Argon+ 4% nitrogen	Sheath: SS304L Insulation: Silicon Dioxide (>99.5%) Wires: Copper (impurities of zirconium 0.19%) Shield: Copper
Miniature Fast Fission Chamber	Deposit on cathode: U-238 : 99.964% U-235 : 0.0354% U-234 : 0.0003%	SS316L Fill Gas:Argon	Material: SS316L ID: 6.3 mm OD: 8 mm Length: 33.5 mm Fill Gas:Argon	Sheath: Polyvinyl chloride Insulation: Polyethylene (PE) Wires: Copper clad steel (CCS)

The foils were activated in the ATRC northwest large in-pile tube flux trap, which is the largest irradiation facility in ATRC. In addition, the southeast standard in-pile tube was used for activation measurements using hardware shown in Figure 5.

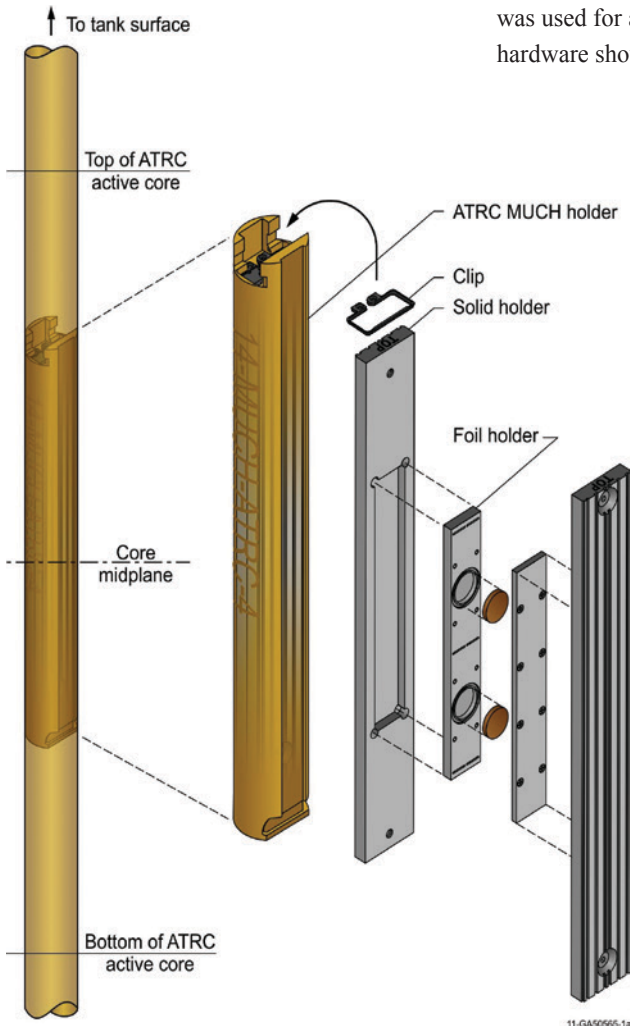


**Figure 5.** Activation detector apparatus for the ATRC southeast standard in-pile tube.



**Figure 6.** Various experimental hardware for testing in-core sensors in ATRC.

Standardization of flux data from separate reactor runs was accomplished using measured activation of standard copper/gold (1.55% Au by weight) flux wires at specific locations within the insert fittings, as well as between two fuel elements at the axial core mid-plane of four of the fuel elements surrounding the northwest flux trap.

### Real-Time Flux Detectors

As indicated in Table 1 and Figure 6, several types of detectors were evaluated. This section describes each type of detector and the specialized fixturing developed for evaluating their performance.

### Self-Powered Neutron Detectors

SPNDs have been used effectively as in-core flux monitors for decades in commercial nuclear power reactors and material test reactors world-wide [8–10]. SPNDs rely on interactions of neutrons and atomic nuclei to produce a measurable current that is proportional to the neutron flux. Compared to other in-core detectors, they feature several advantages:

- Power supply not needed
- Simple and robust structure
- Relatively small physical size
- Good stability at elevated temperature and pressure
- Able to generate reproducible linear signals
- Low burn-up rate (dependent on emitter material).

However, there are also some disadvantages associated with SPNDs:

- Limited operating range due to relatively low neutron sensitivity
- Limited to thermal flux detection
- Require background noise compensation (for some emitters)
- Delayed signal response (for some emitters).

A typical SPND consists of a coaxial cable containing an inner electrode (the emitter) surrounded by insulation and an outer electrode (the collector). In an “integral SPND,” the lead cable and detector are mated directly to each other; the insulation of both sections are identical, and the collector of the detector section is also the outer sheath of the lead cable section, as shown in Figure 7. Modular SPND assemblies are made from separate detector and lead cable sections. Typically, SPND characteristics of interest include size, material compatibility at high temperatures, sensitivity, response time, and burn-up rate.

Characteristics of SPNDs evaluated in this project are listed in Table 1. SPNDs are encased in tinted Lucite tubes to prevent any

unwanted leakage of component materials (if they are not leak tight) and to reduce unwanted noise produced when the SPND cables come in contact with metal surfaces. SPNDs were inserted into the ATRC N-16 positions using specially designed experimental guide tubes (EGTs). The EGTs are primarily fabricated from aluminum to minimize their weight. However, selected components, such as the guide tube shown in Figure 6, are made from stainless steel 304 for additional robustness. As illustrated in Figure 6, the six EGTs mechanically position detectors at a specified vertical location in the four N-16 exterior positions and two center flux trap N-16 positions. The EGTs were supported above the reactor by attachment to the reactor control bridge.

Position control and detector response are controlled and measured via specially developed software to allow all detectors to either individually or simultaneously move and measure the local neutron flux and provide a three-dimensional measurement of the overall neutron flux.

SPND response was evaluated in ATRC in several different activities. Specifically, SPND signals were compared with each other, CEA fission chambers, and neutron activation measurements.

### Miniature Fission Chambers

Fission chambers (see Figure 8), which are ion chambers with a fissionable material deposit on the inner wall, offer another method for real-time flux measurement. The fission fragments provide a very large pulse from the neutron-induced reaction and can be used in either pulse or direct-current mode. Normally, highly enriched  $^{235}\text{U}$  is used for the coating, which makes the chamber sensitive to thermal neutrons. However, other deposits (such as  $^{238}\text{U}$ ,  $^{242}\text{Pu}$ , or  $^{232}\text{Th}$ ) can be used, providing a higher neutron energy cutoff.

Characteristics of the miniature fission chambers included in the ATRC evaluations are listed in Table 1. Miniature fission chambers are used in pulse mode using current preamplifier electronics. Uranium coating masses were chosen in order to provide a high fission rate in ATRC flux (from  $10^3$  to  $10^5$  cps). To protect these fission chambers and to preclude any leakage from fission chamber components into the ATRC coolant, chambers were also placed in Lucite tubes and inserted into the ATRC N-16 positions using the EGTs.

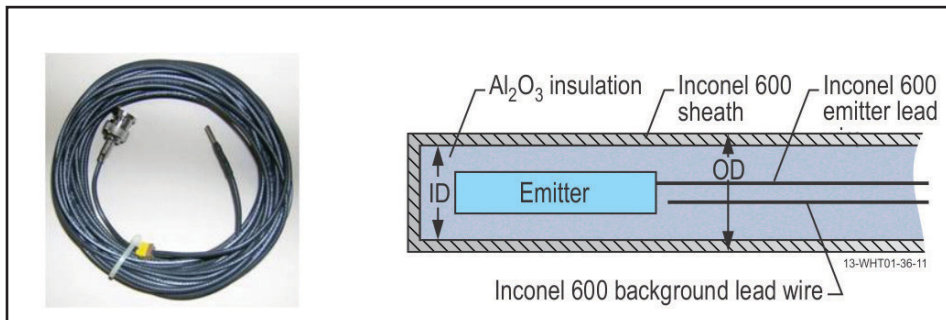


Figure 7. Representative SPND and component sketch.

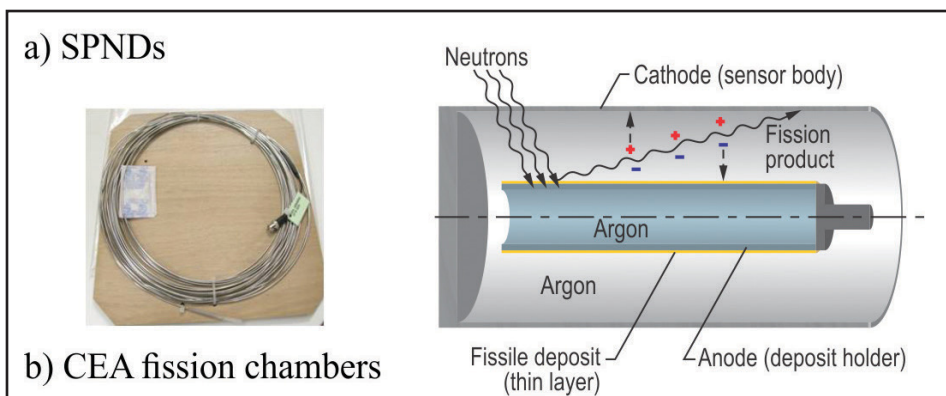


Figure 8. CEA miniature fission chambers and component sketch.

**Testing**

The experimental facilities developed for ATRC flux sensor evaluations allowed a wide range of flux sensor evaluations to be completed. Initial testing, which began in October 2010, included testing of activation foils and wires, SPNDs, and fission chambers. In 2013, a second round of flux detector evaluations was completed. As previously documented [3, 4], four specific activities were envisioned to be completed in this project. Each activity has three experimental configurations associated with the detector evaluations (see Figure 9). Summary descriptions of flux detector evaluations at ATRC are given below.-

**Flux Wires and Foils**

Several activities relied on flux wires and foils to evaluate neutron flux. Testing utilized core irradiations with U/Al and Cu/Au wires for balanced critical shim positions at 600 watts. Activation foil and wire measurements were conducted without any sensors in the N-16 position guide tubes. Twenty-minute ATRC runs, each at a power in the range of 120 watts average power per lobe (600 watts total core power), were required to complete a set of activation measurements.

The core flux distribution measurement for the balanced shim position was conducted using standard ATRC procedures, with the exception that a Cu/Au flux wire was substituted for a U/Al wire in selected fuel elements surrounding the northwest large in-pile tube. After irradiation, all foils and wires were transferred to the collocated Radiation Measurements Laboratory for detailed radiation counting to obtain the data required for final analysis [4]. Further experimental details related to activation foils testing can

be found in [9] and [10].

**Self-Powered Neutron Detectors**

SPND evaluations were completed by inserting the detectors into the six N-16 positions shown in Figure 9. Tests were completed for three different critical configurations of the outer shim cylinders: (1) balanced, (2) unbalanced toward the northwest flux trap, and (3) unbalanced away from the northwest flux trap. For each configuration, measurements were obtained for at least four intermediate power levels between 1 mW and 600 W, as shown in Figure 10. At 600 W, axial flux measurements were obtained by varying detector positions using the EGTs, as shown in Figure 11. These evaluations allowed the response and accuracy of each type of SPND to be compared.

**Fission Chambers**

The CEA fission chambers and SPND comparisons were completed by positioning the detectors in the N-16 positions shown in Figure 9. In these evaluations, tests were conducted by ascending to powers of 600 watts with at least four intermediate power levels beginning at approximately 1 mW, as shown in Figure 10. At the maximum power of 600 W, the axial flux profile shown in Figure 11 was measured by moving the detectors using the EGTs.

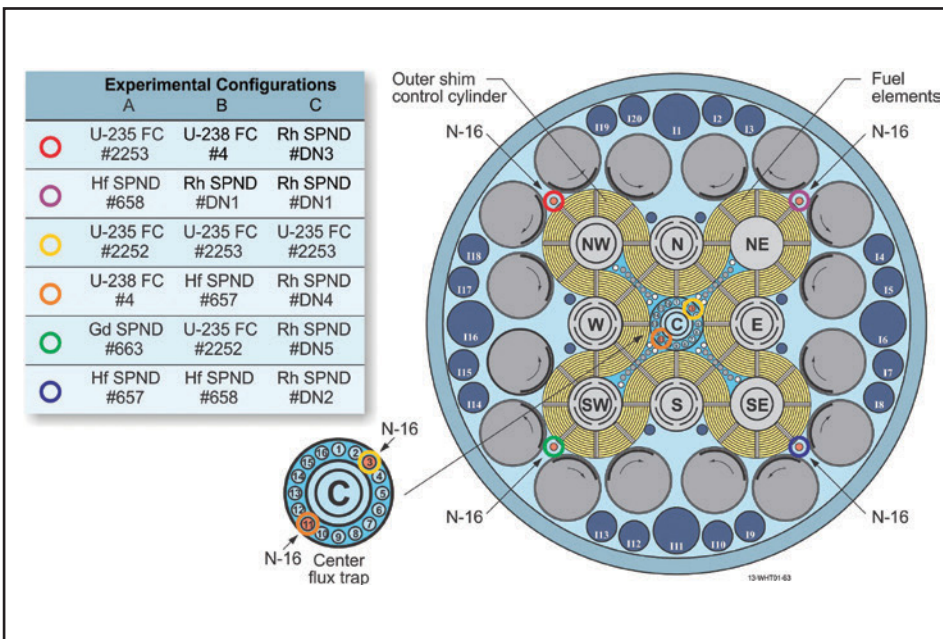


**Figure 9.** Positioning of SPNDs and fission chambers for initial evaluations.

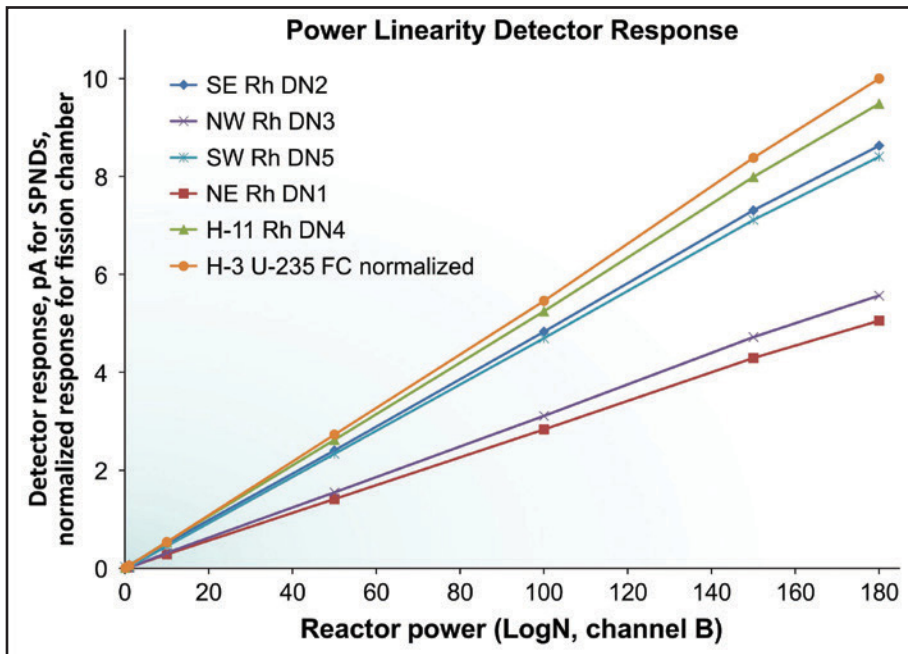


**Figure 10.** Comparison of power linearity measurements from rhodium SPNDs and a miniature fission chamber from experimental Configuration C.

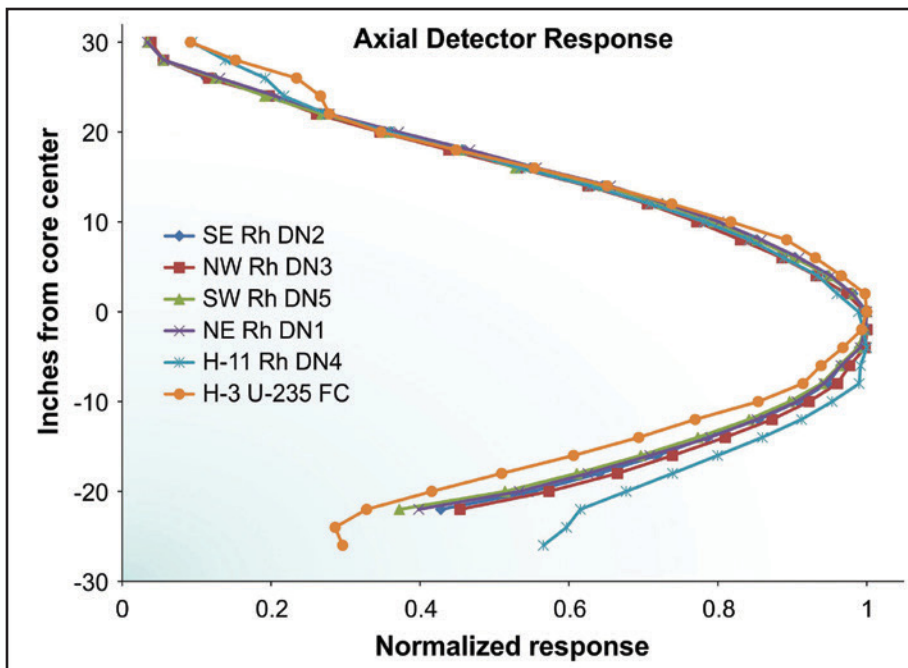


**Figure 11.** Axial flux profile from rhodium SPNDs and a miniature fission chamber from experimental Configuration C.

The CEA fission chambers and SPND comparisons were initiated in October 2010. Two CEA researchers traveled to ATRC to assist with these initial evaluations. However, the 2013 evaluations were independently completed by INL and ISU researchers. These evaluations demonstrated that several sensors could be used to determine lobe power. Results from the evaluations are being assessed to determine the optimum sensor to measure regional core power in ATRC and provide insights into a suitable system for ATR (see Figure 12).

### Summary

A joint ISU/INL/CEA project, funded through the ATR NSUF, has been completed to evaluate real-time, state-of-the-art, in-pile flux detection. A new capability for evaluating flux detectors, which includes specialized instrument positioning hardware and associated software, was developed to facilitate these evaluations at INL's ATRC. The effort evaluated several types of in-core flux sensors, and the data and fixturing developed in support of this effort have been and will, in the future, be used to support various programs. Axial flux profile measurements and power linearity measurements have provided new data for use in understanding ATRC power monitoring and flux profiles.

This effort complements current activities to improve ATR software tools, computational protocols, and in-core instrumentation under the ATR Modeling, Simulation, and Verification and Validation Upgrade Initiative. In addition, this research supplements work to replace nuclear instrumentation under the ATR Life-Extension Program and on going efforts to provide enhanced instrumentation for users of ATR NSUF.

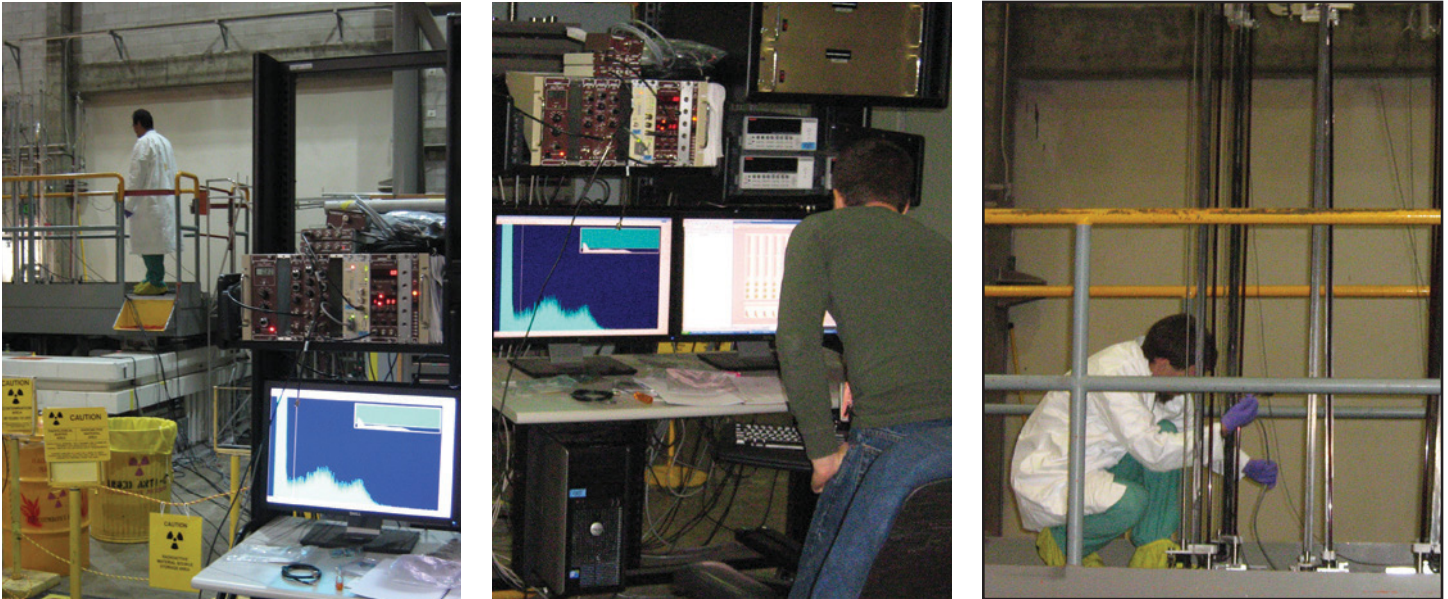


**Figure 12.** INL and ISU researchers completing in-core sensor evaluations.

## Acknowledgements

Work supported by the U.S. Department of Energy, Office of Nuclear Energy, Science, and Technology, under the U.S. Department of Energy Office of Nuclear Energy's Idaho Operations Office Contract DE-AC07-05ID14517.

## References

1. INL/EXT-08-14709, *FY2009 Advanced Test Reactor National Scientific User Facility User's Guide*, Idaho National Laboratory (2009).
2. J. Rempe, D. Knudson, J. Daw, T. Unruh, B. Chase, and K. Davis, "Enhanced In-pile Instrumentation at the Advanced Test Reactor," *invited paper for ANIMMA 2011 Special Edition, IEEE Transactions on Nuclear Science*, 59 (4), Part 2, 1214 -1223 (August 2012).
3. J.L. Rempe and D.W. Nigg, *FY-10 Irradiation Experiment Plan for the ATR National Scientific User Facility – Idaho State University Project Evaluating Flux*, Internal INL report, PLN-3351, May 2010.
4. D.W. Nigg, J.L. Rempe, T. Unruh, and J. Neilson, *Qualification of Devices for Neutron Flux Measurements in the Advanced Test Reactor Critical Facility*, Internal INL report, TEV-885, May 2010.
5. INL/EXT-10-19940, *Advanced Test Reactor Core Modeling Update Project Annual Report for Fiscal Year 2010*, Idaho National Laboratory (2010).
6. INL/EXT-11-23348, *Advanced Test Reactor Core Modeling Update Project Annual Report for Fiscal Year 2011*, Idaho National Laboratory (2011).
7. W. P. Poenitz, D.W. Maddison, J.M. Gasiello, S. G. Carpenter, and R. J. Armani, " $^{235}\text{U}(n,f)$ ,  $^{238}\text{U}(n,\gamma)$ ,  $^{238}\text{U}(n,f)$ , and  $^{239}\text{Pu}(n,f)$  Reaction Rate Measurement Calibrations at ZPPR," ANL Internal Document, ANL-87-5.
8. D.W. Nigg, C.A. Wemple, R. Risler, J.K. Hartwell, Y.D. Harker, and G.E. Laramore, "Modification of the University of Washington Radiotherapy Facility for Optimization of Neutron Capture Enhanced Fast Neutron Therapy," *Medical Physics*, 27, 359-367, (2000).
9. G.R. Imel and P.R. Hart, "The Performance of Hafnium and Gadolinium Self Powered Neutron Detectors in the TREAT Reactor," *Nuclear Instruments and Methods in Physics Research B*, 111, 325-336 (1996).
10. M.E. Miller, L.E. Mariani, M.L. Szejnberg Goncalves-Carralves, M. Skumanic, and S.I. Thorp, "Implantable self-powered detector for on-line determination of neutron flux in patients during NCT treatment," *Applied Radiation and Isotopes*, 61, 1033-1037 (2004).



**Troy Unruh** (B.S., 2004, and M.S., 2010, Nuclear Engineering, Kansas State University) has over 10 years of experience with reactor operations and experiments. His research team received an R&D 100 award for the high-efficiency semiconductor neutron detector developed as part of his Kansas State University graduate research. He is an early-career R&D engineer at the High-Temperature Test Laboratory and is currently pursuing a doctorate in nuclear engineering from ISU. During his tenure at INL he completed a 6-month assignment at CEA studying fission chambers. Mr. Unruh currently leads research efforts to develop micro-pocket fission detectors and perform flux detector evaluations at ATRC. He has authored and co-authored over 20 archival peer-reviewed journal publications and peer-reviewed conference papers.



**Benjamin Chase** (B.S., 2004, Interdisciplinary Engineering, ISU) is a Nuclear Engineer in the Irradiation Testing Department at INL. He works at the High-Temperature Test Laboratory developing, testing, and deploying detectors for use in high-temperature, high-flux conditions. He also performs reactor physics analysis as part of the ATR Low-Enriched Uranium Conversion Project. He is involved in experiments at ATRC to perform validation measurements for the new ATR reactor physics methods upgrade and to evaluate advanced detectors. Prior to working on these projects, he was a reactor engineer at ATR. Prior to working at INL he was a Nuclear Power School instructor at the Naval Nuclear Power Training Command. Mr. Chase is currently working to finish his Master's Degree in Nuclear Engineering at ISU.



**Joy Rempe** (B.S., 1981, Nuclear Engineering, University of Missouri-Rolla; M.S., 1983 and Ph.D., 1986; Massachusetts Institute of Technology) is a Laboratory Fellow and Group Leader at INL where she leads in-pile instrumentation development efforts for INL's ATR NSUF. She also provides consulting assistance to vendors, utilities, and regulators on severe accident issues. With over 28 years of research experience, Dr. Rempe has authored or co-authored over 50 archival peer-reviewed journal publications and over 90 peer-reviewed conference papers on reactor safety, severe accident phenomena, high-temperature testing, and in-pile instrumentation. She is an inventor/co-inventor on five patents (pending). In 2005, Dr. Rempe was elected a Fellow in the American Nuclear Society; between 2009 and 2012, she served on the American Nuclear Society Board of Directors; in 2010, she was appointed to the U.S. Nuclear Regularly Commission's Advisory Committee on Reactor Safeguards; in 2012, she received the DOE Secretarial Honors Award; and in 2014, she was appointed by Energy Secretary Moniz to DOE's Nuclear Energy Research Advisory Committee.



**David Nigg** (Ph.D., Engineering Sciences, University of Kansas) has over 35 years of experience in computational and experimental reactor and radiation physics, research reactor applications, medical applications of nuclear and radiological sciences, radiobiology and biophysics, and technical management. He is a registered Professional Engineer by Examination in the State of Idaho. In 2006, he received the Hatanaka Memorial Award, the highest honor bestowed by the International Society for Neutron Capture Therapy, in recognition of sustained excellence and leadership in NCT research and development. He currently leads the INL ATR Modeling, Simulation, and Verification and Validation Upgrade initiative.



**George R. Imel** (Ph.D. from Pennsylvania State University) served as Dean of the College of Science and Engineering at ISU until July 2013, when he returned to full-time faculty as Professor in the Nuclear Engineering and Physics Departments. He also consults for the European Union's Euratom and the International Atomic Energy Agency. Prior to coming to Idaho State in 2007, Dr. Imel worked in applied physics at Argonne National Laboratory for 24 years. His most recent assignment was a 10-year attachment to CEA/Cadarache in France, where he was involved with developing new forms of data acquisition and analysis for fast critical and subcritical systems. At CEA/Cadarache, Dr. Imel also served as a mentor for Ph.D. candidates in experimental reactor physics and was involved with five juries (three in France, one in Spain, and one in Switzerland). Dr. Imel was an original member of the working group for the TRIGA Accelerator Driven Experiment of the Italian National Agency for New Technologies, Energy and Sustainable Economic Development in Italy and was the leader of the experimental program for this multinational project. At Argonne National Laboratory West, he was section head of the Experimental Breeder Reactor-II Reactor Physics and Experiments.



**Jason Harris** (Ph.D., Health Physics, Purdue University) is an Associate Professor of Health Physics and Nuclear Engineering at ISU where he conducts research in nuclear power occupational, public dose and environmental studies, accelerator applications for homeland security, radiation detection and measurement, nuclear education, and nuclear security. He is the Director of the ISU Environmental Monitoring Laboratory and the Associate Director, Analytical Instrumentation Laboratory Lead, and Nuclear Science and Engineering Core Capability Coordinator for the Center for Advanced Energy Studies. In addition, he holds a joint appointment with INL and serves as a senior consultant for the North American Technical Center (in nuclear power plant radiation protection and environmental studies). He currently serves as the Chair for the International Atomic Energy Agency International Nuclear Security Education Network and acts as a lecturer and implementor for the U.S. Department of State Partnership for Nuclear Security. For the Health Physics Society (HPS), he has served as an International Radiation Protection Association delegate since 2004 and has also served executive roles on the HPS Academic Education Committee, the HPS Health Physics Student DVD Ad Hoc Committee; the HPS Power Reactor Section, the HPS Accelerator Section, the American Nuclear Society Board of Directors, the RETS-REMP Workshop Steering Committee, the North American Technical Center Public

Radiation Safety Research Program Effluent Expert Committee, and the International ALARA Symposium Organizing Committee. In 2012, he was awarded both the HPS Elda E. Anderson and the Purdue University HSCI Outstanding Young Alumni awards.



**Todd Sherman** has been a nuclear engineering Ph.D. student at ISU since August 2013. His thesis research consists of studying the effects of irradiation and aging on nuclear power plant concrete. Todd is a native of Idaho and graduated from Teton High School in Driggs. He received a B.S. degree in Civil and Environmental Engineering and an M.S. degree in Nuclear Engineering from the University of Utah. During his time in Salt Lake City, Todd worked in a radiochemistry laboratory for EnergySolutions and was a Senior Reactor Operator for the University of Utah TRIGA Reactor.



**Jean-François Villard** has 15 years of experience and expertise in measurement systems and nuclear instrumentation. He is head of the project that coordinates French research and development programs related to in-pile instrumentation for research reactors, including the future Jules Horowitz Reactor. He also heads the Instrumentation Sensors and Dosimetry Laboratory, which is in charge of development of measurement systems for research reactors, sensor manufacturing, measurements and analysis of reactor dosimetry for research reactor experiments, and French nuclear power plants. He assists this effort by providing insights related to in-pile testing and the associated neutron flux measurements. Mr. Villard is a World Nuclear University Fellow and has authored or co-authored over 35 archival peer-reviewed journal publications. He is an inventor/co-inventor on five patents (pending).



# Luna Innovations Irradiation Experiment

# Luna Innovations Irradiation Experiment

*J. Palmer, P.E. Murray (INL), S.B. Grover (INL-Retired)*

The reactor experiment design and fabrication groups at Idaho National Laboratory (INL) implement customer requirements into safe, robust experiment assemblies and complete challenging irradiation experiments. The simplest type of irradiation experiment is termed a static capsule, which is simply a sealed capsule placed in one of the Advanced Test Reactor's (ATR) experiment positions without instrument connections. This article describes the processes used to design, fabricate, assemble, and irradiate a unique static capsule experiment that met challenging requirements from the customer Luna Innovations, Incorporated (Luna) for irradiating a fiber optic-based thermal sensor in ATR. As discussed within this paper, irradiation that met customer temperature and fluence requirements was completed in a capsule that was designed to facilitate low-cost shipping and lower-cost post-irradiation examination (PIE) activities. INL expertise allowed this challenging irradiation to be successfully completed at a cost that was 20% lower than the estimated budget.

## Introduction

The experiment design group supporting ATR provides engineering services for a variety of U.S. Department of Energy (DOE) programs, as well as non-DOE programs. Small Business Innovation Research grants from DOE have supported Luna's work in developing thermal sensors based on fiber optic technologies for use in high-temperature reactor environments. The purpose of these single-point sensors is to make low-drift measurements of temperature and to provide both an alternative and a complement to thermocouples and resistance

temperature detectors. Accuracy concerns often restrict the use of resistance temperature detectors to monitoring temperatures below 400°C, and commercial thermocouples have been observed to suffer both drift and insulation shunting errors when operated at elevated temperatures [1, 2].

Luna's thermal sensor design uses an optical fiber to optically couple to the sensing element, which incorporates a radiation-hardened, metal-oxide transducer. The radiation-tolerant optical fiber employed in this sensor does experience radiation darkening due to atomic displacement and ionization from fast neutrons and high-energy gamma rays, as do all silica-based optical fibers. However, the darkening of the optical fiber does not result in sensor drift, because the fiber is not the sensor material; the measurement of temperature is independent of attenuation in the fiber, short of fiber failure or complete loss of optical transmission.

Luna has conducted multiple tests of this type of thermal sensor in the Ohio State University (OSU) research reactor. Sensors based on this technology have been shown to have good survivability up to a fast neutron ( $E > 1$  MeV) fluence of  $2 \times 10^{19}$  n/cm<sup>2</sup> and 87 GRad gamma radiation [3]. The tests in ATR will allow Luna to evaluate the performance of their sensors at high temperatures (up to 1000 °C) and fast fluences ( $E > 0.1$  MeV) up to  $8 \times 10^{20}$  n/cm<sup>2</sup>.

As part of this Luna Small Business Innovation Research Phase III Project, INL developed and fabricated a unique capsule design, assembled the capsules containing the Luna fiber optic sensors, and completed

the required irradiation. This paper describes processes used by INL's reactor experiment designers to meet Luna test objectives. Processes and analyses described in this paper illustrate INL capabilities for completing such challenging static capsule experiments.

## Capsule Design

Luna test specifications required that one or more sensors be irradiated to fast neutron fluences ( $E > 0.1$  MeV) of at least  $6.8 \times 10^{20}$  n/cm<sup>2</sup>, and at temperatures ranging from 800 °C to 1000 °C. In addition, Luna requirements necessitated that the test capsule incorporate materials with low neutron activation characteristics, such that after irradiation, the capsule could be shipped in a lightweight carrier and be disassembled in a shielded glove box. The INL design team evaluated available reactor positions and determined that a small B position, specifically B8, would provide the best combination of cost, neutron flux, and test volume to meet Luna's experiment objectives (see Figure 1). Using this position, Luna's neutron fluence objectives could be met in one 50-day cycle and nine sensors could be irradiated, with five of them meeting the target fluence. The test matrix agreed upon by INL and Luna is shown in Table 1.

Table 1. Luna Experiment Test Matrix		
Luna Experiment. Designation: Capsule ID	Fluence Level* (low, medium, high)	Target Temperature** for Sensor (capsule centerline - °C)
Luna-9	Low	800
Luna-8	Medium	1000
Luna-7	High	800
Luna-6	High	1000
Luna-5	High	1000
Luna-4	High	800
Luna-3	High	1000
Luna-2	Medium	800
Luna-1	Low	1000

\*Low  $\approx 3 \times 10^{20}$  n/cm<sup>2</sup> (E > 0.1 MeV), Med  $\approx 6 \times 10^{20}$  n/cm<sup>2</sup>, High  $\approx 8 \times 10^{20}$  n/cm<sup>2</sup>.  
 \*\*Calculated temperatures are to be within  $\pm 50^\circ\text{C}$  of target temperatures shown.

The capsule design for the Luna experiment is shown in Figure 2. Primary capsule design objectives included: 1) protective structures to prevent the fiber optic sensors from damage during handling and transport, 2) material thermal properties and fill gas mixtures that would yield the high irradiation temperatures desired by Luna, and 3) to keep shipping and PIE costs low, the irradiated capsules must meet Department of Transportation (DOT) Type A source term limits (thus, reducing capsule shipping costs and allow PIE activities to be completed in existing OSU facilities).

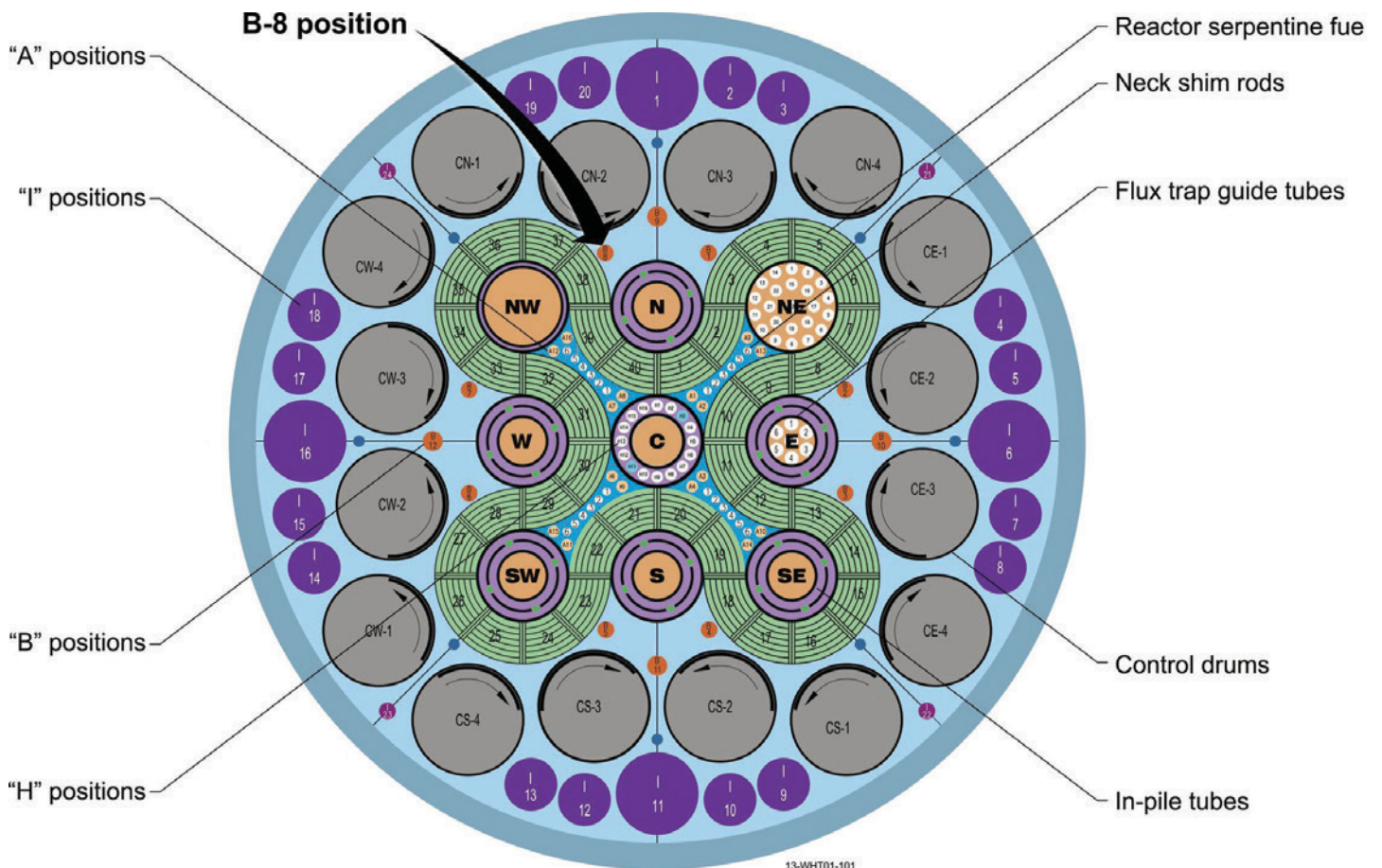
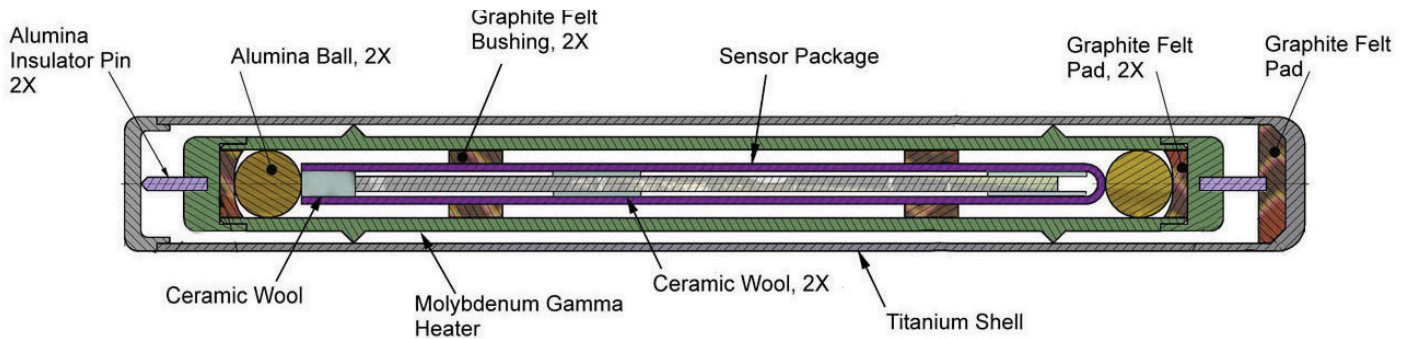


Figure 1. ATR core cross section showing B-8 position.



**Figure 2.** Luna capsule cross section.

Luna provided the primary protection for their fiber optic sensors. Sensors were housed inside a vanadium sleeve (shown as “Sensor Package” in Figure 2). Then the INL design team added graphite felt pads to cushion the sleeve axially and radially and added alumina balls and pins to thermally insulate the sensor package from the water-cooled titanium capsule, as shown in Figures 2 and 4.

The high irradiation temperatures were achieved by surrounding the sensor packages with a “gamma heater” made of high-density molybdenum (see Figure 4). Molybdenum was selected because it is essentially the only high-density, high-temperature material that does not significantly activate under neutron irradiation. As noted above, the use of molybdenum allowed the INL design team to meet shipping requirements in a relatively lightweight shipping package and also lowered the dose rates during handling and disassembly. Thermal analyses also allowed INL researchers to select an appropriate gas composition (a helium/argon mixture) that ensured the test was maintained at the values specified by Luna.

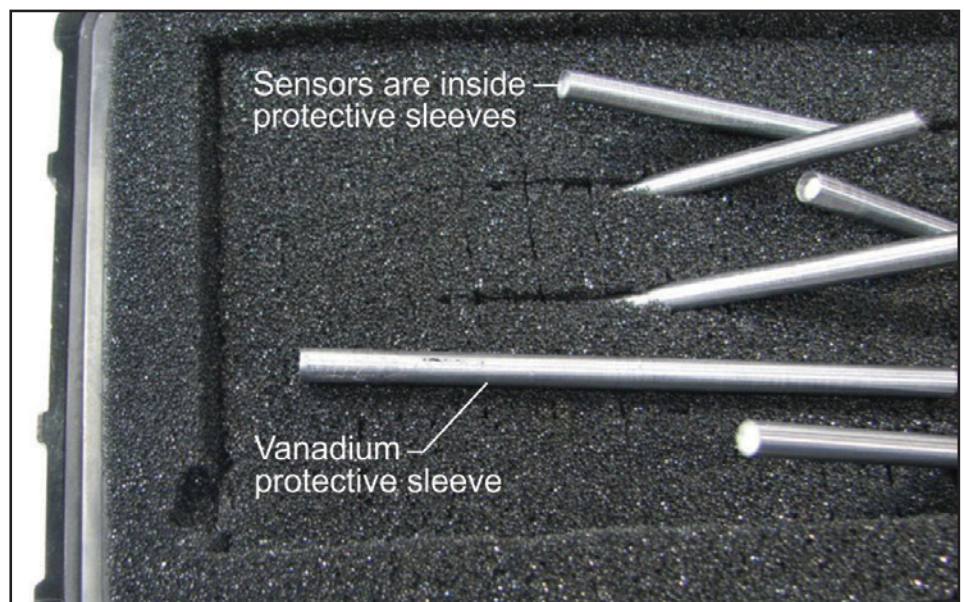


**Figure 3.** Luna sensor packages.



**Figure 4.** Molybdenum heaters with sensors inside – ready to be installed in capsule bodies.

Titanium was selected as the capsule shell material because it is easy to weld and activates less than many other common capsule materials, thus facilitating the requirement to meet Department of Transportation (DOT) Type A shipping requirements. In addition, titanium is a material that is approved by the American Society of Mechanical Engineers Code for Class 3 nuclear vessels, which simplified the ATR safety evaluation. Finally, titanium was selected because the weld procedures that were needed to fill the capsules with different blends of inert gases had previously been qualified by INL weld engineers for ATR use.

### Physics and Shielding Analyses

For irradiation experiments in ATR, physics analyses are required to determine the heat rates of the materials being irradiated and to calculate radioisotopic source terms for the capsules and contents after they have been irradiated. The quantities of radioisotopes produced were compared against the allowable quantities for DOT Type A shipments, and it was determined that after 2 months decay time, all nine capsules could be shipped together in a single package and still meet Type A limits.

To qualify as a Type A shipment, dose rates outside of the shipping package must also fall below certain limits. Luna provided a shielding container that incorporated 10 cm of lead shielding and weighed about 300 Kg. A shielding analysis was performed that showed this shielding was sufficient to meet the DOT dose-rate limits with a factor

of two margin. Hence, these results allowed Luna to use this relatively lightweight shipping container that could be accommodated in existing OSU PIE facilities (if a large cask had been required, it would have required a more extensive PIE facility with a heavy lift capability and a full hot cell).

Additionally, dose rates were calculated for individual capsules and the various capsule components to determine if the capsules could be disassembled in a shielded glove box instead of a full hot cell. Results demonstrated that the OSU shielded glove box could be used if the capsules were allowed to decay for about 7 months.

### Thermal Analysis

Thermal analyses were performed for each of the nine Luna capsules to determine the temperature of the fiber optic sensors (and other capsule components) during normal reactor operation. Results from these analyses were used to determine the temperature-control-gas mixtures needed to attain the desired irradiation temperatures for the sensors. Various mixtures of helium and argon in 10% increments were evaluated to determine the best gas mixture for each capsule. A temperature contour plot of Capsule 5 (at core mid-plane) is shown in Figure 5. Note that the largest temperature changes were in the gas gaps between the titanium capsule and molybdenum sleeve and between the molybdenum sleeve and vanadium sheath. Also, analyses indicated that the alumina pins (see Figures 2 and 4) were effective thermal insulators between the capsule and its contents.

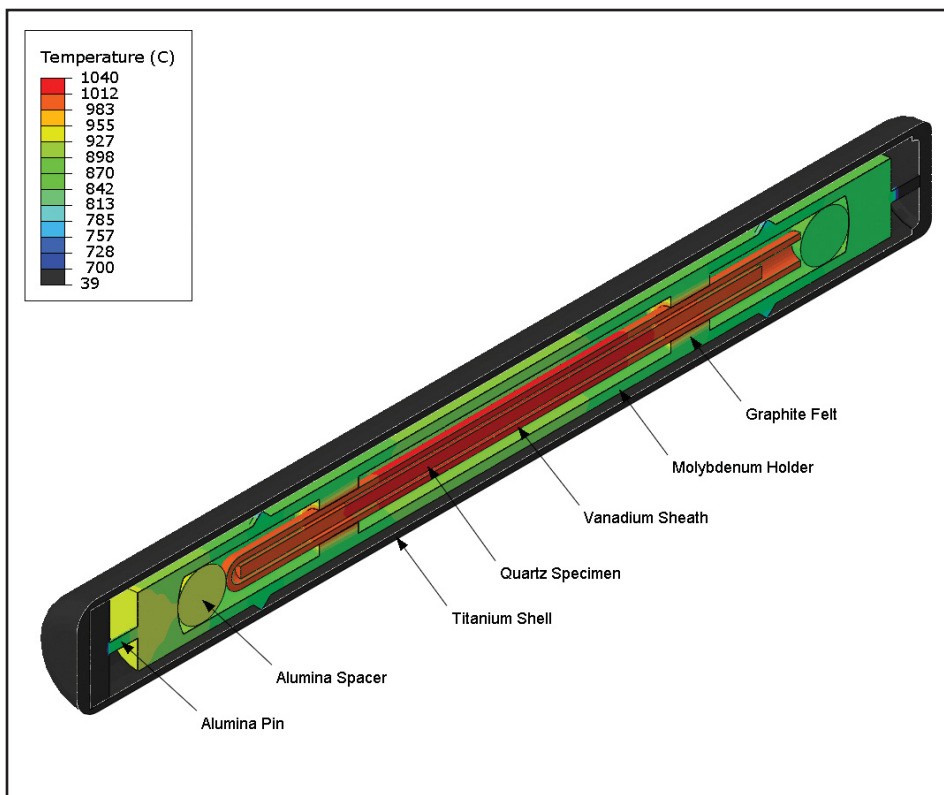
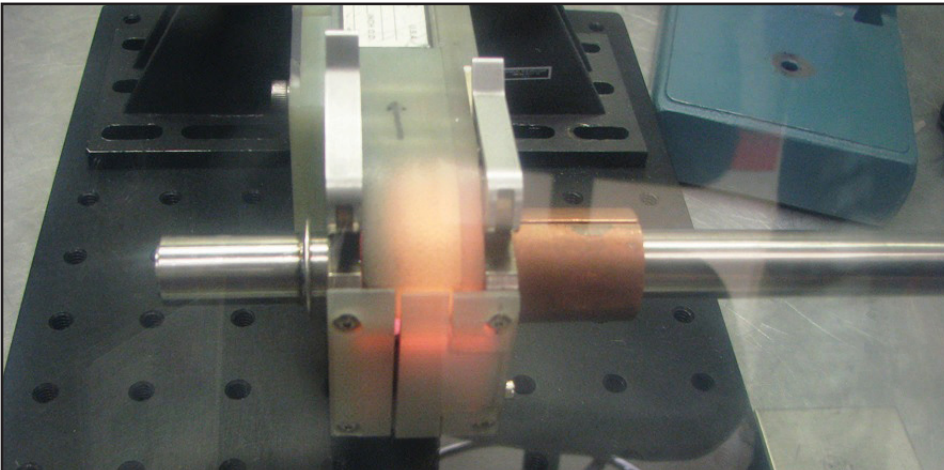


Figure 5. Temperature contour plot of Luna Capsule 5.

## Fabrication and Assembly

To overcome difficulties associated with machining titanium and molybdenum, INL completed developmental machining work to ensure all components could be fabricated to the required tolerances. Results from this developmental work further enhances the ability of INL's experimental design and fabrication group to produce irradiation experiments using these relatively low activation materials.

Assembly was straightforward and took less than an hour per capsule. Each capsule was then placed in a glove box (see Figure 6) and filled with the precise mixture of helium and argon specified by the thermal analyses. Welding took place inside this glove box. These welds were made using a standard tubing welder placed in the glove box. The welds were autogenous (i.e., no filler metal was used). As shown in Figure 7, in the as-welded condition, these titanium welds are flush to the surface of the shell and have a smooth polished appearance. These welds successfully passed the liquid penetrant



**Figure 6.** Luna capsule being welded inside the glove box.



**Figure 7.** Nine Luna capsules—complete and ready for irradiation.

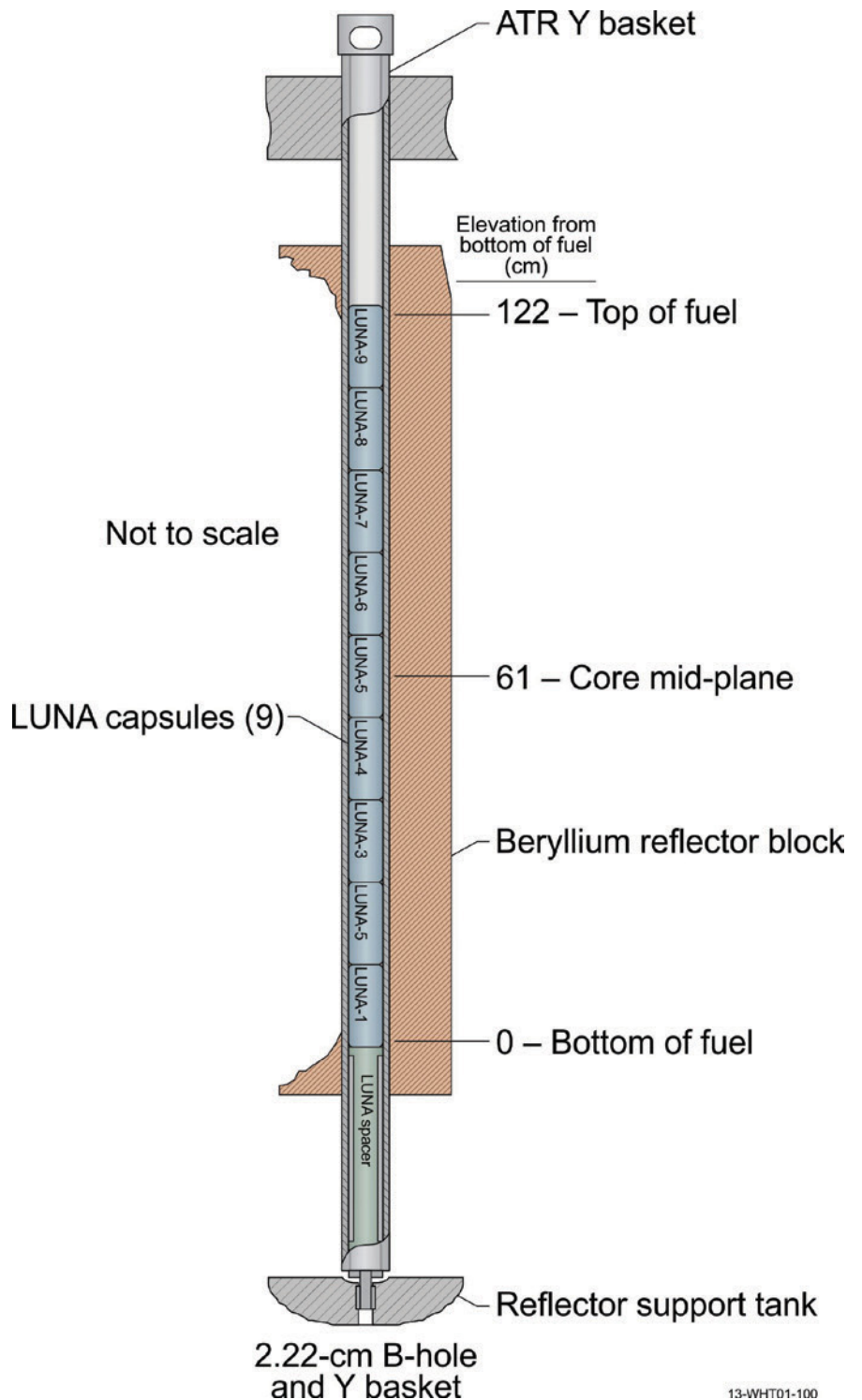
and helium leak check ( $<1.0 \text{ E-}07 \text{ cm}^3/\text{sec}$ ) examinations with no rejects.

### Irradiation and Future Activities

The Luna capsules were irradiated for 52 days in ATR Cycle 154A and completed irradiation on July 13, 2013. The capsules were irradiated in a standard ATR Y basket (see Figure 8). Following the irradiation, the capsules were placed in the ATR canal and allowed to decay for 2 months.

After this cooling period was completed, the capsules were placed in the shielded container provided by Luna. Figure 9 shows placement of the capsules in the shielded container during mock-up testing completed by INL; mock-ups are typical quality assurance processes performed by INL to ensure irradiation activities can be successfully completed. The shielded container was then placed in a DOT Type 7A drum. Using this arrangement, shipping can be completed by a commercial transport company, which is a considerably less expensive option than required for higher-consequence radioactive shipments that require a dedicated truck and driver.

These various cost saving efforts, added together, allowed the INL project team to complete their scope at a cost 20% less than the originally agreed upon ceiling for the project.



13-WHT01-100

**Figure 8.** Luna experiment installed in the B-8 position of ATR.

PIE for this experiment will be completed by OSU in a shielded glove box. Luna has performed time-motion studies to show that the capsule shells can be cut and the vanadium sheathed sensor packages extracted within minutes. As stated earlier, vanadium was selected as the sensor sleeve because of its extremely low activation under neutron irradiation. Once the sleeves have been separated from the capsules, they can be handled with gloved hands, allowing optical connections to be made to the sensors inside the sleeves. PIE activities will evaluate whether sufficient transparency remains to transmit a signal and assess the accuracy of the irradiated sensor signal.

## Conclusion

INL reactor experiment design and fabrication expertise are capable of implementing customer requirements into safe, robust experiment assemblies and completing challenging irradiation experiments. As discussed within this paper, an irradiation was completed that met customer high-temperature and fluence requirements in a static capsule that was designed to facilitate low-cost shipping and lower-cost PIE activities. INL expertise allowed this challenging irradiation to be successfully completed at a cost that was 20% lower than the estimated budget.

## References

1. H.M. Hashemian, "RTDs vs. thermocouples: Measuring industrial temperatures," *InTech*, September 1, 2003, <http://www.isa.org/>.
2. Bechtel Bettis, Inc., "NRPCT Closeout of Prometheus Sensor Development Work for NR Information," Bettis Atomic Power Laboratory, December 21, 2005.
3. R.S. Fielder, D. Klemer, and K.L. Stinson-Bagby, "High-Temperature Fiber Optic Sensors, an Enabling Technology for Nuclear Reactor Applications," *ICAPP*, 2338 (2004).

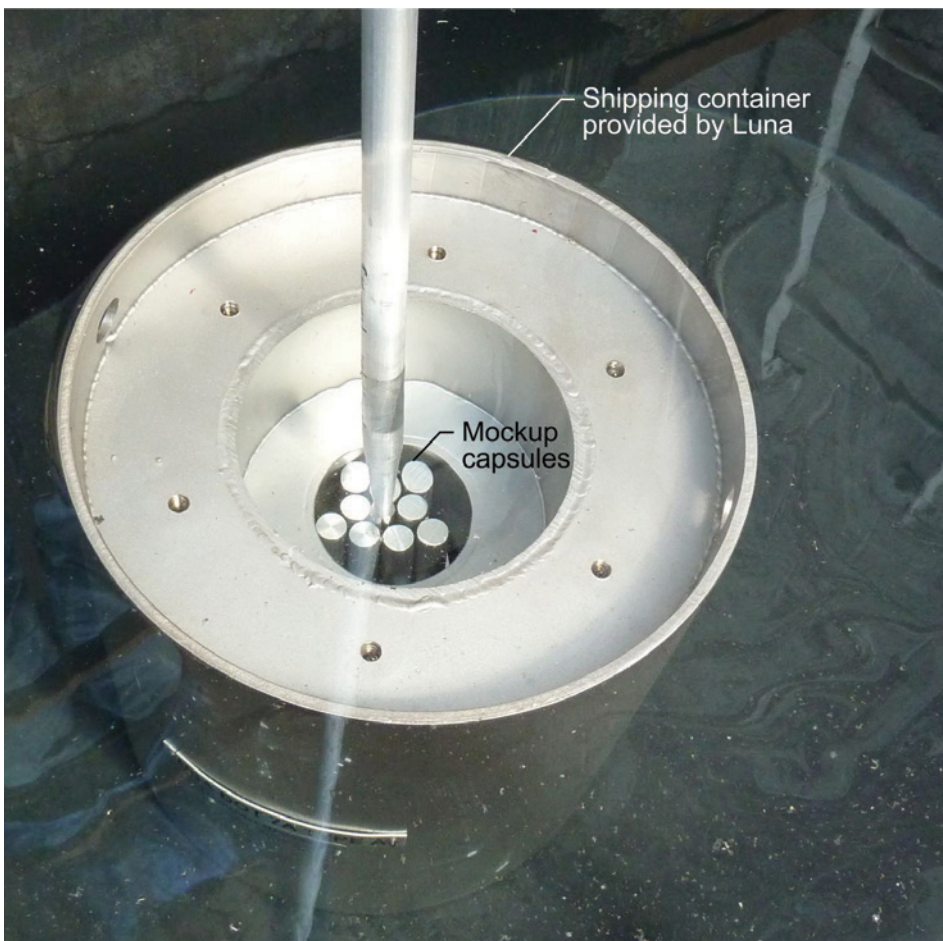


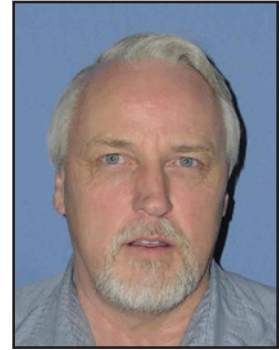
**Figure 9.** Shielding container provided by Luna (photo taken during INL mock-up testing).



**Joe Palmer** (B.S., 1987, Mechanical Engineering, Brigham Young University; M.S., 1988, Mechanical Engineering, Brigham Young University) is a mechanical design engineer at INL. He designs temperature-controlled experiments and experiments for the Hydraulic Shuttle Irradiation System. Mr. Palmer has 25 years of extensive experience in reactor experiment design, chemical process equipment design, dynamic systems modeling, piping systems, finite element stress, and thermal analysis. He also holds a Professional Engineering license in Idaho.



**Paul Murray** (Ph.D., Engineering Mechanics, University of Texas at Austin) studied finite element methods for flow and transport processes. His research includes computational mechanics and heat transfer, finite element analysis, nuclear reactor hydrodynamics, welding process modeling, and thermal analysis of irradiation experiments. He has been employed at INL since 1989 and is currently with the ATR Experiment Design and Analysis Department.



**S. Blaine Grover** (B.S., 1978, Nuclear Engineering, Idaho State University; Registered PE) has been involved in designing irradiation experiments and associated support systems for ATR during almost all of his 30-year tenure at INL. Mr. Grover retired from INL in 2013. Before leaving he served as the technical lead for the ATR irradiation experiments in support of the U.S. DOE Next Generation Nuclear Plant Program, which included both fuel and material irradiation testing. Mr. Grover also supported developing new irradiation experiment programs and external customers for ATR, as well as assisting ATR NSUF.



